Alma Mater Studiorum · Università di Bologna

Scuola di Scienze
Dottorato di ricerca in Fisica
Ciclo XXXII

Settore concorsuale di afferenza: FIS/01 - FISICA SPERIMENTALE
Settore scientifico disciplinare: 02/A1 - FISICA SPERIMENTALE DELLE INTERAZIONI FONDAMENTALI

Plasma Production via 6 ns Pulsed Laser at 1064 and 532 nm wavelengths on Nanostructured Targets

Presentata da:

Marco Frassetto

Coordinatrice del dottorato:

Prof.ssa Silvia Arcelli

Supervisore:

Dott. Fabrizio Odorici

Co-supervisore:
Prof. Marco Cuffiani

Anno Accademico 2019/2020

Abstract

This thesis presents the result of a study, within the scope of the PLANETA experiment (an INFN research program), on the effect of nanostructures on laser-matter interaction. Specifically, the plasma created on targets containing metal nanowires when irradiated with a laser pulse 6 ns long, at 1064 and 532 nm wavelength, with a power density of about $1 \cdot 10^{12}\, W/cm^2$.

Laser-produced plasma is of interest for a wide range of scientific and technological application, from using them as a source of X-rays to the possibility of nuclear fusion thanks to the high densities and temperatures which can be reached inside the plasma.

However, most applications are constrained by the very limited penetration of laser energy into matter, due to the rapid formation of a reflective critical surface of dense plasma.

PLANETA experiment was meant to investigate if targets with metal nanowires (thin cylinders with diameter < 100 nm, smaller than the laser's wavelength, and a few micrometers long) could lead to production of a hotter and/or longer lived plasma compared to bulk metal. The proposed mechanism would be a deeper penetration of laser light into the targets, because nanowires are highly absorbing in the range of visible light. This could lead to volumetric, instead of superficial heating, and thus to the production of a hotter and denser plasma compared to a bulk metal target.

Targets were produced at the electron microscopy lab of INFN Bologna, with nanowires of different geometrical parameters and different metals (Ni, Fe, Co and Ag). They were irradiated with a Nd-Yag laser at the INFN Laboratori Nazionali del Sud in Catania, and the resulting plasmas were observed with detectors of several kinds to compare them with plasmas from bulk metals. A different INFN facility at the Department of Physics, University of L'Aquila, equipped with a 532 nm wavelength laser was available to the PLANETA experiment. Although at the time of this writing, data from green laser irradiation were very limited, hey give a useful comparison and their analysis is included.

To investigate the impact of nanostructures on plasma evolution, properties of the produced plasmas were tested for different kinds of targets and for different beam conditions (polarization, energy).

Contents

Abstract **1**

Introduction **4**

1 State of art **6**
1.1 Laser produced plasma 6
1.1.1 Features and applications of laser produced plasma 6
1.1.2 Laser coupling with matter 8
1.1.3 Plasma emission 11
1.2 Light Coupling to metallic nanowires 12
1.2.1 Nanowires as waveguides 12

2 Production of nanostructured targets **18**
2.1 Nanomaterials 18
2.2 Anodized alumina templates 19
2.3 NWs electrodeposition 26

3 Experimental setup **28**
3.1 Target production 28
3.1.1 Samples characterization 29
3.2 The 1064 nm laser setup at INFN-LNS 32
3.2.1 Laser setup 32
3.2.2 Laser and optics 34
3.2.3 Interaction chamber 41
3.2.4 Detectors 43
3.3 The 532 nm laser setup at l'Aquila 49
3.3.1 Laser system 49
3.3.2 Interaction chamber 50
3.3.3 X-ray detectors 51
3.4 Craters' analysis in Bologna 53

4 Data analysis **57**
4.1 Sample types . . . 57
4.2 Morphological analysis of craters . . . 58
4.2.1 Craters shape . . . 58
4.2.2 Morphological measurements . . . 65
4.2.3 Uncertainties and statistics . . . 67
4.2.4 Morphological data . . . 69
4.3 Visible spectrum analysis . . . 71
4.3.1 Analysis software . . . 71
4.3.2 Plasma evolution . . . 75
4.3.3 Visible emission comparison . . . 78
4.4 X-ray analysis in single photon mode . . . 84
4.4.1 Calibration . . . 85
4.4.2 Filter choice . . . 88
4.4.3 Observed spectra and temperature estimation . . . 88
4.4.4 Temperature comparisons . . . 90
4.5 X-ray analysis in flux-integrated mode . . . 93
4.5.1 Analysis software . . . 93
4.5.2 Nanowires of different metals . . . 94
4.5.3 Nanowires with different geometry . . . 96
4.5.4 Polarization analysis . . . 98
4.5.5 Plasma penetration study . . . 101
4.6 Preliminary results from green laser . . . 103
4.6.1 Available samples . . . 104
4.6.2 Focalization and energy stability . . . 104
4.6.3 Metal Filters . . . 104
4.6.4 Data Analysis . . . 108
4.6.5 Discussion . . . 110

Conclusions **110**

Bibliography **113**

Introduction

This thesis will present the results of a research activity, which was part of the INFN PLANETA experiment. The PLANETA experiment was aimed at investigating the properties of nanostructured materials, specifically ordered arrays of metal nanowires, as targets for laser plasma production, on the hypothesis that this could lead to a hotter, longer lasting plasma compared to ablation of a bulk target.

This activity involved producing the targets, irradiating them with laser pulses, and analysing the resulting plasma with different detectors to study its parameters and evolution. Hardware and software technological solutions were developed during the experiment, to allow irradiation of the targets in consistent conditions and to analyse the resulting plasma. The developed techniques will be described.

In the first chapter, the theoretical background relevant to the experiment will be presented. The processes involved in plasma production via laser ablation will be discussed, and their limitations explained. Specifically, it will be shown that the weak penetration of laser light into matter is a limiting factor in heating the plasma. Hot and dense plasma is of interest for nuclear physics research and potential technological application, but the ability to produce it with laser pulses is severely limited by the lack of penetration of laser light.

In chapter 2, the nature of nanowire arrays - the nanostructures used as targets in the PLANETA experiment - will be presented, and their construction process explained. It will be shown how controlling the production process allows to control the parameters (length, diameter, regularity...) of the resulting nanowires. Finally, the interaction between nanowires and light will be presented, to explain why nanostructured targets might help to produce dense and hot plasma through the improvement of their coupling with light.

In the third chapter, the experimental setup will be described. Two different laser irradiation setups were used during the experiment, and both will be presented. One, situated at the INFN-Catania Laboratori Nazionali del Sud facility, was used for most of the data taking, and used a 1.7 J, 6 ns infrared laser (1064 nm Nd:YAG laser). The other, situated at the Physics Department of L'Aquila, used a similar laser, but with frequency doubling capability. At the cost of shooting at a lower (600 mJ) energy, it could generate a 532 nm wavelength beam (green light). Since laser-nanostructure coupling is wavelength dependent, this allows for a useful comparison.

In chapter four the collected data and analysis will be presented. The different kind of analysis performed will be explained and their results shown. Most of the data comes from X-ray analysis of the plasma. The X-ray flux was observed both integrating over the

spectrum, to measure total intensity, and in single photon mode, to study the spectral shape. This allowed to compare different kind of targets (both with nanowires and bulk) in different conditions to study how the X-ray flux from the plasma reacted to variables of interest. Another important source of data was the study of the geometrical evolution of the plasma plume through study of the visible light emission with a fast detector. The results from this analysis will be presented, too.

Finally, in the conclusions the main findings of this study will be summarised.

Chapter 1

State of art

In this chapter, the theoretical background relevant to this thesis' work will be discussed. First, in section 1.1 plasma production via laser ablation will be presented. After a brief overview of the technological and scientific applications for laser produced plasma, this thesis will describe how laser delivers energy into matter, how the process is affected by laser wavelength and pulse duration, and the limitations to such a process which make very difficult creating a hot plasma in such a way. Finally, the cooling processes which end the plasma state will be considered. In subsection 1.1.3, emissions from plasma, in particular in the X-ray range, will be discussed. They are of particular interest to this study because both experimental setup used for data taking had detector sensitive to X-rays. Therefore, the relation between plasma parameters such as temperature and its emission spectrum will be of great interest to this work. Finally, the state of art in producing hot and dense plasma will be presented, and it will be shown that nanostructured targets are a promising avenue of research to obtain this kind of plasma.

1.1 Laser produced plasma

1.1.1 Features and applications of laser produced plasma

Since laser light is an effective way to deliver energy with high power density, it can be used to heat matter to the point of ionizing the atoms, producing a plasma. Laser production of plasma is of interest for a wide array of scientific and technological applications, such as micromachining, X-rays production, nuclear physics and acceleration of charged particles [1] [2].

To understand the peculiarities of laser produced plasma, it's useful to compare it with the other main technological strategy to produce hot plasma: magnetic confinement. In magnetic confinement, a small amount of matter is gradually heated to very high

temperatures by means of electrical currents and electromagnetic waves, while strong magnetic fields are used to prevent the plasma from dispersing. This kind of plasma can be maintained as long as energy is supplied, but since containment becomes more difficult for higher temperature and density, only comparatively low densities can be reached, so that maintaining the temperatures required for nuclear fusion, in the order of tens of keV, has proved difficult.

By contrast, laser produced plasma is transient, but since it can deposit a large amount of energy in a short time and a very localized area, it can reach very high values of temperature and density at the same time. This makes it useful for different approaches to nuclear fusion, as in the nuclear confinement fusion design, and is of interest to astrophysical research, since it allows to study the behavior of plasma in conditions closer to those found in star cores. Since the cooling plasma emits a strong X-ray flux, it's also a promising source for imaging and diagnostic, more energetic and bright than X-ray tubes and much more compact compared to accelerators [3].

The main limitations of laser plasma production are its short lifetime and the low efficiency of energy delivery from the laser beam into matter. So, the possibility to obtain LPP (Laser Produced Plasma) with higher energy content and longer confinement time is of great interest for all aforementioned applications.

Unfortunately, there is a fundamental limit in the absorption of laser energy into matter: laser light penetrates very little into ordinary matter (tens of nm at most). In the following sections, the theory of laser interaction with matter will be briefly exposed, and the factors limiting its efficiency will be discussed. In this way, the reason for our interest in nanostructured materials as targets for laser beams will be explained.

Therefore, during laser irradiation of ordinary matter, only a thin skin of dense plasma is formed. This first layer of plasma prevents any further heating of the target, because dense plasma reflects very efficiently electromagnetic radiation [4]. Due to this, only a fraction of a laser pulse energy heats the target, forming a thin layer of dense plasma, which quickly cools due to expansion [5].

All mentioned application of LPP would benefit from a deeper heating of the target. With a volumetric instead of superficial heating, a longer-lived, denser and likely hotter plasma could be obtained from a laser pulse.

Thanks to its light-guide behaviour, plasmonic effect could allow a deeper penetration of light into matter. Incoming laser light, instead of heating only the first few tens of nm of the target, could convert its energy to heat within several propagation lengths (1μm). Recent literature, and this work's observations, show a greatly increased X-ray flux for nanostructured targets compared to Al-Bulk ones [6, 7].

The behaviour of a LPP, especially in a complex medium like a nanostructured target,

is very difficult to be understood in detail. Simulations are very complex even when using several approximations, and data are difficult to gather and analyse. Still, an overview of the processes involved in energy transfer to and from LPP is necessary to understand the potential advantages of nanostructured targets.

1.1.2 Laser coupling with matter

Laser interaction with matter depends on a great number of factors, the most important being laser intensity, pulse duration and wavelength. Of course, different kinds of target also behave differently. For this thesis' purpose, we'll consider bulk metal targets and semiconductors, since this experiment used as targets metal nanostructures in a semiconductor matrix. The mechanisms involved in energy transfer change over time as matter is ionized into a plasma. In particular, as will be seen, the high reflectivity of plasma drastically lowers the efficiency of heating after plasma formation.

Optical penetration

In the first moments (<1 ps) [4] of the laser pulse, energy from the beam is directly transferred to the free electrons in the material by ohmic heating. In metals, free electrons are abundant, while in semiconductors electron-hole pairs are quickly generated. The optical penetration depth is extremely limited, in the order of tens to few hundreds of nanometres into the surface, depending on wavelength and material. So, only a very thin layer of material is directly heated by laser light. In those first moments, free electrons effectively form their own plasma, then start transferring energy to the atom lattice. This energy transfer happens very quickly for metals ($\approx ps$), more slowly for semiconductors (up to $\approx$ 1 ns, depending on conditions). When energy is transferred to the atoms, the material quickly disintegrates, forming a plasma cloud between the laser beam and the remaining solid matter. The interaction is now laser-plasma and plasma-target. While the next section will be considered how the laser beam interact with plasma, it should be noted that heat conducted by the plasma will keep transferring to the target, thus ablating it much deeper than the thin layer reached by laser light.

Laser-plasma coupling and critical density

EM wave propagation: Once the laser is mostly interacting with the plasma, the absorption of light strongly depends on laser parameters such as intensity and wavelength. In general, energy can be transferred to the plasma by damping of the electromagnetic waves within the plasma. The dispersion relation of an electromagnetic wave in a plasma

is given by:

$$\omega^2 = k^2c^2 + {\omega^2}_{\mathrm{pe}} \tag{1.1}$$

where ${\omega^2}_{\mathrm{pe}}$ is the plasma frequency.

To understand how the laser beam interact with the plasma, consider that the light's electric beam will cause the free electrons to oscillate. For a strong field, oscillation velocity is:

$$v_{osc} = \frac{e \cdot E}{m_e \omega} = \sqrt{\frac{I \cdot \lambda^2}{1.39 \cdot 10^{10} W/cm^2}} \tag{1.2}$$

where I is the laser intensity and λ is the wavelength. Depending on the factor $I \cdot \lambda^2$, different heat transfer processes can be dominating $I \cdot \lambda^2$. Interactions of laser light with plasma are extremely complex, requiring detailed modelling to be understood, and exceed the scope of this work. However the main processes by which energy can be transferred from a laser beam to a plasma will be briefly described, with some of their functional dependencies, to understand which factors can influence laser-plasma coupling:

- **Inverse bremsstrahlung:** The electric field from the laser beam forces an oscillation on the plasma electrons, with a so-called quiver velocity of.

$$V_q = \frac{eE}{m_e \omega_L} \approx 25 \lambda_L(\mu m) \sqrt{I(W/cm^2)} cm/s \tag{1.3}$$

  Oscillating electrons can collide with ions, heating the plasma by inverse bremsstrahlung. This process dominates at comparative low $I \cdot \lambda^2$. Bremsstrahlung absorption coefficient is proportional to

$$K_b = \frac{Z N_e^2}{T_e^{3/2} \omega_L} \frac{1}{\sqrt{1 - \frac{\omega_{pe}}{\omega_L^2}}} \tag{1.4}$$

  Note that inverse bremsstrahlung is most effective for high Z, high density plasma. Since plasma produced by ablation of metal targets fullfill both conditions, this mechanism was likely the leading one at our experimental conditions.

- **Resonant absorption:** In this process, which becomes important over $I \cdot \lambda^2 = 10^8$ W, the electric field of the laser pulse perpendicular to the target surface creates a plasma density wave (also called *Langmuir wave*), which in turns heats the electrons within the plasma as it is dampened, both by collisional and non collisional processes.

- **Vacuum heating:** This process dominates at high intensities (over $I \cdot \lambda^2 = 10^{10}$ W). In vacuum heating, free and even bound electrons at the edge of the plasma

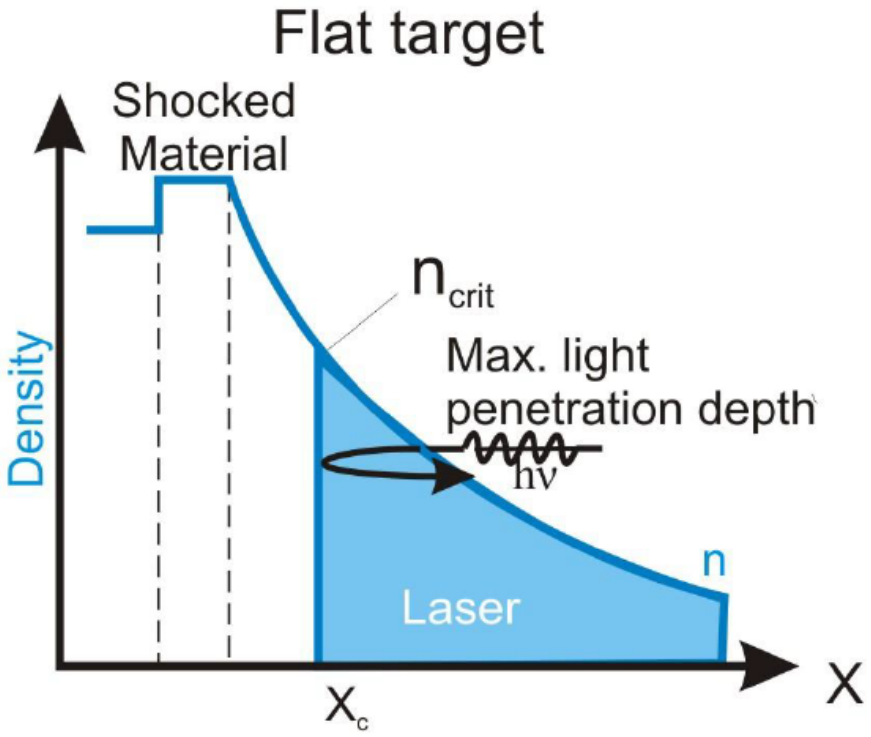

Figure 1.1: Light reflection on critical density plasma. As the incoming EM wave approaches the surface, it encounters denser and denser plasma, until critical density (which is two orders of magnitude lower than solid density) is reached and light is reflected back. Due to this effect, laser heating of a dense plasma is very inefficient [4].

are ripped away during a half-cycle of the EM wave, and then accelerated back against the plasma, transferring energy to it.

All these processes are limited by a fundamental constraint: the ability of the EM wave to penetrate plasma. When a plasma reaches sufficient electron density (about two orders of magnitude below that of a solid), it becomes almost perfectly reflective to electromagnetic radiation [5]. In Laser Produced Plasma, a steep density gradient forms near the solid surface, and when sufficient density is reached, a reflective critical surface forms.

The mirror-like behaviour of a critical surface (see figure 1.1) sharply limits the possibility to heat matter with laser light. A very fast laser - pulse length shorter than a femtosecond - can deliver most of its energy before plasma is formed, but still it can reach only the surface of the target, since the pulse duration is too short to allow for thermal conduction.

This is the limitation which nanostructured targets could overcome. As will be explained in greater detail in the next paragraph, nanowires normal to the surface absorb incoming photons and transport them deep into the material. It is hoped this will pro-

vide an efficient process to deliver energy into a thick volume instead of a thin surface layer. Plasma produced in this way would have two advantages: more energy would be delivered into the plasma before a reflective surface forms, and lower surface-to-volume ratio would make thermodynamic expansion slower.

1.1.3 Plasma emission

Emission Mechanisms

Once produced, laser-produced plasma cools down in two ways: by radiating energy and by thermodynamic cooling, since it's very hot and dissipates quickly. Plasma cooling process can thus be described in terms of its thermodynamic cooling time vs radiative cooling time. Radiative cooling becomes more important for hotter plasma, while thermodynamic cooling dominates for comparatively cold plasma. Radiative cooling is interesting to our study for different reasons. First, some application for laser produced plasma use it as an X-ray source, so studying the emission spectrum allows to assess it potential usefulness. But more importantly, plasma emission provides information about the internal parameters of the plasma. Thus, most of the data taken for this work are radiation measurements, either in the visible light or X-ray range. To interpret the data, it's necessary to consider the process by which a plasma emits radiation, and how emission is dependent on plasma parameters.

Radiative Processes: Plasma dynamics are extremely complex and sensitive to specific conditions, so emission spectra from plasma varies a lot. But The main contribution to emission spectrum come from a limited number of processes [4, 3]:

- **Line emission:** Emission due to de-excitation of residual electrons in ions. Lines are broadened by excited states lifetimes and Doppler effect. Lines due to this effect can be used to discern the atomic species in the plasma and their degree of ionization.
- **Recombination emission:** Emission due to photo-recombination of electrons and ions.
- **Bremsstrahlung:** The well-known phenomenon of emission due to electrons collisions with ions is particularly important for low Z plasma (since ions are completely stripped). It contributes with a continuous exponential term to the spectrum, which can be used to calculate the plasma temperature.

- K_α **emission:** This process can be observed if a population of highly energetic electrons (10-100 keV) is formed, for example due to resonant absorption. These fast electrons can be reflected against the cold, unionized matter and strip the core electrons, thus leaving a hole which is filled by a transition at a very specific energy. Since the resonance absorption process is more efficient for short-pulse generated plasma, K_α emission is more common in that kind of plasma.

Emission as a Function of Elemental Composition

X-ray varies substantially depending on the elemental composition of the plasma, with emissions rising periodically for increasing Z and then falling sharply near atomic shell closures. Due to the different available mechanisms for X-ray emission, the elemental composition difference is heavily dependent on laser fluence, becoming more pronounced at higher fluences, since more electronic transitions and ionization levels become available.

1.2 Light Coupling to metallic nanowires

While laser production of plasma is an established technique, with thoroughly documented studies, the innovative element introduced in our work was the use of a nanostructured target, specifically a matrix of vertically arrayed metal nanowires. To understand the potential advantages of this choice, and the practical difficulty of producing the targets, this section will discuss the properties of nanowires when interacting with light.

1.2.1 Nanowires as waveguides

Nanowires are thin metal wires with diameter smaller than visible light's wavelength, and up to tens of micrometers in length. They can be fabricated in densely packed arrays with the techniques which will be discussed in the next chapter.

The interest in nanowires as targets for laser-plasma production stems from the unusual properties of their interactions with electromagnetic radiation. The most important is their ability to act as a sub-wavelength waveguide, due to the formation of waves of collective electron excitation.

Nanowires can be fabricated with a much smaller diameter (< 100 nm) than visible light's wavelength. Sub-wavelength metallic structures interact with light in a much different way compared to macro-scale structures of the same material. This is due to a phenomenon called plasmonic effect, which has attracted great interest in recent years for its application in nanoscale manipulation of light.

Plasmons are collective electron excitations formed on the surface of metals, caused by electromagnetic radiation. Due to plasmonic excitations, a metal nanowire exposed to electromagnetic radiation acts as a waveguide, despite being much smaller than the incident wavelength: photons can be absorbed at one end of the nanowire, transported through its length as an electrical impulse, and re-emitted as photons (with some loss in intensity) at the opposite end [8, 9].

Plasmonic effect can be demonstrated observing the light-guide behavior of sub-wavelength metallic structures, but plasmons can also be directly imaged with near-field microscopy thanks to the strong electrical field they form near the metal surface, as can be seen in figure 1.2:

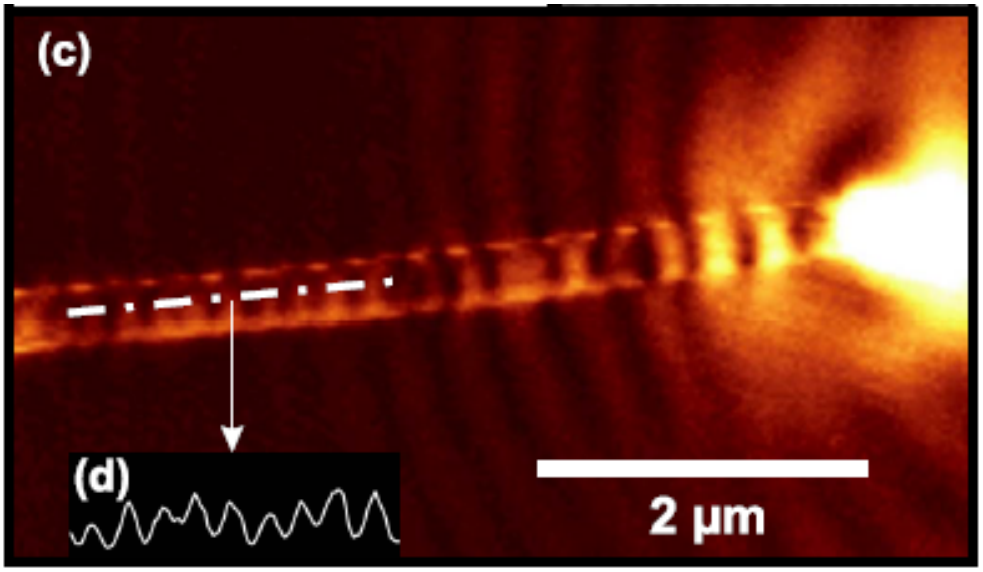

Figure 1.2: Surface plasmon oscillations imaged with Scanning Near Field Optical Microscope [27].

Plasmonic effect even works with bent nanowires and allows fan in-fan out. Thanks to these properties, metallic NWs are of great interest for many applications, from opto-electronic circuitry (as light guides with components much smaller than light wavelength) to sensors [10] and energy production [11].

Most relevant to this research is the capability of plasmonic effect to transfer energy delivered by a laser beam from the surface to the interior of a target. This allows volumetric instead of superficial heating of matter, which is of great interest for dense plasma formation. Most of this thesis' work is aimed at comparing the plasmonic effect in different nanomaterials.

Plasmonic coupling to light

Light transmission through nanowires much thinner than wavelength has been repeatedly demonstrated and studied in recent years [12]. Impressive images directly demonstrating light absorption and emissions at the ends of a nanowire have been obtained, such as in figure 1.3.

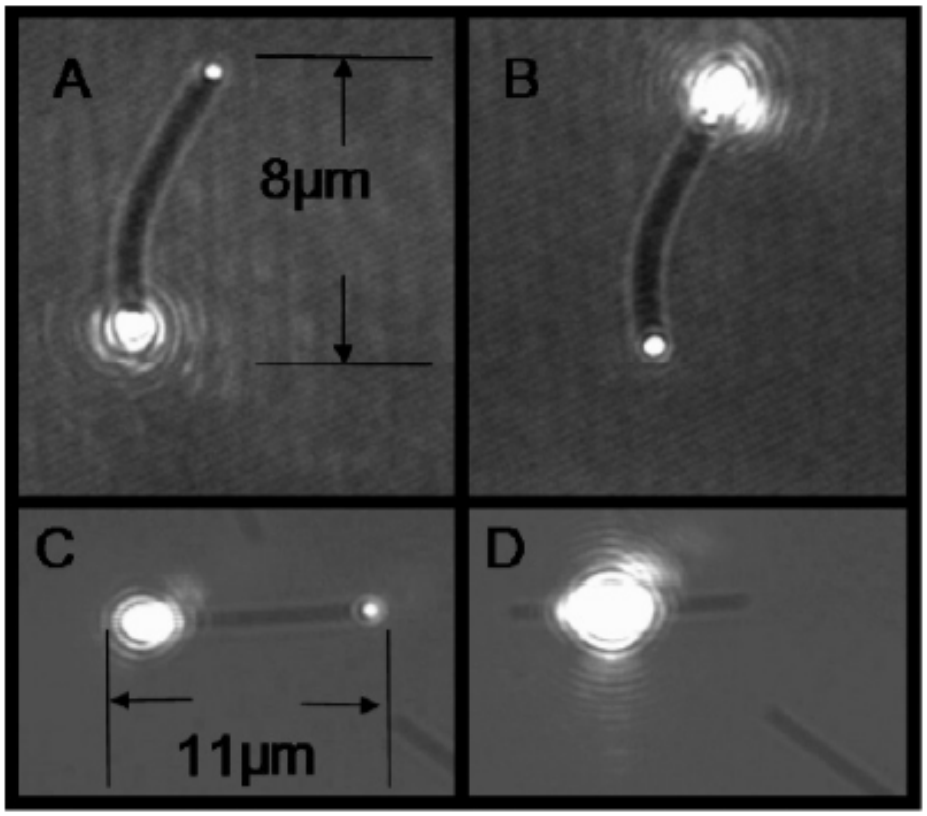

Figure 1.3: Light transmission through a metal nanowire thanks to the plasmonic effect. As can be seen, focusing light on one end of the NWs (A, B and C) causes emission at the opposite end, while focusing light on the middle of the NW (D) there is no emission, since plasmon excitations couple with photons only at discontinuities [12].

Light couples to plasmons at discontinuities. These are usually the ends of the NW, but can also be kinks or anisotropies along the wire. A gentle bend will not emit light, but will cause loss of energy, with greater loss at smaller radii [12]. This is of little concern in our experiment, since alumina-fabricated nanowires are very regular in shape and structure.

Plasmons, which can be treated as quasiparticles, propagate with specific wavelength and polarization, and nanowires have their own resonant frequency, which is strongly dependent on geometrical characteristics of the nanostructures. Therefore, photon-plasmon coupling is dependent on wavelength, and nanostructures' parameters can be tuned - at

least in principle - to absorb specific wavelengths [8].

The change in photon-plasmon coupling for different nanostructure geometry can be seen quite spectacularly observing the colour change in our samples for different heights of nanowires. As can be seen in figure 1.4, there is a specific progression:

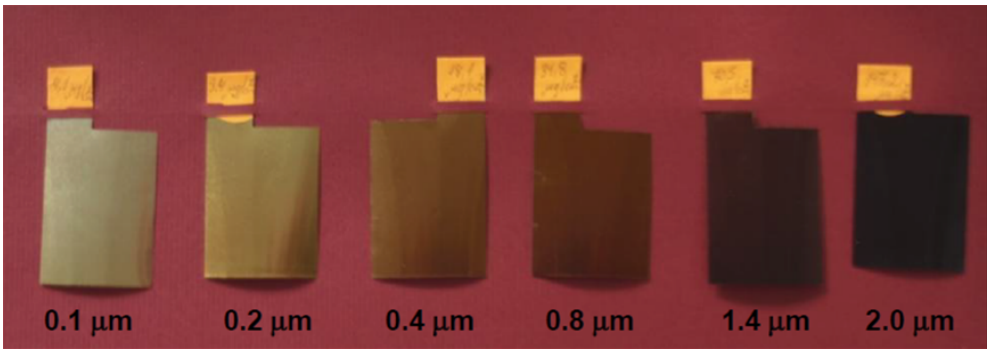

Figure 1.4: Change in light absorption for samples with NWs of different length. From left to right, the sample in this image have progressively longer NWs, from 0.1 to 2.0 μm. As can easily be seen, the longer the NWs, the darker the colour.

- Porous alumina without nanowires, or at very low NWs length, shows the colour of the aluminum substrate.
- For longer ($> 0.1\mu$m) nanowires, light is absorbed unevenly across the visible spectrum, thus coloring the sample. Different nanowires material give rise to different colors.
- For long enough ($> 2-3\mu$m) nanowires, the sample appears black, with absorption coefficients as high as 95%.
- When the growth of the nanowires exceeds the thickness of the alumina, the longest nanowires reach the top of the channels and start "overgrowing", forming characteristic mushroom structures (see fig 1.5). These irregularities break the photon-NW coupling, and the sample shows the colour of the nanowires metal. Obviously, this behavior is undesirable and growth time should be adjusted to prevent it [26].

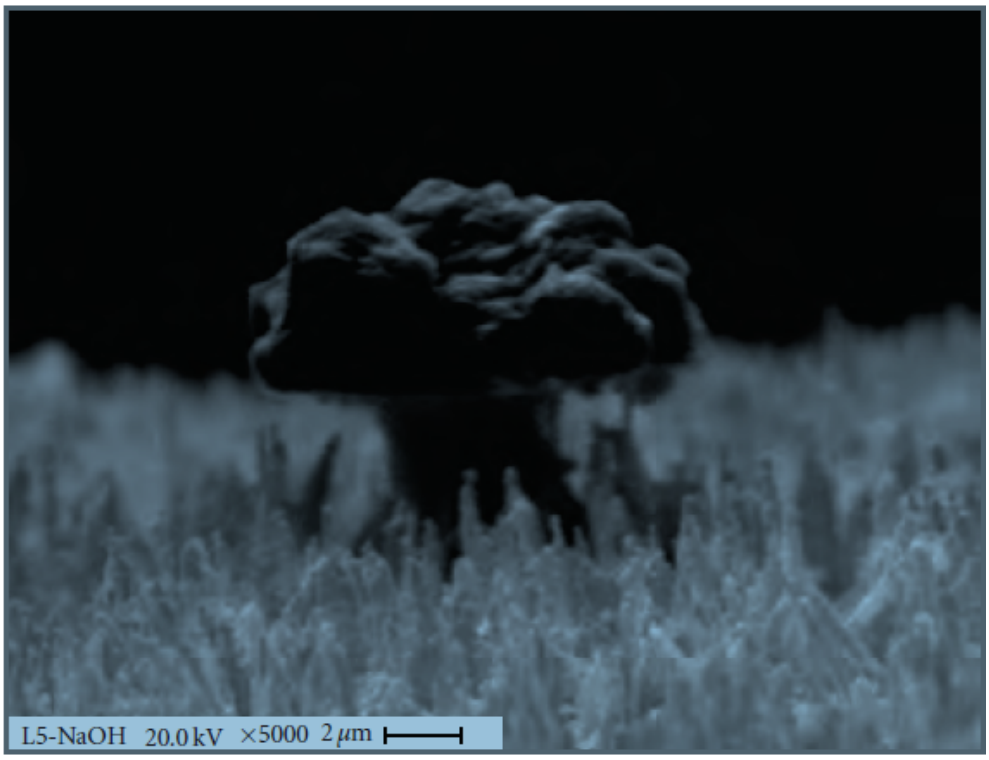

Figure 1.5: Overgrowth of cobalt NW, after the dissolution of the alumina matrix. Once a NW length exceeds that of the channel, it grows irregularly, forming a a "mushroom" [26].

Light absorption of nanowires is - unsurprisingly - dependent on the incidence angle, favoring absorption along the NW axis. This is potentially useful for our applications, since alumina pores (and thus nanowires grown in them) are normal to the surface, and will transport light deep inside the material.

The specific absorption spectrum of nanowires is dependent on a great number of parameters, such as geometry, NWs metal and surrounding material (NWs freed from alumina have a remarkably different behavior) [8, 14].

Energy transport by plasmonic effect

Of special interest to this work is the capability of plasmonic effect to transport energy along the nanowire. As mentioned before, energy can be lost due to photon emission at discontinuities, but most of the energy loss is caused by ohmic heating of the nanowire. In our attempt to optimize volumetric heating of the metal, this is a key property of the NWs.

A useful parameter to quantify energy loss is propagation length, defined as the length along which the propagating plasmon reduces its intensity by e. Measuring propagation length in nanowires is tricky, due to the difficulty of handling single NWs and measuring the intensity of output photons.

Despite this, in recent years, measurements have been successfully performed and theoretical models have been proposed, providing some information of interest for this work [12, 15]:

- Even minor differences in NWs parameters (geometry, material, surrounding material) lead to considerable differences in propagation length. Still, values range between few μm and tens of μm [12].
- Propagation length is considerably greater for highly crystalline (ideally monocrystalline) NWs. Thus, chemically deposited nanowires (such as those used for this work) have usually longer attenuation length than those fabricated via microlithography [**?**].
- Propagation length is sensitive to wavelength, with longer attenuation length at higher wavelengths (see fig 1.6). This is encouraging, since a near infrared laser was used for this experiment.
- Propagation length is greater for NWs of greater diameter.

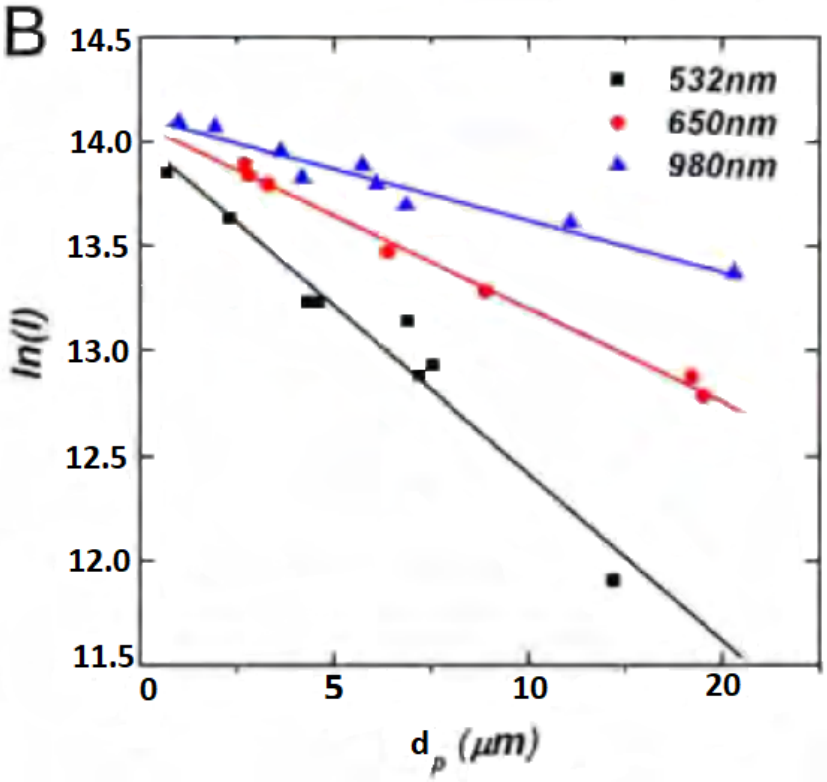

Figure 1.6: Intensity of light after propagation through NWs of different length. As can be seen, intensity decays exponentially with length. The slope is determined by propagation length. As can be seen, propagation length is longer for greater wavelength [15].

Chapter 2

Production of nanostructured targets

Production and characterization of the nanostructured targets was a key part of PLANETA experiment. Producing nanostructures with the desired properties is a delicate and challenging process, and experimentally veryifying the parameters of the nanostructures adds further complexity.

After a brief overview of nanomaterials, in section 2.2, the theory behind the realization of the nanostructured targets used in this experiment will be presented. First, it will be shown how the nanoscale, ordered alumina matrix used as a guide to grow the nanowires is obtained. Then, the methods to chemically grow the nanowires will be presented, and their resulting features will be discussed. Since nanowires of different materials and dimensions were investigated for this work, it will be explained how to control parameters such as diameter, length and regularity during the production process. Finally, the plasmonic effect in nanowires will be briefly discussed. This effect allows a nanowire to act as a waveguide to light, despite having a diameter smaller than the incident light's wavelength.

This effect might be useful to obtain more efficient delivery of laser light into matter, which is of great interest to this work.

2.1 Nanomaterials

Nanotechnology - the fabrication and use of materials with sub-micron features - is a field that attracted huge interest in recent years for a wide array of scientific and technological applications - sensors, optics, electronics, drug delivery, and more.

Broadly speaking, there are two ways to produce a nanostructure (which can be a sphere, rod, ring, or a more complex structure): top-down and bottom-up. In top-down

approaches, nanostructures are "sculpted" out of bulk material with sub-micron removal tools, usually gamma rays or ion beams, a process called microlitography [2]. Top-down approaches allow great control over the process, and are capable of building shapes of great complexity, like sub-micrometer gears. But these techniques are hampered by high cost, low throughput, and resolution limits, often making any practical application impossible [16].

Conversely, bottom-up approaches exploit self-organization of matter in ordered structures under appropriate chemical and physical conditions. Techniques of this kind are cheaper and scalable, allowing to create nanostructured materials in macroscopic amounts. Bottom-up techniques attracted a great deal of research in recent years, and techniques have been demonstrated to build nanostructures in a wide variety of shapes and sizes.

Of particular interest to this research is the fabrication of metal nanowires (NWs). A very effective strategy for NWs fabrication which emerged in recent years is electrochemical deposition in Porous Anodized Alumina Templates. In this process, first an alumina template with deep and regular-shaped channels normal to the surface is created. Then, the channels are filled with metal through electrodeposition. Changing anodization and deposition conditions allow control over the resulting NWs shape and structure. Many different metals can be deposited this way: iron, copper, gold, silver, nickel and cobalt NWs have been fabricated this way [17, 13].

This comparatively simple and inexpensive technique allows fabrication of NWs with excellent regularity, crystallinity and aspect ratio, while allowing high throughput and scalability [18].

In the following subsection, the techniques for making alumina templates and filling the channels with metal will be discussed.

2.2 Anodized alumina templates

Porous Alumina (aluminum oxide, Al_2O_3) coatings were initially employed for decorative and protective purposes, due to their hardness and resistance to corrosion [19]. In the last decade, they emerged as powerful tools for fabrication of nanostructures, thanks to their ability to form regularly shaped nanoscale channels (pores).

Anodization of Al under most conditions leads to formation of a "barrier type" alumina film. A barrier type layer, like that of most anodized aluminum products, is simply a layer of alumina externally coating the bulk Aluminum.

If anodization happens ion acidic pH, with appropriate conditions of electrolyte concentration, temperature and applied voltage, though, the deposited alumina is dissolved almost as quickly as it is deposited, becoming thinner in some places and thicker in others.

But alumina thickness affects the electrical field, which in turn affects oxide dissolution and formation reaction speed.

In appropriate conditions an equilibrium is reached with stable "channels", allowing the flow of ions, forming in the oxide layer. As the oxide layer thickens, the channels are not filled - the film keeps growing in thickness without changing cross-section. This channels, also called pores, are normal to the aluminum surface and will later be used to grow the metal nanowires [21].

These channels have a low variation in diameter - which can range from tens to hundreds of nm, depending on fabrication conditions - and are densely packed in an ordered hexagonal pattern.

While the details of the chemical processes involved are complex and subject to some debate, the occurring electrochemical processes at the anode can be simplified to:

$$Oxide\ formation : 2Al_{(s)} + 3H_2O_{(l)} \rightarrow Al_2O_{3(s)} + 6H^+_{(aq)} + 6e^- \tag{2.1}$$

$$Oxide\ dissolution : Al_2O_{3(s)} + 6H^+_{(aq)} \rightarrow 2Al^{3+}_{(aq)} + 3H_2O_{(l)} \tag{2.2}$$

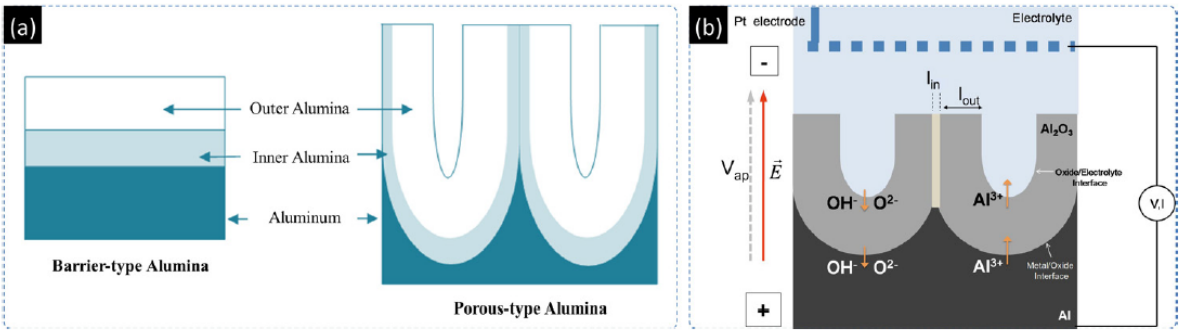

Figure 2.1: (a): Different types of alumina coating. The continuous type alumina is not useful for nanotechnology purposes, while the porous kind is useful for NWs fabrication. (b):Pores - also called channels - formed in porous alumina. Note that an oxide layer (grey) separates the empty channels from the metallic aluminum (black) [16].

As represented in figure 2.1, the alumina produced this way has two different regions. The inner, closer to the metal, is denser and purer, while the outer, closer to the oxide-solution interface, is less dense and substantially anion contaminated. Nanoporous alumina is thus formed of hydrated alumina, water molecules and anionic impurities (which can be up to 15% in mass of the resulting volume). alumina is more dense and pure away farther from the pores' wall, while less dense and comprising more anionic impurities closer to the channels [20]. Note that, no matter the depth of the pores, a thin

layer of continuous barrier-layer is always present at the bottom of each nanopore [20].

Anodization current

The time dependence of the anodization current density j(t) during PAA formation is well established and can also provide insights into the growth process. As shown in figure 2.2, four different stages of anodization can be distinguished [21, 16]:

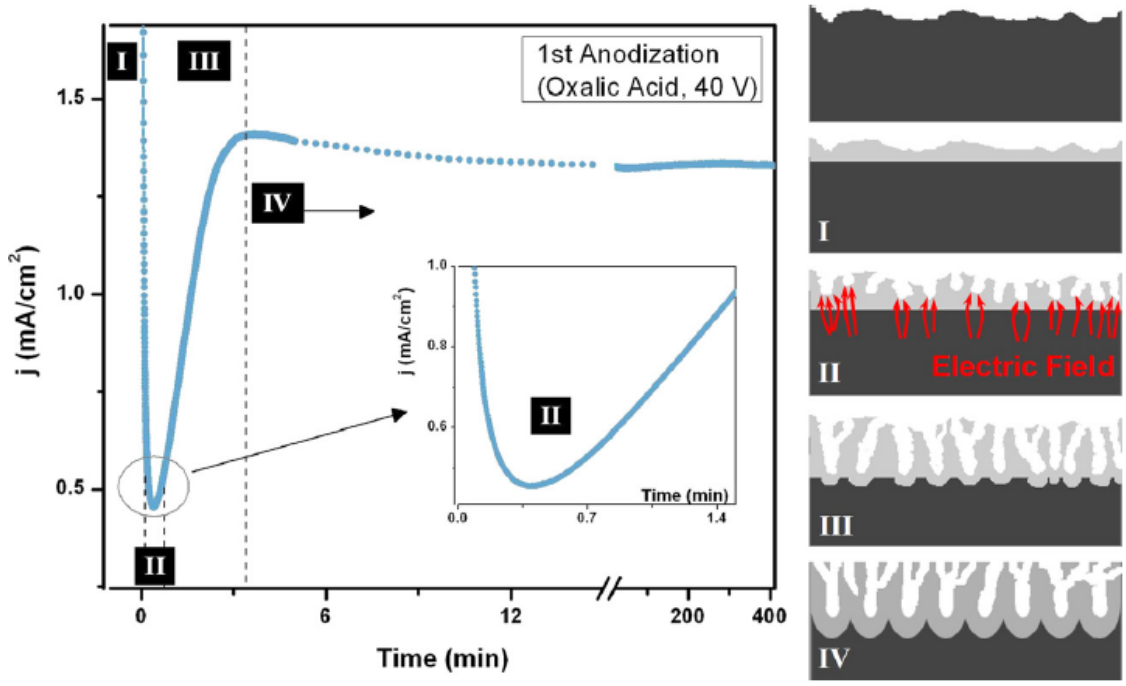

Figure 2.2: Typical behaviour of anodization current over time for oxalic acid anodization. While oxide layer growth rate is different for different electrolytes, the curve has a similar shape in every case. [16]

- **Stage I:** At the beginning of the anodization process, the formation of an oxide barrier layer with high resistivity causes a sharp decrease in j(t).
- **Stage II:** Surface irregularities lead to focusing of electric field lines at specific points. This gives rise to localized heating by electrical dissipation. Higher temperature enhance chemical dissolution of the oxide layer, thus decreasing resistivity. Soon a balance is reached between oxide growth and dissolution, and j(t) reaches a minimum value.
- **Stage III:** Intense dissolution sites nucleate into pores, and channels begin forming. Channels allows ions passage, so j(t) grows quickly to a maximum value.

- **Stage IV:** As channels grow and some close off, j(t) slowly decreases and finally reaches an almost constant value when an equilibrium between dissolution and growth is once again found. From this point, the oxide layer grows at a constant rate.

Channels geometry

An important property of Alumina Templates is *self-organization*: channels are regular in shape and spatial distribution, with a honeycomb-like hexagonal cell structure(see figure 2.3. While there is not yet a consensus over the process behind this pattern, it is thought to be related to an effective repulsive force between the origin points (roots) of the pores. From experimental data and some models, a porosity (percentage of "empty" volume) of about 10% is essential to obtain self-ordered pores [22].

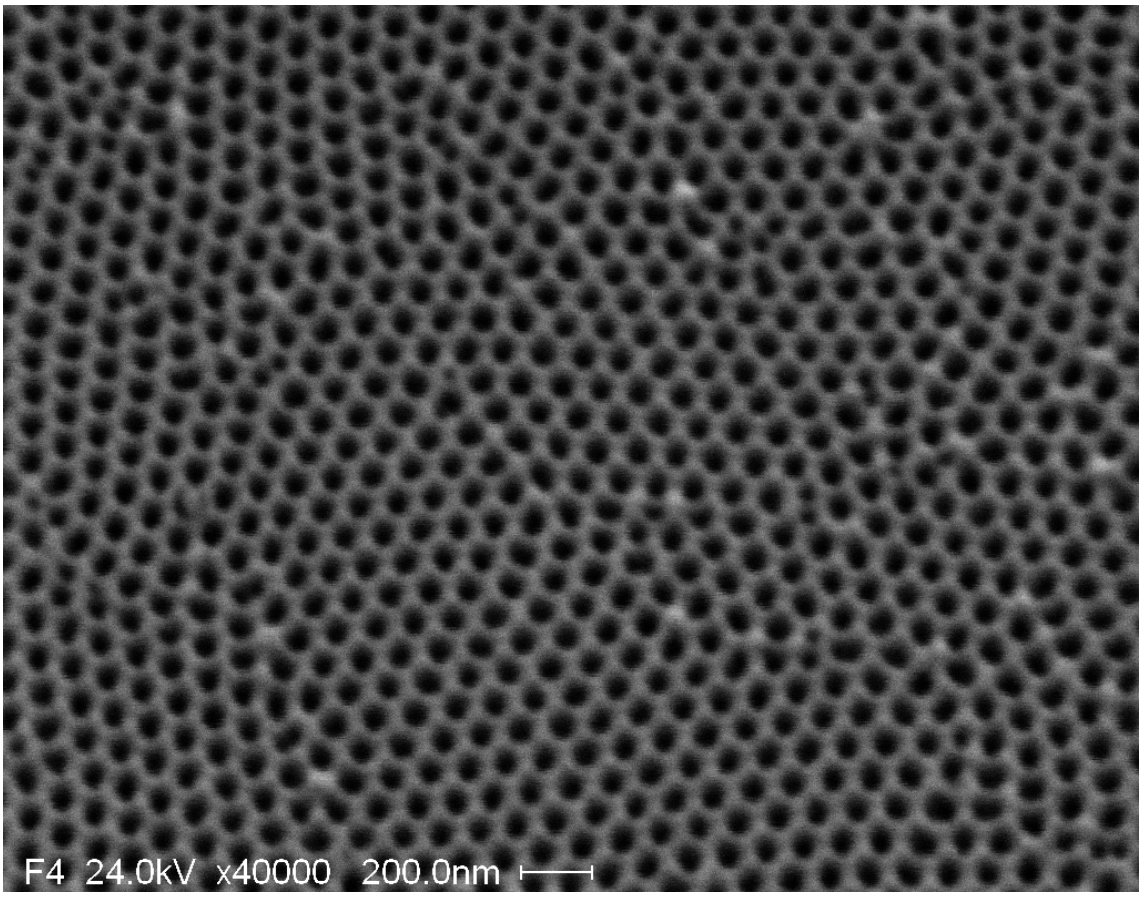

Figure 2.3: Scanning Electron Microscope (SEM) image of nanoporous alumina, seen from above. The very regular honeycomb structure of channels can be noted. In this case, pores are about 60 nm in diameter, but considerably smaller ones, down to 20 nm, can be obtained

The hexagonal cell structure's degree of order depends on purity of the aluminum, electrolyte choice and concentration, temperature and metal grain size. If a highly reg-

ular array is required, thermal annealing (heating and then slowly cooling the material) can increase the metal's grain size, while two-steps anodization (chemically removing the oxide layer and repeating the anodization process) leads to much more regular hex cells [21, 23, 24]. For our needs, regularity of the array was not crucial and single step anodization was used.

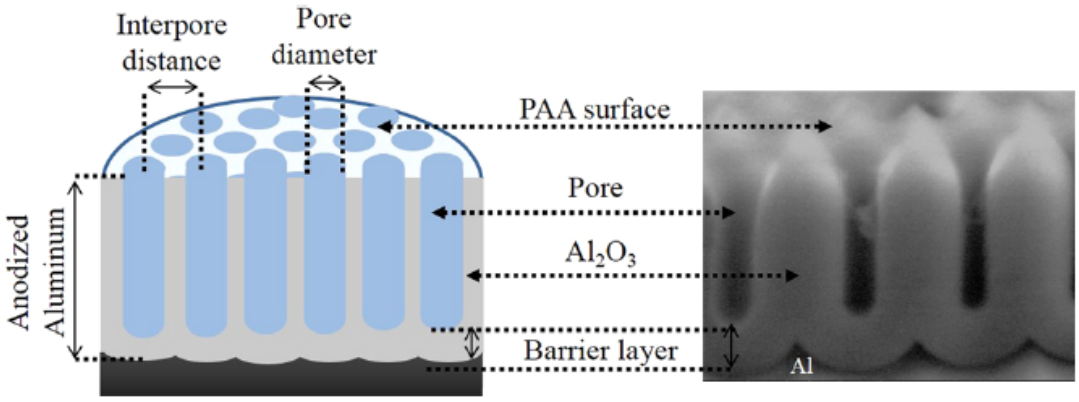

Figure 2.4: Diagram (left) and cross-sectional SEM image (right) of the pores formed by ordered alumina growth. Note the barrier layer formed under the pores [16].

One very important aspect of this process is the possibility of altering the anodization parameters to control the geometrical features of the resulting channels, which will be determine the structured of the nanowires grown inside them. The most important are barrier thickness, pore diameter and oxide layer thickness. It will be now considered how these parameter can be controlled and the range of values which can be obtained [16, 20].

Geometrical parameters: The main geometrical parameters of the alumina template are: [23]

- Interpore distance D_{int}, the distance between the centres of adjacent pores, expressed in nm
- Pore diameter D_p
- Barrier thickness, the thickness of continuous oxide layer at the bottom of channels

Interpore distance is connected to anodization voltage V_{ap}, by the relation:

$$D_{int} = 2.5V_{ap} \tag{2.3}$$

This means the key parameter of the interpore distance (which is closely related to pore diameter, and thus the diameter of the resulting nanowires) can be controlled by

changing the anodization potential. For a given electrolyte, though, anodization potential can be changed only in a narrow range to maintain self-organization.

Therefore, to obtain different geometrical features, different acids must be used at different voltages. In graph 2.5, the different acids used in different voltage regimes are shown. Different electrolytes also require specific concentrations and temperatures to maintain the self-ordered regimen. While some models have been proposed, optimal conditions for porous alumina production have mostly been found empirically.

In table 2.6, the optimal conditions for different values of interpore distance can be found.

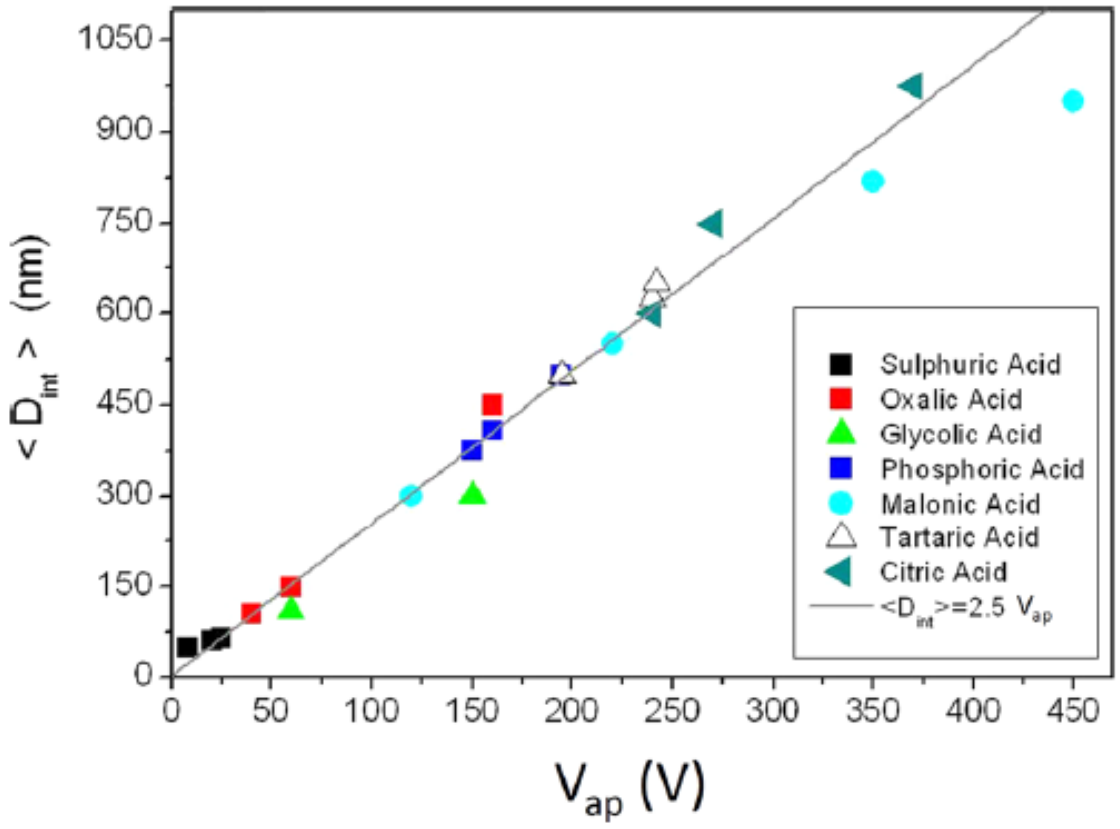

Figure 2.5: Experimental data for interpore distance vs anodization voltage. As can be seen, they are directly proportional over a wide range. The proportionality constant is in the order of 2.5 nm/V. Different voltage ranges require use of different acids. This work's interest is limited to small interpore distance NWs, therefore only sulphuric and oxalic acid (black and red points) have been used [16].

Acid	Sulfuric	Oxalic	Phosphoric
Potential (V)	25	40	195
Concentration (M)	0.3	0.3	0.1
$\langle D_{int} \rangle$ (nm)	65	105	480
$\langle D_p \rangle$ (nm)	25	35	180
t_b (nm)	~34	~50	~250
Porosity (%)	~14	~10	~13
Velocity (μm/h)	5	2.5	5
Temperature (°C)	~1	~4	~1

Figure 2.6: Typical conditions for aluminum anodization using different electrolytes. Temperature, voltage and concentration cannot be changed too much without losing self-organization. Therefore, to create templates with different parameters, different acids are used.

Pore diameter, being closely related to interpore distance, is also proportional to anodization voltage, with a proportionality constant on approximately 1 nm/V.

Taking all this into account, the main way to control D_{int}, and pore diameter with it, is to use different electrolytes. Stronger acids lead to smaller pores. Of greatest interest for sub-visible wavelength applications are sulphuric, oxalic and phosphoric acids. In table 2.6 optimal anodization conditions and resulting parameters are shown. As can be seen, pore diameters ranging from tens to hundreds of nm can be obtained with different electrolytes, but for a given electrolyte the window of anodization conditions is quite narrow.

For a given D_{int}, pore diameter can be somewhat enlarged by chemical pore widening - that is, cutting off the anodization current leaving the sample in the solution, allowing the acid to attack pore walls and thus increasing pore diameter.

As will be shown later, these parameters directly impact the formation of nanowires, which will inherit the pores' geometry.

Oxide layer thickness: Oxide layer thickness is another important parameter, since it determines the length of the channels and the maximum possible length of the nanowires (which can fill the channels only partially, but can't overflow them without losing the ordered structures. Since NWs diameter is independent of the alumina layer's thickness, channel length determines the maximum aspect ratio (length/diameter ratio), which can be relevant to their properties. Layer thickness is mainly determined by anodization time [25]. Longer anodization leads to a thicker alumina layer, in an approximately linear fashion. Thicker oxide layer means deeper channels, allowing formation of nanowires with a higher aspect ratio (length divided by diameter). Channels with a length of tens of μm

can be consistently achieved.

It should be noted that while alumina is more dense than aluminum, its volume is not 100% solid due to porosity (which is in the 10-15% range for optimal anodization conditions), and mass is gained in the process (more oxygen is gained than aluminum is lost). Thus, anodization increases an object's volume, "swelling" its surfaces [22].

2.3 NWs electrodeposition

Once a nanoporous matrix with the desired geometry has been obtained, it can be used to grow nanowires inside the pores.

The electrodeposition method basically consists in the growth of a metallic material on top of a conducting substrate, by the electrochemical reduction of metal ions present in an electrolyte solution. The general electrodeposition reaction can be expressed as:

$$\left(M_x W_y\right)^z + nxe \rightarrow xM^0 + yW \tag{2.4}$$

Where M is the metal to be deposited, W is an ion or molecule bound to the metal ion (usually H_2O or SO_4^{2-}), z is the charge of the $\left(M_x W_y\right)$ complex and n is the amount of electrons involved in the reaction.

Since a fixed number of metal ions is deposited per moved electron, the total deposited mass is proportional to the total transferred charge, which can be estimated measuring and integrating the electrical current during the deposition process. By Faraday's law of electrolysis, deposited mass m is:

$$m = \frac{QA}{nF} \tag{2.5}$$

Where Q is transferred charge in Coulomb, A is atomic mass in g/mol, n the stechiometric coefficient in 2.4 and F is Faraday's constant (96 485 C/mol).

Since NWs diameter is fixed by pore diameter, an immediate consequence of eq. (2.5) is that NWs length grows at a constant rate if deposition occurs at constant current.

However, alumina is non conductive, therefore the barrier layer at the bottom of the pores prevents electrodeposition using DC current. Two solutions are possible: either AC deposition is used, or the barrier must be removed.

AC deposition is possible because the barrier acts in a similar way to a capacitor and current rectifier, allowing growth of nanowires in the pores. NWs deposited in AC are insulated from each other and the aluminum substrate.

To remove the barrier and allow DC deposition, the whole oxide layer can be detached from the aluminum substrate, and the barrier can be removed from the bottom via

mechanical or chemical means, but this requires a thick oxide layer to survive the process. If the opened pores are subsequently coated with metal on one side, this allows DC deposition, but requires a thick oxide layer to survive the process.

A different approach to barrier layer opening is electrochemically etching the barrier from the pores side. This requires very controlled conditions, to avoid destruction of the pores' walls, but if successful, DC deposition can subsequently be used to grow NWs independently of total thickness, and without detachment from the bulk aluminum. It should be noted that, once the barrier layer is opened, nanowires deposited in DC will contact the aluminum substrate directly, thus affecting the electrical behavior of the resulting material.

Chapter 3

Experimental setup

In this chapter, the various part of the experimental setup will be described, along with the methods and detectors used.

The main activity of the PLANETA experiment consisted in producing high-absorbance nanostructured targets and irradiating them with pulsed laser beams. Several kind of detectors, which will be described in later sections, gathered data on plasma formation and evolution during and immediately after the laser shoot. In a later phase, the targets were analyzed with optical microscopes and Scanning Electron Microscope (SEM) to study the effects of irradiation.

Sample production and characterization, both before and after irradiation, took place at the INFN microscopy laboratory in Bologna. As for irradiation, two different facilities were used, in order to have access to laser beams with different optical parameters, wavelengths in particular. One was the at the LENS (Laser Energy for Nuclear Science) facility at the INFN LNS (Laboratori Nazionali del Sud) site in Catania, where a 2 J, 1064 nm (infrared) laser was used. The other facility is an INFN laser with 532 nm (green) and 1.4 J, located at the physics department of the University of L'Aquila.

3.1 Target production

During the three years of experimental activity, samples were produced in Bologna with a wide range of different geometrical and chemical features, to test the effect they had on the resulting plasma. The most important parameters which varied between the experimental samples were:

- NWs metal. Since different metals differ in electrical conductivity, melting point and X-ray emission lines, this research meant to test how chemically different NWs reacted to irradiation. However, not all metals are suitable for the deposition tech-

niques that were employed. Nanowires made of cobalt, iron, nickel and silver were produced and irradiated during the experimental activity.

- Nanowires diameter. As previously explained, NWs diameter can be controlled by using an appropriate electrolyte and the appropriate anodization voltage, so it can be changed only within discrete ranges. Since this research was mostly interested in nanowires much thinner than incident light's wavelength, sulphuric and oxalic acid were used, allowing to produce 20 and 50 nm thick wires, respectively.
- Nanowires length. It was part of the experiment's aim to determine if longer nanowires led to different plasma parameters, and if so, at what point would the length effect reach saturation. Since length can be controlled by changing anodization and deposition times.
- Electrical contact. As explained in section 2.2, it's possible to produces nanowires either directly in contact with the underlying aluminum, or separated by a thin - but electrically insulating - alumina layer. Samples of both kinds were produced, to better investigate the role of electrical conduction in producing the plasma.

Control samples:

Each sample was anodized (and filled with NWs) along with a smaller control sample cut from the same aluminum sheet, to be used for quality control. This control sample, which is expected to have identical nanostructures to the main sample, can be used for destructive analysis (for example, cutting it to observe its cross-section with SEM) to directly observe the size and quality of nanostructures.

3.1.1 Samples characterization

While NWs parameters can be roughly calculated from anodization and deposition time, the actual samples must be analyzed before irradiation.

For each sample, the control sample was analyzed with SEM to measure nanowires parameters. After that, the whole samples were observed with an optical microscope capable of 3D scanning. In addition, some samples were analyzed with a spectrophotometer to measure they absorbance at different wavelengths.

SEM analysis

The most important way to analyze samples before subjecting them to irradiation is SEM analysis, in order to measure nanowires diameter and height, which can't be measured with any optical microscope since NWs are thinner than visible light's wavelength.

A Philips 515 Scanning Electron Microscope, able to reach 40 000x magnification, available at the INFN microscopy lab in Bologna was used.

Since nanowires are normal to the sample's surface, and don't feel it completely, they can't be seen from the top. Therefore, the control strip was purposefully cut. The exposed nanowires in the cut region were imaged from the side, which allowed a good measurement of height, since it's easy to see until which point the nanopores are filled with metal.

To measure NWs diameter, finding nanowires free from the alumina layer was preferable, so a region in each strip was chemically etched to dissolve most of the alumina (see image 3.1). This freed the nanowires, causing them to collapse in clumps, which allowed clearly resolving and measuring single nanowires.

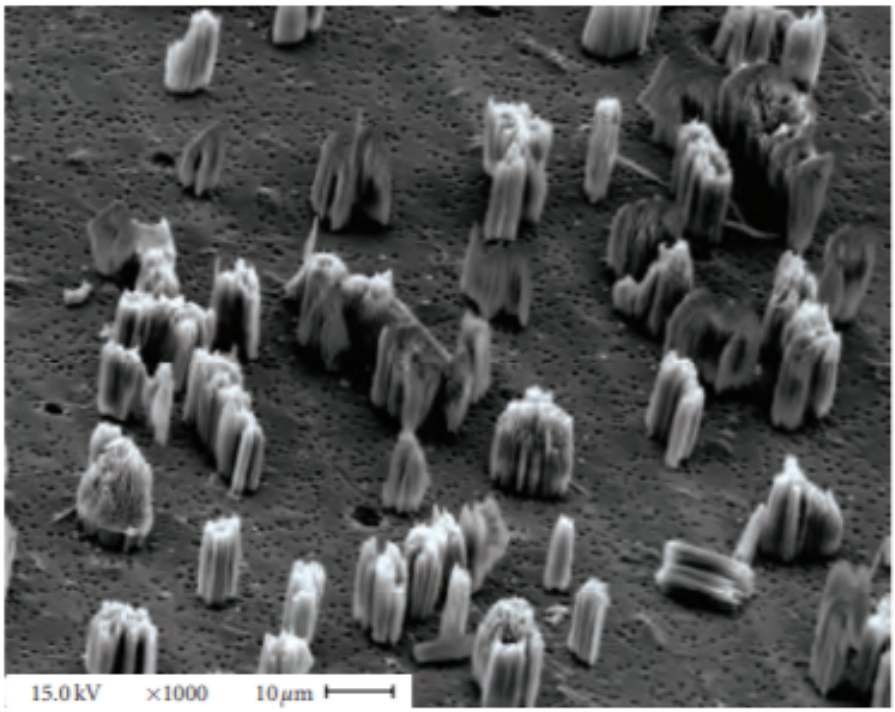

Figure 3.1: Clumps of nanowires after chemical etching. Image from [13].

Surface microscopy

A Huvitz HDS-5800 optical microscope, capable of 3D reconstruction of targets, was used to observe the sample before irradiation. No visible microscope can observe the nanostructures, so the interest was in assessing roughness, irregularities or other micrometer-scale features.

It was soon found that all samples are smooth within the micrometric resolution available, and the surfaces were featureless for all observed samples, until the sample

was irradiated. After irradiation, surface microscopy allowed to study the craters and other surface modifications of the targets.

3.2 The 1064 nm laser setup at INFN-LNS

Most irradiated samples (which will be called "targets" in this section) were shot by a pulsed laser at an INFN facility (Laboratori Nazionali del Sud) in Catania, in several phases from 2016 to 2018. A second laser setup was available for the PLANETA collaboration at L'Aquila, but due to hardware upgrades it was only used for a short data taking phase in 2019.

Data from various detectors were collected during irradiation and later, once the targets were returned to Bologna , craters were analyzed at SEM and optical microscopes. In the following subsection, the laser setup and the detectors will be described.

3.2.1 Laser setup

Targets were placed inside an interaction chamber, held in position by a metal target holder which can be moved with great accuracy, providing the desired spacing between shots. The elements of the irradiation setup (not considering the detectors) are:

- **Laser:** A Q-switched solid state Nd-YAG laser has been used for irradiation. It fires in 6 ns long pulses, with a maximum rate of 10 Hz. It emits light in the near infrared, at 1064 nm wavelength. Each pulse carries a nominal maximum energy of 2.2 J. The laser beam is generated outside the chamber and has a diameter of 2 cm, so before reaching the target it crosses a transparent window and a convergent lens.

- **Interaction chamber:** Lens, target and some detectors were all contained in a 800 mm diameter cylindrical interaction chamber, pressure of 10^{-4} torr.

- **Focusing lens:** a fused silica plano-convex lens with focal length 67 mm focuses the beam on the target. The incoming laser beam makes a very small angle (few degrees) with the focal axis of the lens, in order to avoid that light from the target is focused back towards the laser. Between the lens and the target there is a thin sheet of transparent Mylar, to avoid condensation of ablated material on the lens. The laser beam should shrink to about 200 μm diameter on the focal spot. As will be discussed later, proper laser focusing was found to be a key parameter to get reliable data.

- **Target holder:** a metal target holder has been employed to keep the target in position, and to connect it to the movimentation system. Since preliminary data suggested a problem with lack of planarity of the target holder, a new one was produced at the INFN Bologna workshop and used for the data taking.

- **Movimentation system:** The target holder is connected to a movimentation system which can move in three dimensions. It is used first to change the distance of the target from the lens (z axis movement) in order to find the focus position, and then to shift to target in the x-y plane between shots. It allows x-y-z movements with 1 μm increments, in a 26 mm range. The normal to the target is kept at an angle of 30 degrees relative to the incoming beam, so that planarly reflected light does not go back toward the laser.

Images 3.2 and 3.3 show the inside of the interaction chamber.

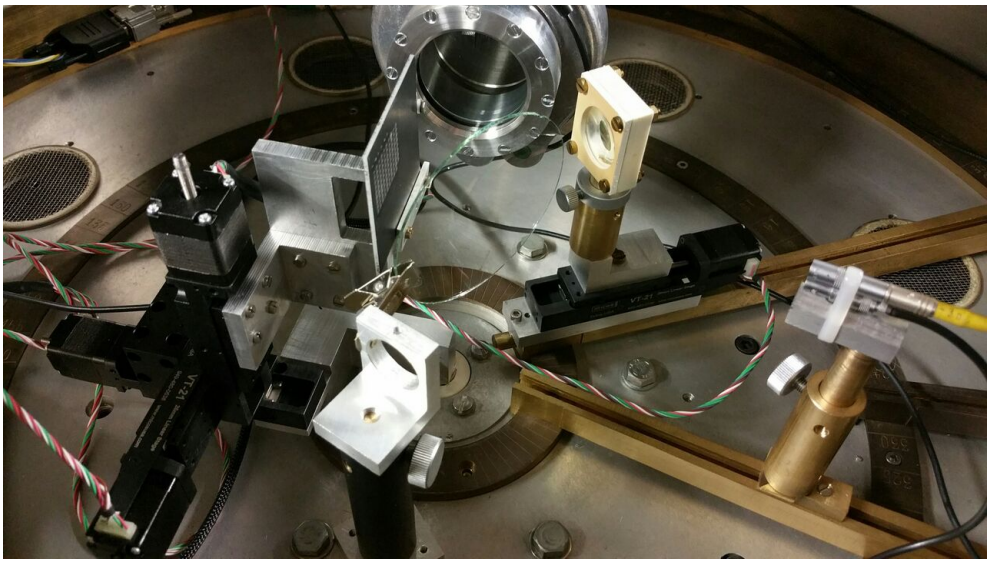

Figure 3.2: Vacuum chamber at LNS laboratory. The lens can be seen in its white plastic case, along the laser beam path.

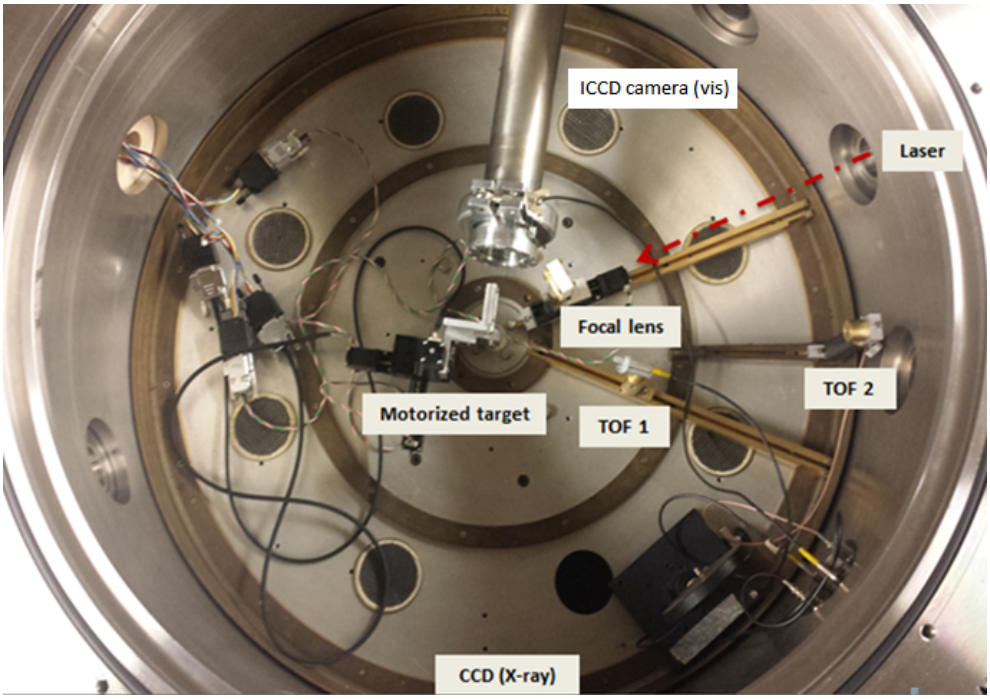

Figure 3.3: The target can be seen in its holder. On the right, a top view of the camber can be seen, with the different detectors and instruments labeled.

3.2.2 Laser and optics

The laser beam is generated outside the chamber, and crosses an optical bench before entering the vacuum chamber through a plain glass window. The optical bench allowed to manipulate the beam before it entered the chambered.

After several setup upgrades and modifications, the optical bench setup which was used for most data takings (see figure 3.4) was:

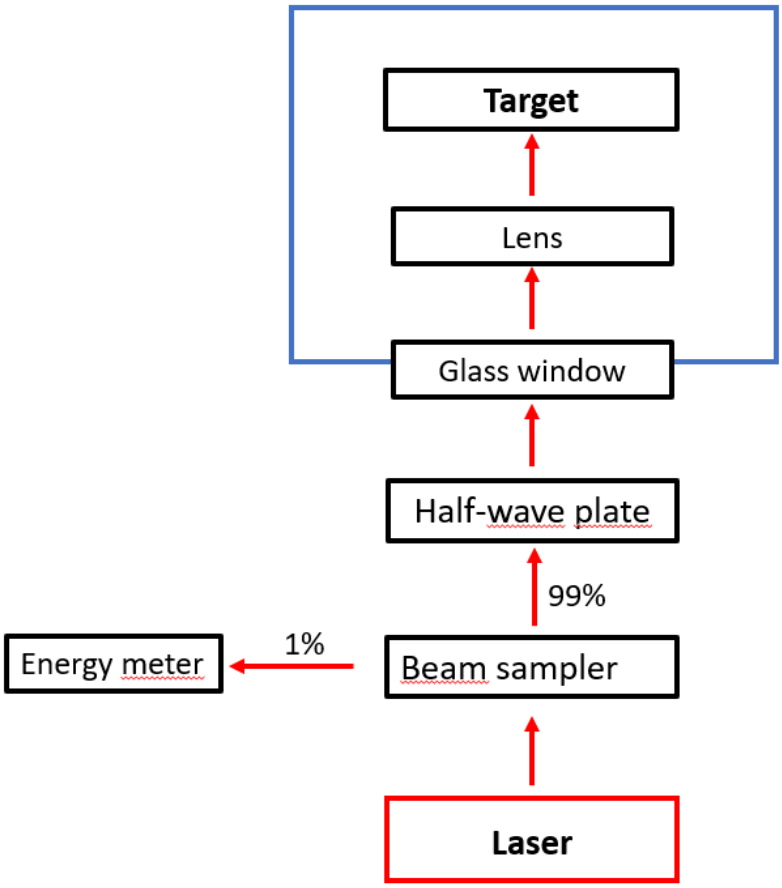

Figure 3.4: Schematic representation of the optical setup used for the experiment.

- **Laser**: A QUANTA system Q-switched solid state Nd-YAG laser has been used for irradiation. It fires in 6 ns long pulses, with a maximum rate of 10 Hz. It emits light in the near infrared, at 1064 nm wavelength. Each pulse carries a nominal maximum energy of 2.2 joule, but as will be shown, actual maximum energy was found to be 1.9 J. Inside the laser, the beam passed through two different population-inversion crystals. The pulse is generated in the first, and the second acts as an amplifier, to allow a large range of energies (between 0.5 and 1.7 J) to be used. Light emitted from the laser is linearly polarized.

- **Aim pointer**: a low-power, red laser pointer closely aligned with the main beam allowed to correctly position the optical elements and the target along the laser's path.

- **Beam sampler**: a beam sampler optical element extracted a small percentage of the beam (about 1%) to measure the energy shot-by-shot, while allowing the beam to reach its target.

- **Energy meter**: a Thorlab energy meter model S220C based on a pyroelectric sensor measured the energy for a given laser shot. It could be moved on the main beam line for calibration, or on the sampled beam to provide online energy measurement during operation. It has a 25 μJ resolution and a 5% uncertainty.

- **Half-wave plate**: a birefringent half-wave plate allowed to rotate at will the laser's linear polarization. Note that the laser light produced by Q-switching is inherently linearly polarized, but the polarization plane is fixed. This allowed to control the polarization angle relative to the target's surface.

- **Windows**: a plain quartz window allowed the beam to enter the vacuum chamber. During setup, the beam's energy was checked before and after the window, and it was found that only a negligible (<1%) amount of the beam's power was lost in it.

- **Lens**: A plano-convex lens focused the beam on the target's surface. The lens was 5 cm in diameter, to make it substantially larger than the beam, and had a focus length of 67 mm.

Additional elements, like a polarimeter to check polarization and special thermosensitive paper to measure the beam width, were temporary added when necessary.

Using the energy meter, energy loss was checked after each element, from the laser to the target. As expected, only the beam splitter diverts a meaningful amount of energy from the main beam, with power loss after the beam splitter <2%.

While this was the setup during data taking, further elements could be added, like a calorimeter for energy measurement calibration, and a polarimeter to check the polarization plane.

Energy measurement

At first, pulse energy was measured with a calorimeter, which could be added to the optical line to completely absorb the beam, and provide a measurement of energy by averaging over many shots (since it needed to reach a stable thermal equilibrium to provide an energy measurement).

While this calorimeter allowed to measure the actual energy output - which was found to be substantially lower than nominal - the beam energy needed to be measured shot by shot, and without preventing the beam from reaching the target.

For this purpose, the aforementioned pyroelectric sensor and beam-splitter were added. By systematically recording series of shots at different power settings, it was found that shot energy is more stable (variance within 2% of mean) for high-energy shots and somewhat less stable (within 5% at lower energy). It was also found that the

first shot in a series has a tendency to spike by up to 10% if the laser has been inactive for a few minutes, so the precaution was taken to fire a few shots with an absorber blocking the window before actually firing on the target.

To calibrate the pyroelectric energy meter, which directly measures the extracted beam, series of shots were fired with the sensor across the main beam line and then across the extracted line. This way, a conversion constant between the values measured on the extracted beam was found to be constant for all low energies, as expected. Since the higher energy values on the main beam could damage the sensor, it was compared to the previously mentioned calorimeter. Within its sensitivity, it found the same proportionality factor between sampled line and beam line. Thus, during data taking it was assumed the same constant was valid at all energies (even if it was re-calculated for each data taking phase, to account for possible changes to beam parameters during maintenance).

Beam divergence

To reach high power densities on the target, the beam (about 1.2 cm wide at the source) had to be focused to a narrow spot. Since direct measurement of minimum spot size is impractical, it was necessary to calculate it from beam parameters.

For a diffraction-limited Gaussian beam, minimum spot size is a function of divergence as follows:

$$R_{spot} = \theta * F \tag{3.1}$$

Where F is the lens' focal length and θ is half-angle divergence in radiants.

Divergence is the aperture angle of the laser's beam (see figure 3.5. It should be noted that, due to fundamental physical constraints, divergence can't be decreased by any optical system, so minimum spot size was ultimately dictated by the laser beam's optical properties at the source.

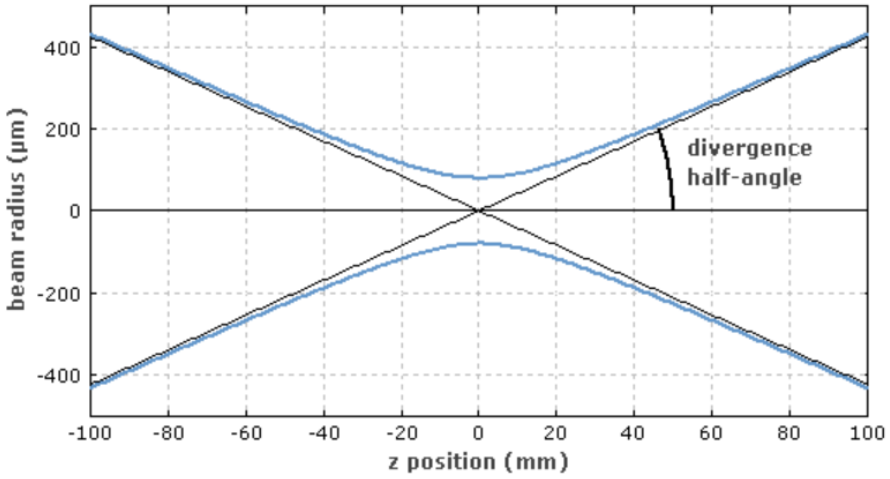

Figure 3.5: A schematic representation of the divergence angle.

While nominal full-angle divergence for the laser beam was 0.5 mrad, its enlargement before entering the chamber was noticeable higher, so it was decided to take a measurement. At high energy the beam profile could easily be seen on any absorbing target, even if the lack of a sharp edge made the measurement subject to substantial uncertainty.

To get as accurate a reading as possible, the vacuum chamber was partly disassembled and the beam's width was measured at the farthest point of the room. The beam's divergence was measured at different points, and the results can be seen in table 3.6. The result is 2.6 mrad, much larger than the nominal value, and consistent with the observed spot size on the target.

	Distance cm	Diameter mm	Divergence mrad	Err div mrad
Laser out	0	11		
Chamber in	150	15	2,5	0,3
Chamber out	237	17	2,6	0,3
Far wall	644	29	2,7	0,3

Figure 3.6: Full-angle divergence measured at different points: just in front of the laser, before the vacuum chamber, after the vacuum chamber, and as far from the laser as the room physically allowed. Since the laser's edge isn't sharply defined, 1 mm measurement was taken as uncertainty for beam width. The divergence value calculated on the three points is consistent within uncertainty.

As will be shown in the next section, assuming a Gaussian beam profile, this leads to estimate a 194 $\pm 20\,\mu$m diameter spot size, which is comparable to the marks observed

on the targets after irradiation.

Beam focusing

Since energy deposited on target falls quadratically with spot diameter, maintaining good and consistent focalization was required to obtain reliable data.

Focusing the laser beam with the required accuracy proved challenging, and our methods and technologies changed during the experimental phases. While it was possible to move the lens with 1 μm accuracy, the lens-target distance could only be roughly estimated.

To initially find the position of best focus, targets were shot repeatedly and metrics from the resulting plasma were used to find the best focus position. At first, data from TOF detectors was used to find the best focus, assuming the best focus would lead to faster ions, and thus lower time of flight. However, it was soon noticed that integrated X-ray measurement had a clearer and more consistent response to lens-target distance, so best focus position was chosen by maximizing X-ray flux.

During preliminary data takings, though, it soon became obvious that a single best focus distance couldn't be assumed to be valid for the whole target. This is because targets aren't perfectly planar, often retaining a small curvature from the cutting process, and sliding the targets to fire new spots might cause small variation in distance due to misalignments.

At first, this was corrected by finding the best focus position at the corners and the sample, and adding a linear position correction to shots on different parts of the target. When this system, too, was found insufficient to ensure consistent focalization, it was concluded that a shot-by shot position measurement was required.

In 2018, a distance monitor was added to the setup. After finding the best focus in any point of the sample with a fine Z-scan, every planned firing point was scanned with the distance monitor, then corrected to keep a fixed distance between target and lens. This allowed to reliably keep the target in focus, which in turn substantially lowered the spread of measured fluxes from events with the same beam parameters, improving our resolution.

To find the best focus, nine (or more) shots are fired on the target, moving the lens closer or farther from the target and measuring x ray flux (detectors will be described in section 3.2.4), on the assumption that the best focus yields the brightest X-ray flash, since it achieves the maximum power density.

It was noticed that focalization curves - X-ray flux relative to lens position - at different energies provided different results, as it can be seen in figure 3.7. At higher pulse energy, X-ray flux is less sharply dependent on focus position, with a larger plateau

around the maximum. Interestingly, the maximum also has a 0.1 mm offset compared to lower energies, with the best focus lens position at higher energy farther from the target compared to low energy pulses.

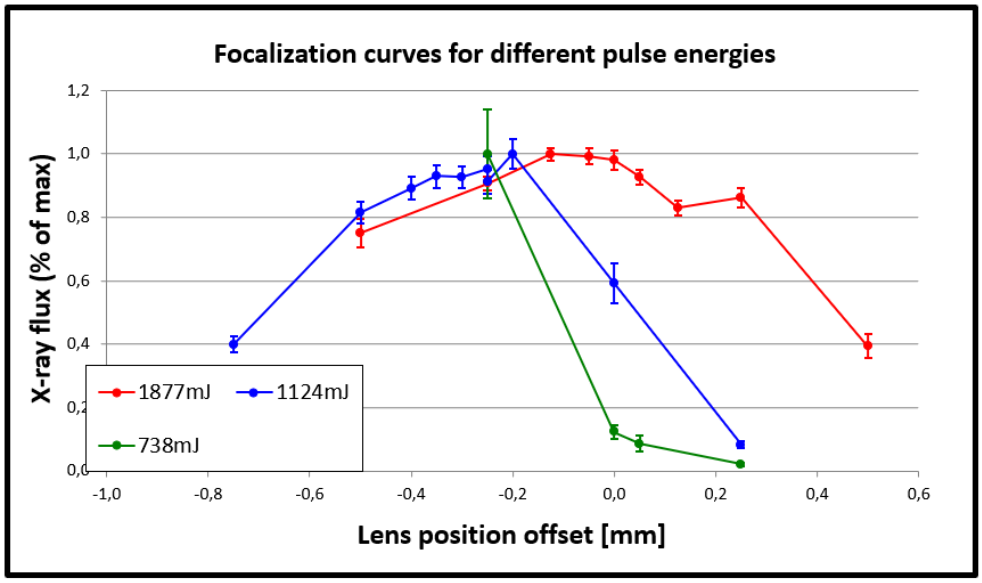

Figure 3.7: X-ray flux vs lens position for different pulse energies. Flux is shown normalized to maximum, and position is relative to best focus.

Literature suggests that this happens because at high power density, focusing the beam on the plasma plume (in front of the target) leads to the highest X-ray emission. However, since our interest lies in light-matter interaction, it was chosen to take the lower energy focus position as the correct one. This also allows for greater precision, since the X-ray flux falls more sharply with distance from the best focus.

To better study the relation between distance and focus, the X-ray flux response was scanned in a $\pm$ 1 mm range from the best focus position. The results can be seen in figure 3.8. As it can be seen, at just 0.2 mm from the maximum, flux falls by more than 50%. This highlights the importance of a consistent and reliable focalization.

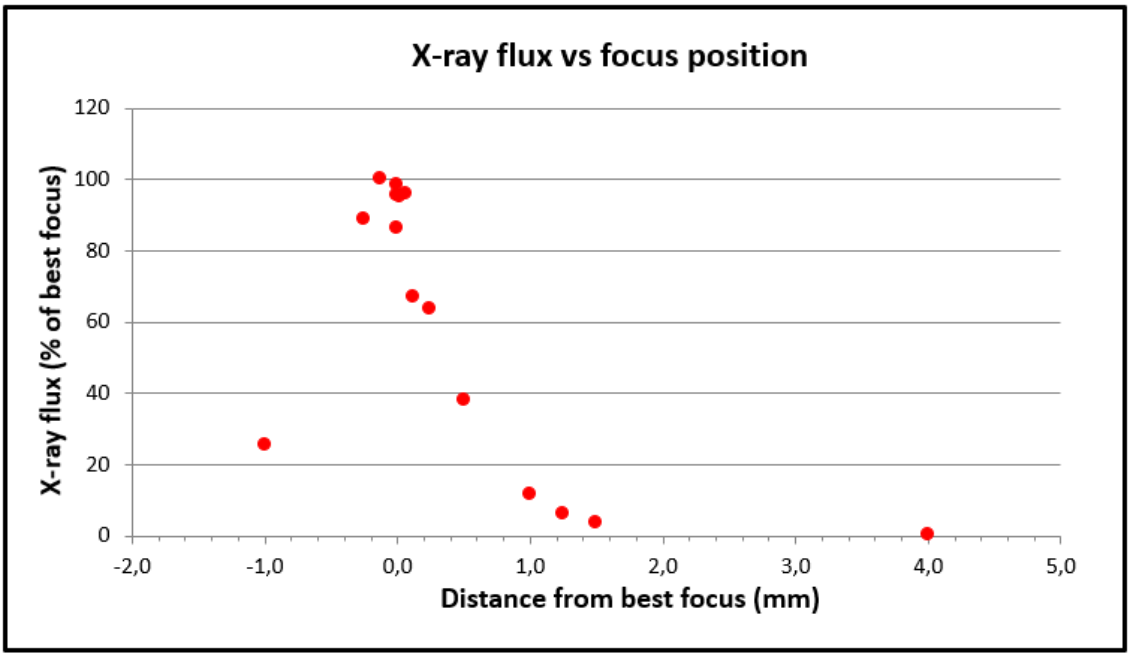

Figure 3.8: An example of the focalization curves used to find lens-target position. Flux is shown normalized to maximum, and position is relative to best focus.

3.2.3 Interaction chamber

An 80 cm diameter (inner size) interaction chamber was used to contain the sample and some detectors, while other detectors are located outside the chamber volume. From the control station outside, it was possible to move the target holder to shoot a different point on the target every time, and shot-by-shot data were collected by several online detectors. This way, once the chamber was sealed and air pumped out, there was no need to open it again until the whole target surface had been shot.

Once the chamber was manually closed, a rotary and a turbo pump were activated in sequence to lower the pressure down to 10^{-4} torr.

The interaction chamber included the following elements (detectors will be described in more detail later):

- Sample holder: The sample holder (see figure 3.9) was designed to hold and move the target, keeping it flat and allowing fine (<5 μm), repeatable movements. Tracks and electrical actuators allowed to move the sample on the X and Y axis, Z being the normal to the target's surface. Total movement range was 25 by 25 mm, so the targets were usually shot in a 2 mm grid, allowing up to 144 shots. Most samples were rectangular, 26 by 60 mm in size, allowing to shoot the same target twice in different sessions. A further actuator allows to rotate the sample, changing its angle relative to the incoming laser beam. Keeping the sample at an angle was

necessary to avoid coherent reflection of the beam back into the optical line, and also desirable to study response to polarization.

- Distance meter: as discussed in the previous section, an accurate measurement of target distance is crucial, so a distance monitor is located inside the chamber, allowing to measure the sample-lens distance while the sample is moved. The distance meters project a low-power laser beam on the target's surface and measures the distance trigonometrically by detecting its reflection. It has a 6 μm resolution, sufficient to stay within the best focus zone.

- TOF collectors: negative biased, open-ended LEMO cables were placed inside the chamber, in different positions, to act as ion collectors for time of flight measurements. Different placements have been tried over time to gather different kind of data, but they were usually placed at least two different distances for better TOF measurement.

- CCD camera: an Andor DY920P model back-illuminated CCD camera provided data on X-rays emission from the plasma. To gather information about X-rays energy, a hole mask was applied to the camera, with foils of aluminum of different thickness (in a 3 to 17 μm range) in front of each hole. Comparing the flux through each pinhole allowed a rough estimate of the energetic emission spectrum of the plasma in the few keV range.

- ICCD camera: Two more detectors, a CCD camera sensitive to X-rays and an ICCD (Intesified CCD) sensitive to visibile light, are placed outside the chamber but observing the interaction region, respectively through a vaccum pipe and a glass window. More details of such detectors will be given in the next sections.

- Lens: A plano-convex lens, described in more detail in the previous section, allows focalization of the laser beam on the target.

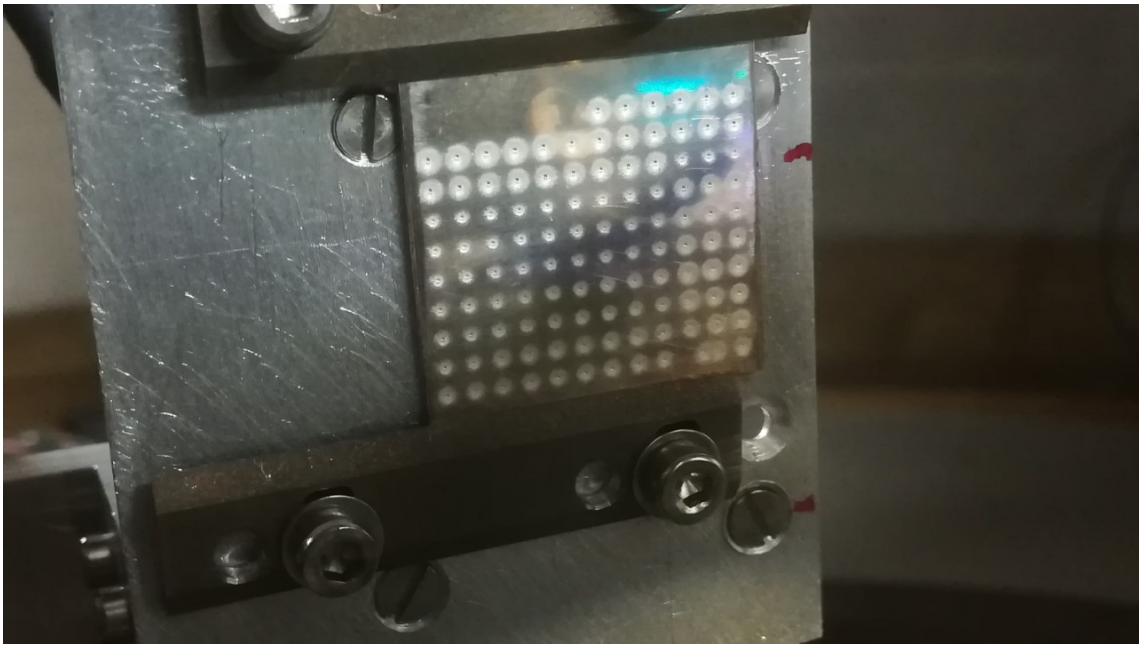

Figure 3.9: The sample holder with a mounted target, already irradiated.

3.2.4 Detectors

In this section, the detectors used to analyse the results of laser-target interactions are presented in detail.

ICCD camera

An ANDOR ICCD (Intensified Charged Coupled Device) camera, positioned 23 cm from the target at low incident angle, has been used to gather time-resolved data about the expansion profile of the plasma plume.

Intensified CCD sensors allow to image low energy photons (in the 200-900 nm range) that wouldn't usually cause electron-lacuna couples in the silicon, and thus would be undetectable. To achieve this, they couple a front-illuminated CCD camera with a gated intensifier via a lens system, as shown in figure 3.10.

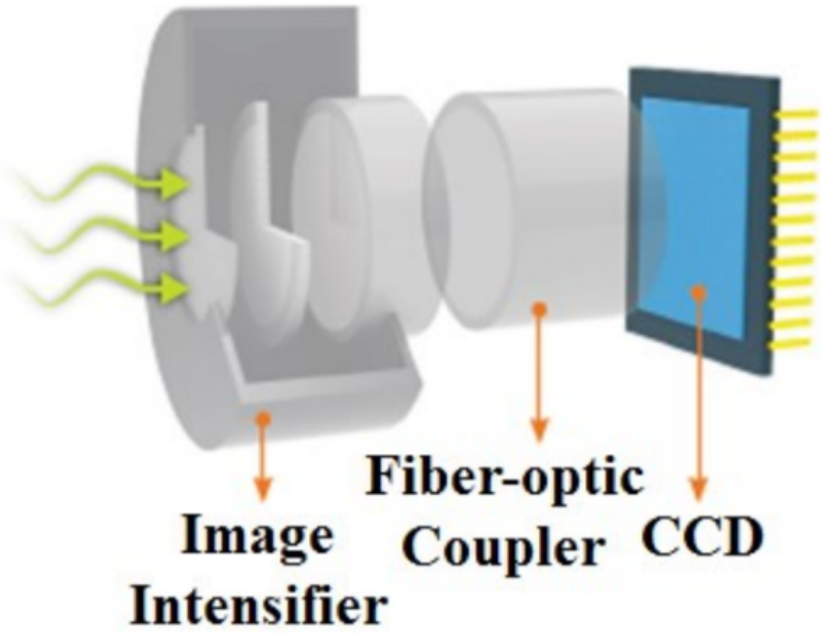

Figure 3.10: Schematic representation of an ICCD camera

The intensifier is the key part to allow imaging of low energy photons. It's in turn comprised of three elements, enclosed within a vacuum tube: a photocathode, a microchannel plate and a phosphor screen (see image 3.11). The photocathode emits photoelectrons when struck by a photon. A strong electric field accelerates the electron toward the microchannel plate (MCP). The MCP is a honeycomb of glass channels (5-10 μm in diameter) where the high potential accelerates incoming electrons. As primary electrons collide with the MCP walls, they produce further electrons, which are accelerated in turn. The end result is a cloud of electrons exiting the MCP with the same 2D spatial distribution of the original photons.

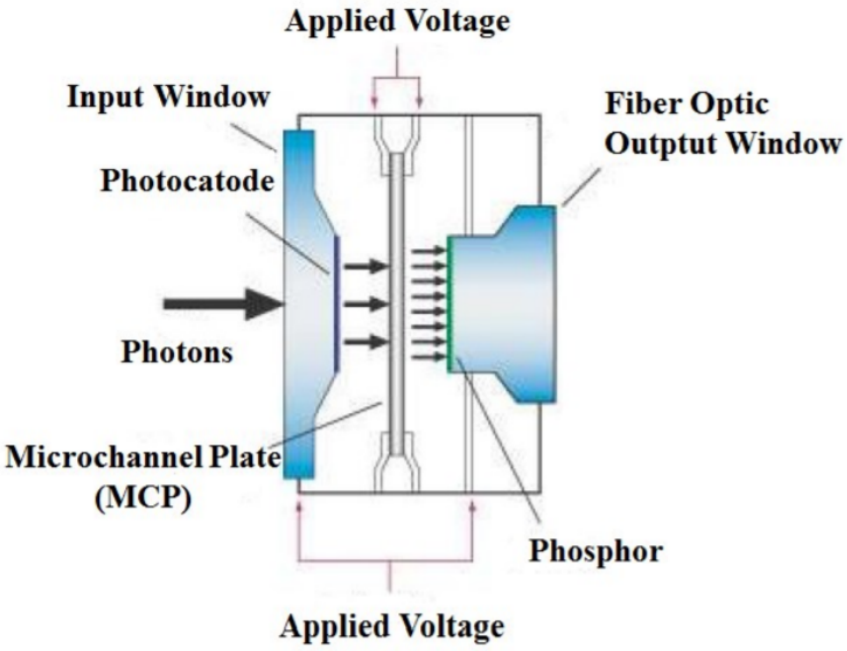

Figure 3.11: Schematic representation of the light intensifier element of the ICCD camera

These electrons, in turn, reach a phosphor layer after the MCP, emitting photons energetic enough to be detected, and this phosphor is coupled to the CCD sensor via optical fibers.

It records the visible radiation coming from the plasma in the wavelength range 200–900 nm, as shown in figure 3.12.

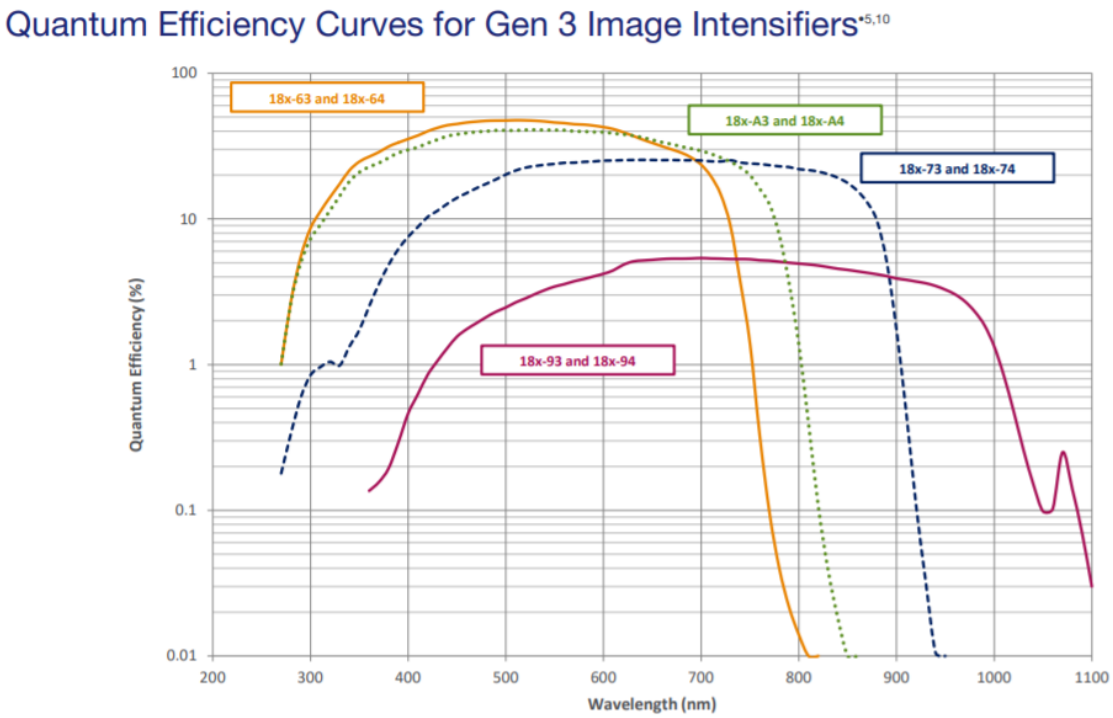

Figure 3.12: Quantum efficiency of the ICCD camera (red curve)

The camera has a 1024x1024 sensitive surface, with 26 μm pixels, allowing detailed spatial resolution. The camera allowed for fast gating, allowing to take snapshots of down to 3 ns exposure . Read-out time was far too long (> 1ms) to take repeated snapshots of the same event - visible signal is detectable for about 200 ns. But since many laser shots were taken with identical parameters, it was possible to obtain time-series of comparable events by taking one snapshot with a different delay for each of a series of shots. This way, the time evolution of a "composite" event could be observed.

Operating the camera presented a few difficulties - for each sessions, it had to be carefully aligned relative to the target, and a small change of alignment could send the interaction point out of the camera's narrow field of view, or directly expose the inside of the crater (which leads to saturation of the involved pixels).

X-CCD camera

An Andor DY920P-BN model back-illuminated CCD camera, which is sensitive to low energy X-rays, was used to study the X-ray emission from the plasma. This camera was placed at an angle of 60 degrees from the target normal. The camera has a 1024x512 pixels, each 26x26um, and is sensitive from about 10 eV to 10 keV (see figure 3.13]. The camera integrated over a comparatively long (hundreds of nanoseconds) time, obtaining a time-integrated image of the event.

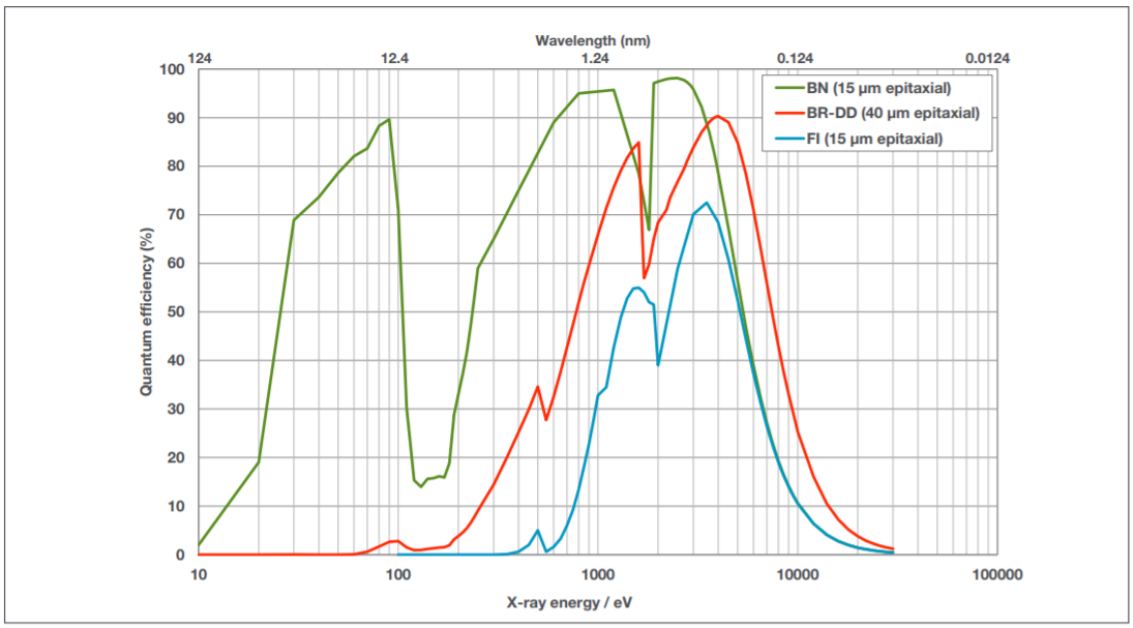

Figure 3.13: Quantum efficiency of the CCD camera (green curve)

Due to the intense flux of X-rays from the plasma, the camera needed filters to avoid pixel saturation. Two different kinds of filters were placed in front of the CCD, at about 10 cm distance. At first they were used separately and then combined, to obtain different operating modes.

The first filter was thick metal frame, with a grid of holes bored through it, and each hole covered by thin aluminum foil of different thickness. This way, the flux from the plasma was completely blocked outside the hole, while the aluminum filters over a mask with 1 mm diameter holes allowed partial transmission, forming "spots" on the resulting image (see image 4.27). The filters were selected thin enough that many photons reached each pixels, leading to a constant intensity over the spot. This way, while there was no information about single photons, the average flux of different events could be easily compared.

Since traversing thicker filters leads to beam hardening, comparing the ratio of signal through different absorbers, in principle, yields information about the spectral composition of the source. Several sets of filters were made and tested, but while they were very useful to get an averaged flux measurement, the differences in ratio between thinner and thicker filters were too small to provide spectral information in any detail.

The other kind of filter used was a single, continuous layer of Titanium (to reduce spectral distortion, compared to aluminum), which covered the entire sensitive surface. With an appropriate thickness, it's possible to reach single photon regime, so that most pixels are hit by at most one photon.

Since pixel counts are proportional to the charge deposited in them, if a single photon

hit the pixel its energy can be measured. With a sufficient number of photons (several events with the same parameters can be used to expand the statistics), the source's energy spectrum can be reconstructed. This is called Single Photon (SP) operating mode.

There were several practical problems in reconstructing spectra from SP data, which will be discussed in the next chapter, but it still turned out the be the best way to obtain spectral information.

In the end, the two kind of filters were mixed to obtain the maximum amount of information: while SPC is best for spectral analysis, a mask with holes covered with filters of different thickness allowed to compare events with very different laser energies (high flux events would saturate the SP mode, low energy ones would provide too little statistics).

So, in 2018 a new kind of mask (see figure 3.14) was used, with 80% of the sensor covered by a 11 μm Ti layer, and the remaining fifth a thick absorber with four holes, covered with different filters.

This way, it was possible to get the spectrum-integrated signal for all events, and still be able to resolve the single photons for events in the right flux range.

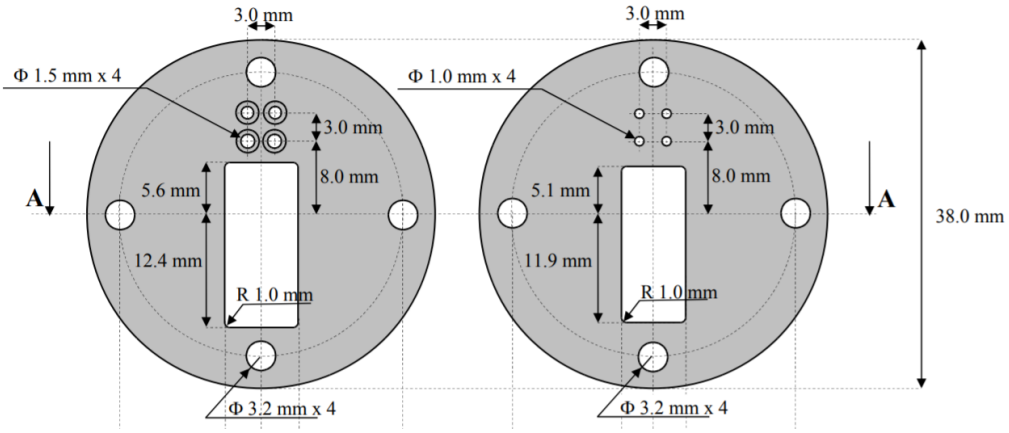

Figure 3.14: technical design for the filter mask. The mask is made of two discs, with thin filters between them. Aluminum filters are used for the four holes, while the wider hole is covered in titanium and used in Single Photon mode.

The camera was used in two different ways (in separate sessions at first, at the same time in later ones): In Single Photon mode and in integrating mode.

Data from the CCD camera are integrated over ten μs - a much longer time than the lifetime of the plasma - and thus yields no information about the time evolution of the plasma.

TOF collectors

Time-of-flight measurements allow to measure the velocity distribution of ions escaped from the plasma. For this measurement, unterminated LEMO connectors at negative voltage placed at different distanced from the interaction point have been used as ion collectors.

In the first data taking sessions, signal was affected by strong oscillations due to the electrical pulse being reflected in the cables. To reduce this source of noise, the pull-up resistor and amplifier was placed into the chamber, as close to the collectors as possible.

During some data sessions, it was attempted to positively bias the cables, hoping to gather data from the electrons, but the electron pulse turned out to be too fast to follow its time evolution, so negative bias was used in most sessions.

At most times, two groups of three ion collectors were placed inside the chamber, one approximately 15 cm from the target (ToF near) and one approximately 30 cm (ToF far) - see figure 3.2. Both groups were almost co-linear with the laser beam, to maximize collection.

TOF data turned out to be subject to large fluctuation, and capacitive effect in the amplification system affected its responsivity, so it was of limited use for analysis. But since the TOF signal could be immediately seen by oscilloscope (without the elaboration software required for the CCD and ICCD), it was very useful to have immediate feedback after a shot. Since shorter TOF time-to-peak was a sign of good focusing, it helped, together with X-ray data, to find the best focus position.

3.3 The 532 nm laser setup at l'Aquila

3.3.1 Laser system

The system is based on a Q-switched solid state Nd-YAG laser with 1064 nm wavelength, pulsed at 6 ns with nominal maximum energy of about 8 J. The maximum pulse rate is one pulse per minute. The 1064 nm output wavelength is then converted to 532 nm by placing a nonlinear medium on the beam, which is used as a 2nd order harmonic generator. In this case the frequency doubling is carried out by a KDP (potassium dihydrogen phosphate, KH2PO4) single crystal, which is a birefringent medium. The final 532 nm beam can have a pulse energy up to about 2 J. The output beam line has a diameter of 20 mm. The beam polarisation can be controlled by inserting a polarization rotator and each pulse energy can be measured by an energy monitor made of a beam splitter and a pyroelectric gauge (by Thorlab, model ES245C), as those installed at LNS. A picture of the beam line with a view of the chamber is shown in fig. 3.15.

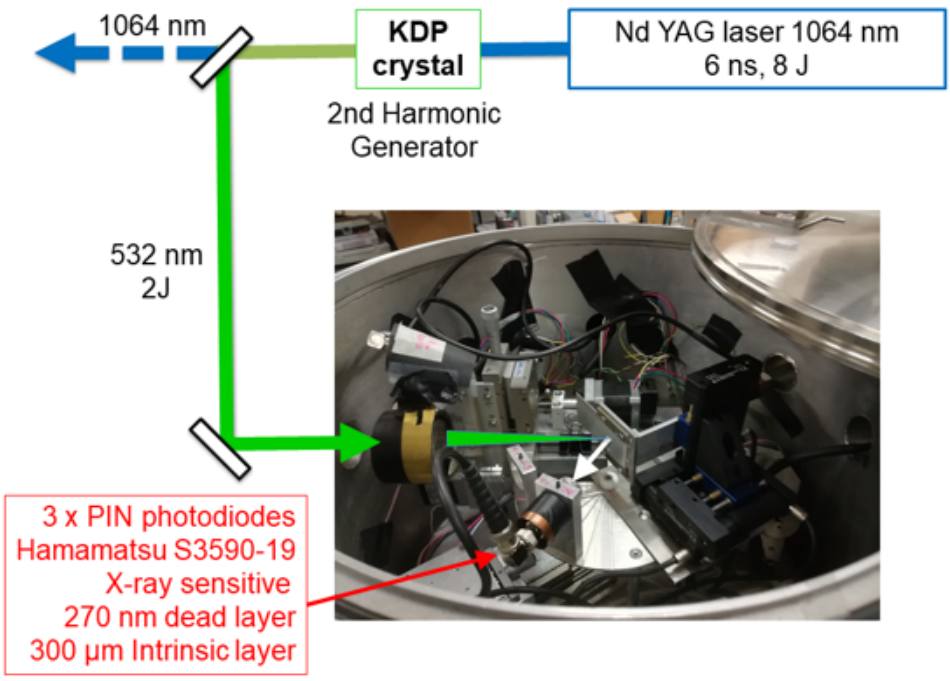

Figure 3.15: Schematic representation of the setup used for the irradiation at L'Aquila.

3.3.2 Interaction chamber

The interaction chamber is a cylinder of internal diameter 400 mm which can reach a vacuum of about 10-4 mbar. The chamber contains a sample holder which is mounted on a motorized translation stage that moves the target along the directions X-Y-Z, with a step resolution of 1 micron. The sample holder has a fourth degree of freedom since it can be rotated along the axis of the chamber so that the angle of the beam with respect to the normal to the target surface can be varied between 15 and 60 degrees. By placing a plano-convex lens with focal length 132 mm on the beam line, inside the chamber, the beam can be focussed on the target in a spot with diameter of about 200 μm, as in the LNS setup. The chamber houses also 4 silicon PIN photodiodes to detect X-rays, as described in the next section. An internal view of the chamber is shown in fig. 3.16

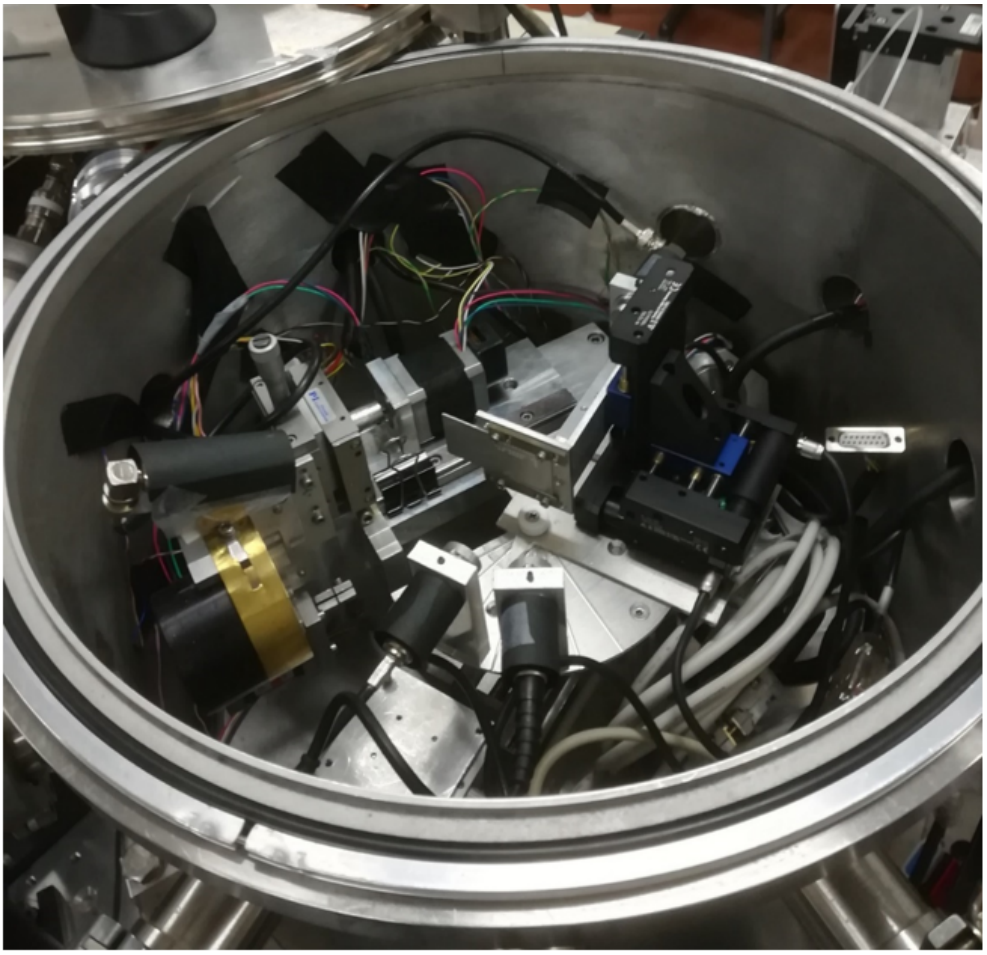

Figure 3.16: Interaction chamber at L'Aquila, seen from the top.

3.3.3 X-ray detectors

In order to detect X-rays, 4 silicon PIN photodiodes sensitive to low energy X-rays can be placed around the target. Such devices are Hamamatsu type S3590-19, without the protective window. They have a thin (270 nm) SiO2 dead layer and a depletion layer of 300 /*mu*m that must be operated at high reverse voltage (-50 V). Detectors can be placed around the target at different angles with respect to the normal to the target surface: on a forward angle (0°, 15°, 30° or 60°), on a backward angle (-45°) or just behind the target (180°). To avoid saturation from visible light, each photodiode was obscured with a filter made of a metal foil. Foils of different metals and thickness (Ti 2μm, Al 3μm, Ni 1μm, Al 9 μm) have been used to select different X-ray energy bands. The signal produced on the PIN diodes is proportional to the total charge in the silicon detector and therefore to the incoming X flow. However, the produced signal also depends on the spectrum of the X flux, since the quantum efficiency of the detector depends on the energy of the photons. Up to 10 keV of energy, which therefore covers the whole X

spectrum under examination, the sensitive thickness of the detector (300 μm) is able to convert any photon into electron-hole pairs. However, the detection quantum efficiency is lacking for low energies ($<$ 1 keV), as a part of the photons is absorbed by the dead region of the detector, by the passivation layer (270 nm) of SiO2 which protects the entrance window [1]. The transmission spectrum beyond the dead layer of the detector, which indicatively coincides with the quantum efficiency, is shown in fig **??**.

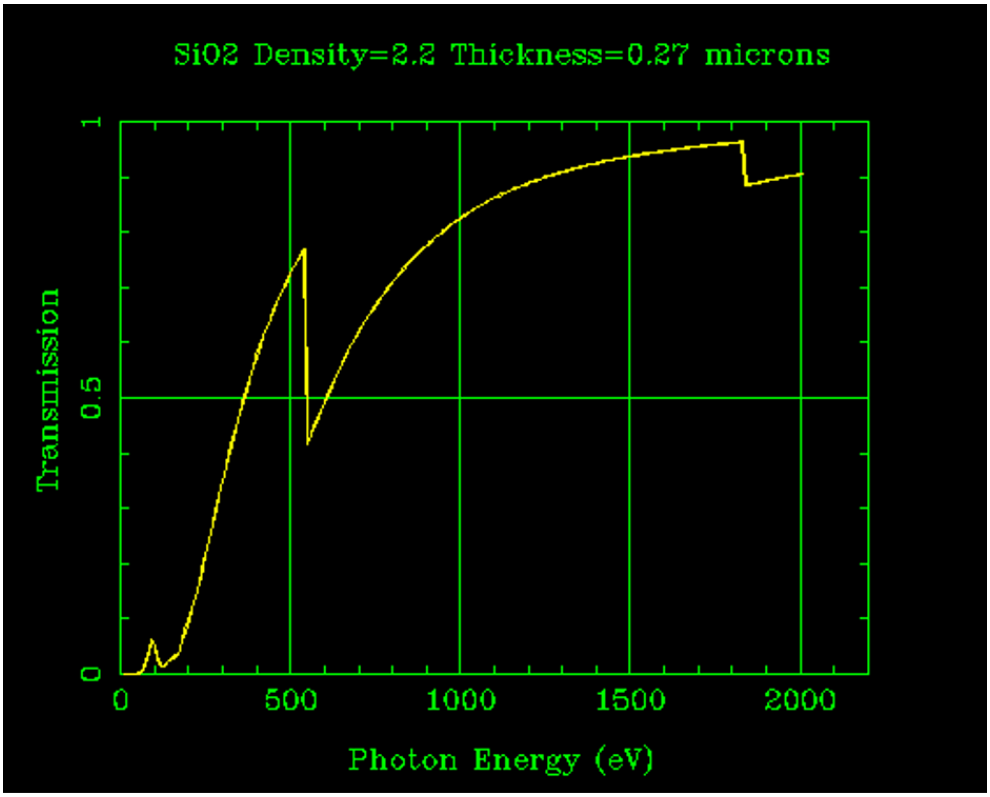

Figure 3.17: Transmission of X-rays through a 270 nm Si=2 layers. Computed from Center for X-ray Optics, Berkeley, website (http://www.cxro.lbl.gov/).

As can be seen, detection is lacking below 100 eV, and is greater than 50% for most values >300 eV. Absorption edges could have distortive effects on the spectrum.

TOF collectors

Time-of-flight measurements allow to measure the velocity distribution of ions escaped from the plasma. For this measurement, open LEMO cables at negative voltage placed at different distanced from the interaction point have been used as ion collectors.

In the first data taking sessions, signal was affected by strong oscillations due to the electrical pulse being reflected in the cables. To reduce this source of noise, the pull-up resistor and amplifier was placed into the chamber, as close to the collectors as possible. However,

During some data sessions, it was attempted to positively bias the cables, hoping to gather data from the electrons, but the electron pulse turned out to be too fast to follow its time development, so negative bias was used in most sessions.

At most times, two groups of three ion collectors were placed inside the chamber, one approximately 15 cm from the target (ToF near) and one approximately 30 cm (ToF far) - see figure 3.2. Both groups were almost co-linear with the laser beam, to maximize collection.

TOF data turned out to be subject to large fluctuation, and capacitive effect in the amplification system affected its responsivity, so it was of limited use for analysis. But since the TOF signal could be immediately seen by oscilloscope (without the elaboration software required for the CCD and ICCD), it was very useful to have immediate feedback after a shot. Since shorter TOF time-to-peak was a sign of good focusing, it helped, together with X-ray data, to find the best focus position.

3.4 Craters' analysis in Bologna

After laser irradiation, targets were sent (or brought) back to the INFN lab of the Physics and Astronomy Department of the University of Bologna, where the morphology and composition of craters has been studied. Part of this thesis work consisted in systematically collecting and analyzing crater data with the optical microscope, further analyzing structures of interest with a SEM.

The instruments employed for imaging are:

Optical microscope: A Huvitz HDS-5800 optical microscope has been used to make 3D pictures of craters and other features on the targets. It offers a range of magnification between 240x and 5800x, and it allows target movement with 2 μm precision in the x-y plane (parallel to target surface) and 100 nm precision in the z axis (normal to surface).

The microscope has very useful image manipulation capabilities: most important was the ability to quickly take several (dozens or hundreds) of images at different Z position, determine the focal plane from each, and generate a composite 3D-model of a surface. See figure 3.18 for examples of the generated models.

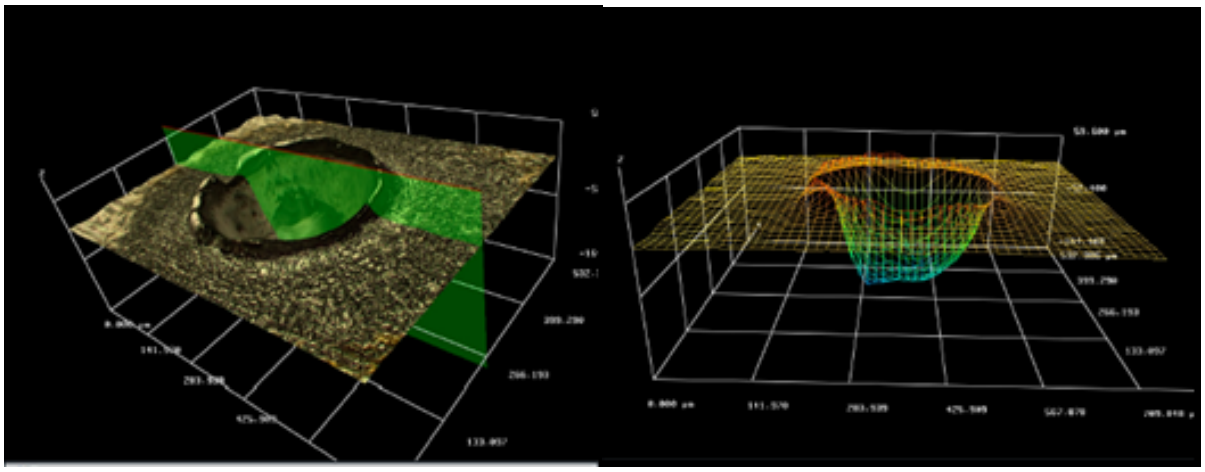

(a) **(b)**

Figure 3.18: 3D model in color view (left) and mesh view (right) generated by the optical microscope. This kind of models allow geometrical measurement with μm precision

The capability to easily build 3D models of laser craters and measure their geometrical parameter (such as ablated volume and depth) was hugely useful for this work, since it allowed to observe qualitatively and compare quantitatively the craters formed on different targets. Along with X-ray measurement, images from the optical microscope were so far the most useful to discriminate the properties of different targets.

Resolution of 3D models created by the microscope is limited by optical considerations, capabilities of the model-building software and artifacts. These contributions will be discussed more in depth in the next chapter, but as a first consideration, these models were found to be accurate within few μm when comparison with other measurements was possible.

No optical microscope could resolve single nanowires (those used for this study were all below 100 nm in diameter), so images and models taken with this microscope are useful down to the micro level, but SEM observation was required to directly observe the nanoscale effects of irradiation.

The microscope software allowed for collection and simple statistical analysis of geometrical data, and was extensively used for this thesis work.

SEM A Philips 515 Scanning Electron Microscope, located at the INFN microscopy laboratory in Bologna, was also used to observe the targets. It can reach 80 000 magnification for ideal samples, ie conductive, planar samples. Since the alumina layer is non conductive, for most of our samples the maximum magnification was 10 000.

This electron microscope has two operating modes (shown in fig 3.19)

- **Backscattered electrons imaging** this mode is used for most imaging purposes, since it yields high resolution images up to tens of thousands of magnifications.
- **Microanalysis** this mode yields no image, but analyses the X-rays emissions of the target in response to the electron flux. Since electrons can reach a 25 keV energy, K and L lines emission is possible, thus allowing the discrimination of elements in the target. This mode was very useful to distinguish the aluminum substrate from the NWs.

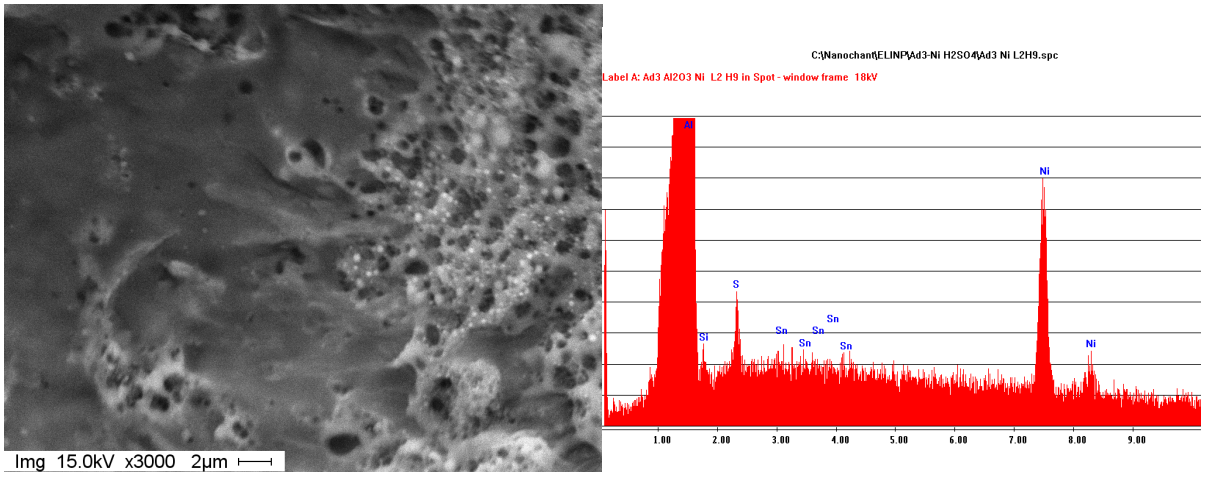

(a) backscattered electrons **(b)** microanalysis

Figure 3.19: Comparison of SEM operating modes. Left: SEM backscattered electrons image of the bottom of a crater. Nanoscale features (the light coloured "bubbles" on the right are likely to be partly molten NWs) can be clearly resolved. This is very valuable to check the quality of targets, and to understand the effects of irradiation on the nanoscale. Right: Microanalysis measurement from the same region. X-rays frequency peaks are used to identify elements. As can be expected, aluminum and nickel are the most prominent peaks, followed by sulphur (leftover from sulphuric acid anodization)

SEM measurements have been crucial for several steps of this work:

- **Parameter control of targets:** While alumina thickness and NWs height can be estimated from anodization and electrodeposition time, electron microscopy allows to directly image the nanostructures and measure their geometrical parameters. Since the targets need to be broken to see the NWs channels, this analysis was performed on the control targets instead of the actual targets.

  NWs of greater diameter (produced by oxalic acid anodization) could directly be observed within the channels, while those of smaller diameter (produced by sulphuric acid anodization) were too small, and were measured performing microanalysis at various heights of the alumina layer to test the presence of the NW metal.

- **Qualitative observation of craters:** comparison between optical and SEM images has been particularly useful, since SEM images allow to understand what kind of nanostructural modifications cause a given colour or texture.

Chapter 4

Data analysis

4.1 Sample types

While it would have been ideal to test every kind of target for every variable of interest (laser pulse power, polarization etc) and with every available detector, this has not always been possible. The main reasons for this are the fact that laser irradiation is destructive and sample production and irradiation are lengthy processes. Moreover, some setup conditions were not available for all samples. While measurements could be combined sometimes - for example, later in the experiment a filter was used for the CCD camera that allowed integrated and single photon mode at the same time - some detector setups were mutually exclusive, due to limited space in the interaction chamber or different filters required. Therefore, this chapter will be organized by sets of analysis which were performed with a given detector on a given set of samples. The relevant samples will be described in each section, but it's useful to understand which categories of samples were produced and used during the experiment. At the time of this writing, most analysis has been carried on 1064 nm data. Only preliminary results are available for 532 nm irradiation. The sample types can be divided into three categories:

- Nanostructured targets: Aluminum targets with nanowires of heavier metals were our main focus. Nanowires were produced with different geometrical parameters and elemental composition, as previously exposed. It should be noted that in some targets, the alumina matrix around the nanowires was left intact, while in others it was partially removed via chemical via chemical etching, in order to obtain "freestanding" nanowires, i.e. nanowires not embedded in the alumina matrix but attached to the aluminum substrate.

- Bulk targets: commercially available high-purity (>99.5%) bulk bulk metal targets (Al, Co, Ni, Ag and Fe) were used as reference samples, to compare against the

nanostructured ones. Which bulk target was the most appropriate reference sample for each nanostructured target is not obvious, to decide, since nanostructured targets are elemental mixtures. After the first data acquisitions, it was decided to use control samples matching the NWs metal, since the resulting plasma had closer parameters.

- Multilayer targets: this was a special set of targets produced to have mixed-element targets to be used as comparison samples, with quantities of atomic species equivalent (in mass) to the nanostructured samples, but without a nanostructured surface exposed to radiation. They were made of an empty alumina matrix on Al bulk, covered by a thin layer of Co (thickness varying for different samples, but in the μm range). Samples of different layer thickness were used to investigate how deep inside the target plasma formation occurred.

4.2 Morphological analysis of craters

Most of the morphological analysis of craters was conducted with the optical microscope (described in section 3.4), thanks to its capability to create 3D models of the craters and perform geometrical measurements. The aim of this work is to use the collected data to find which materials are more suitable to produce a hot and dense plasma.

However, the relationship between crater morphology and plasma parameters is not immediate, so it is not trivial to decide which features are indicative of a "good" plasma and which are not. Since the advantage of nanostructured materials compared to bulk aluminum lies in the volumetric heating of matter, it was decided to simply measure depth and volume of the craters. Later in this section, it will be explained how these quantities were measured, discussing the limitations in the chosen approach and the calculation of uncertainty.

One more choice to be made in the process of data collection was deciding which craters to include in the analysis. Due to laser focusing and other setup issues, some craters were irregular or very shallow. The criteria for crater acceptance or rejection will also be discussed in this section.

Finally, at the end of this section the morphological data (aggregated by target) will be presented.

4.2.1 Craters shape

Most observed craters have a sharp circular shape, with diameters ranging between 150 and 180 μm.

A crater's depth (measured at the deepest point) is, in most cases, greater than its radius but a little smaller than its diameter - the exception being Al-Bulk, which has greater radius than depth. The crater bottom is hemispherical in general shape, but often displays a structure called "channel", (see figure 4.1) a straight narrow indentation, resembling a knife cut, which begins at the centre of the crater and points downward, toward the same direction as the parallel component of the incoming laser beam.

This structure is definitely related to the inclination of the incoming laser beam, but surprisingly it is usually much more narrow (few tens of μm) than the spot size of the beam, so it seems unlikely to be a direct consequence of the spatial distribution of laser intensity. While its exact origin is unsure, optical observation and SEM imaging led to speculate that it originates from a rapid cooling of convection patterns at the crater bottom.

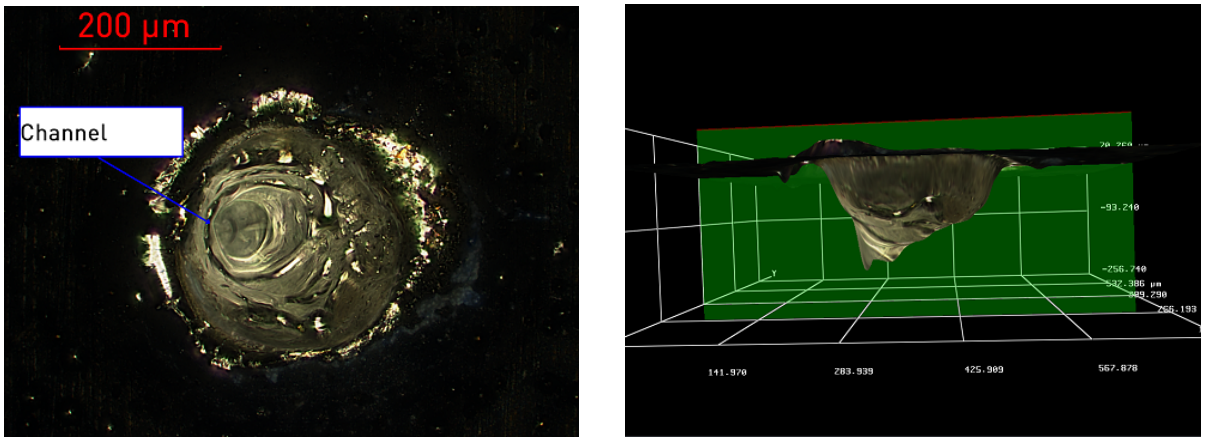

Figure 4.1: The channel structure, common in craters of all targets, seen from top (left) and side (right). As can be seen, the channel is a strongly asymmetric deep indentation in a mostly hemispheric crater. In this image, the laser beam arrived from the right.

Considering the surface outside the craters, different targets show different features - with different NWs material seeming to be a key factor.

Features observed next to crater's rim, for different targets:

- **Bulk-aluminum** shows a slight (less than 5 μm) swelling around the crater, likely due to thermal modifications during irradiation [5]. Outside the crater, there is often sign of surface melting (see figure 4.2).

- **Targets with nickel NWs** often show "peeled off" alumina around the crater (see fig 4.2), revealing intact aluminum. As can be seen in figure 4.2, the oxide layer breaks off along geometric lines. This is probably due to rapid thermal expansion of the material below, which causes rupturing of the alumina layer.

- **Targets with iron NWs** show a different feature: around the crater, alumina undergoes a radical modification, becoming white and foam-like in appearance (see fig 4.2c). They are also the craters with smaller radius.

- **Targets with cobalt NWs** usually show no evident modification of alumina outside the crater (see fig 4.2c), but differently from all other targets, some of them (approximately 25%) show a crater ridge above the alumina surface. This, along with the presence of peculiar "debris projections" and "pits", which will be described later, seems to imply that molten matter movement is more important in Co targets than in other kinds.

- **Targets with freestanding nanowires** (obtained in DC targets, after alumina removal) form craters of comparatively small diameter, but depth comparable to those in confined NWs targets. Their edges are difficult to observe with an optical microscope, since there is not as great a reflectivity difference as in confined targets (see fig 4.2b). They are much easier to distinguish in SEM images: matter inside craters is visibly molten, and a peculiar pattern of ball-like structures surrounds the crater. Lack of conduction through alumina is thought to limit the lateral expansion of craters.

Surface modifications: the surface of irradiated targets undergoes several modifications after laser irradiation. While some can be seen with an optical microscope, comparison with SEM often offers useful insight.

Target surface modifications often affect a wide area - even a millimeter long. Therefore, adjacent shots must be spaced at least 2 mm to avoid ablation on material already modified.

The different kind of surface modifications found in irradiated targets are:

- **Foam-like material:** at the bottom of craters, usually "clean" bulk aluminum metal can be found. But at the edges, and sometimes at the bottom, residual matter from alumina, nanowires and aluminum mix in a foam-like material (see fig 4.3), with collapsed and partly molten NWs forming "bubbles" up to 200 nm in size which appear bright at SEM analysis.

- **Shredded alumina:** while alumina near the crater (tens of μm from the rim) is much less reflective than the aluminum in the crater and looks intact at first sight, it can be noted it gets brown hue. SEM imaging reveals that alumina in this region is heavily damaged (see fig 4.3), with the ordered channel structure completely

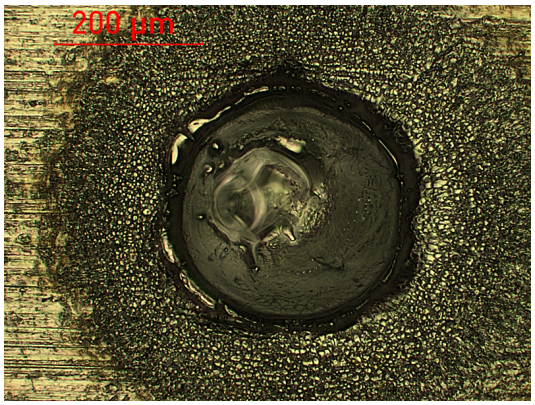

(a) Typical crater in bulk-aluminum. The shape is very regular, and modification of the surface, probably due to melting, can be seen hundreds of μm from the crater's edge.

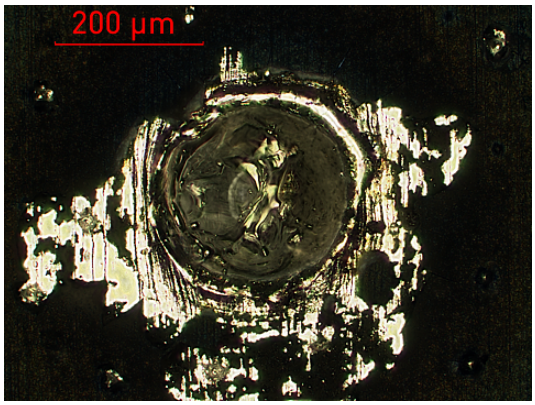

(b) Typical crater in target with Ni NWs. As can be seen, the alumina layer is "peeled off" around the crater, revealing intact aluminum below (lamination lines, vertical in this image, can be noted). The surface appears very dark due to the contrast with highly reflective aluminum.

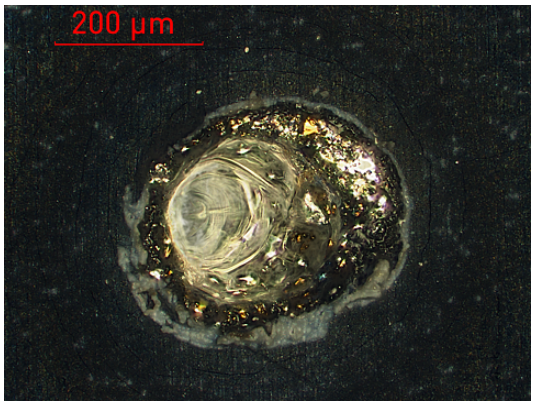

(c) Typical crater in target with Fe NWs. The most striking feature of these craters is the formation of a white "crust", foam-like in appearance, between the crater and the comparatively intact alumina around it.

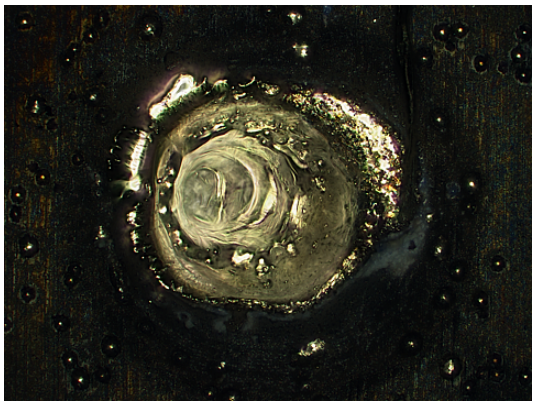

(d) Typical crater in target with cobalt NWs. Craters in this target are comparatively small in radius, and surrounded by a small area of molten surface

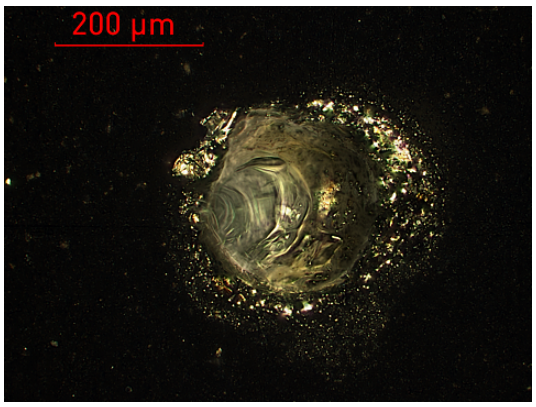

(e) Typical crater in target with freestanding nickel NWs. Craters in this target are comparatively small in radius, and surrounded by a small area of molten surface

Figure 4.2: Comparison between craters in targets of different kinds

lost. Measuring the extent of shredded alumina could be useful in future analysis to understand how far heat propagates from the crater.

- **Coloured alumina:** farther from the crater (hundreds of μm to millimeters), the most evident modification is a change in surface colour, which gains a yellow hue (near to the crater) and then a blue one (farther from the crater). This coloured halo can be seen quite clearly (see fig 4.4) when using a point light source, but disappear completely with diffuse illumination. This led to hypothesize that colours are due to interference effects - possibly caused by partial melting of NWs inside the pores.

  A different hypothesis is that colours are due to thermal combination of alumina with residual gas in the chamber, i.e. mainly nitrogen and oxygen. In future, SEM microanalysis could be used to test these hypotheses.

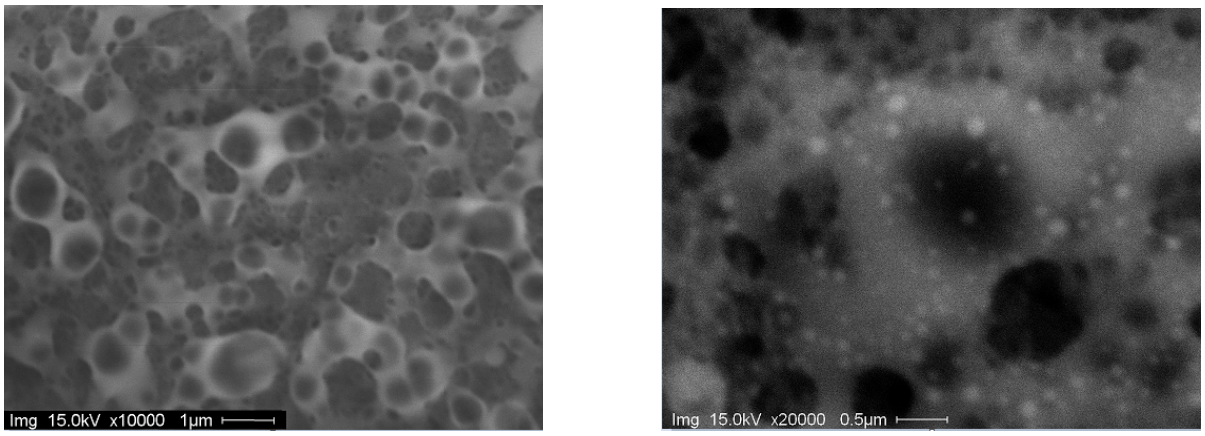

(a) **(b)**

Figure 4.3: left: shredded alumina few tens of μm from a crater in a preliminary target. The ordered structured is completely lost. NWs are no longer visible, likely due to the swelling of the alumina surface during the shredding process. This damage is likely caused by shockwave propagation in the target. Right: foam-like material at the bottom of an out of focus crater. Residual of NWs are still visible as bright bubbles in the alumina.

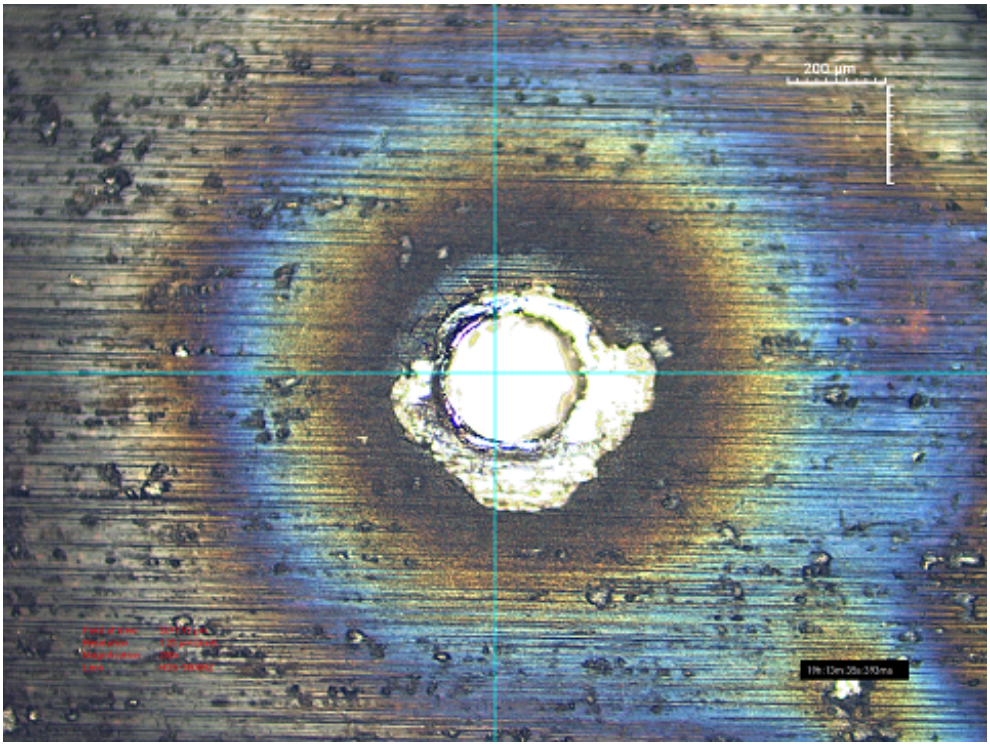

Figure 4.4: Surface modifications of alumina, seen with point like white light source (bright field). Near the peeled off zone, alumina is brownish and rough in appearance: this is the "shredded alumina" region, where the ordered structure is lost. Farther from the crater, alumina is mostly intact (lamination lines are still visible), but acquires colored halos. Different targets show slightly different color patterns, but shorter wavelength colors are always on the outside.

Some other peculiar features were found in specific targets. Although no statistical analysis was performed on them, their presence (or absence in different targets) can shed light on the physical processes which occur during irradiation.

Debris projection: One interesting feature was found in several craters, most of them in the target with cobalt nanowires: a rough circle of fused metal, above the surface level, tangent to the crater (see figure 4.5). In most cases, these debris are tangent to the crater along the direction of the component of the laser beam parallel to the surface, but sometimes the debris forms towards the laser, sometimes opposite it.

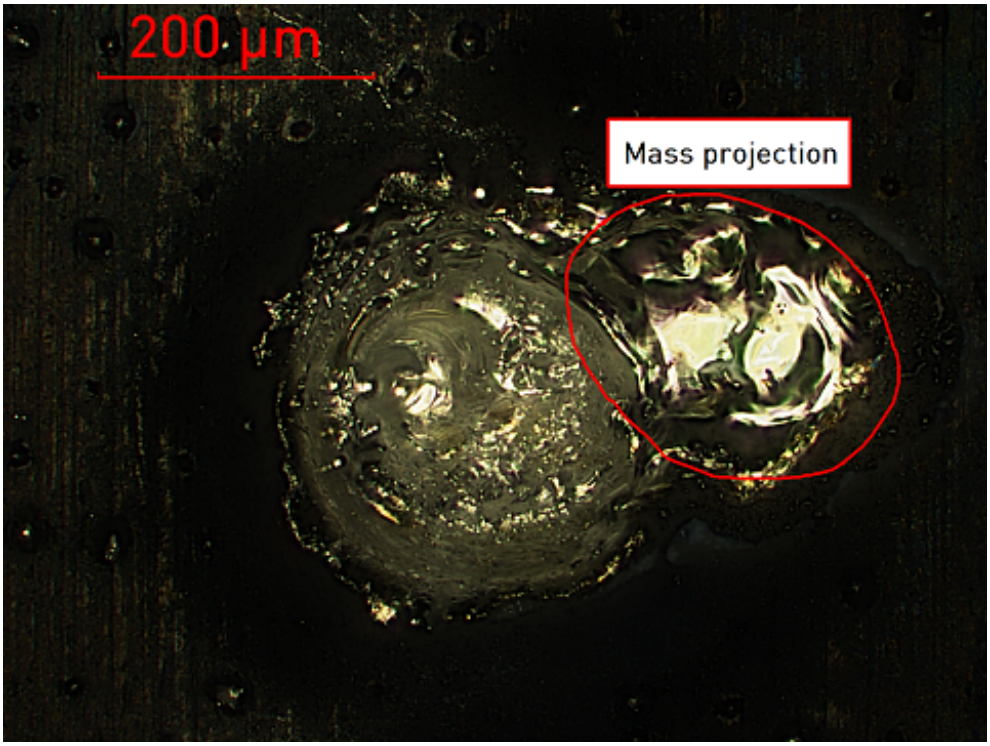

Figure 4.5: Debris (mass) projection in target Co-Thin. It can be seen as a smooth and highly reflective area near the main crater. In this case, the molten material is in the direction of the incoming laser beam (right).

Likely, this debris is formed by matter flow at liquid phase. Together with other features, this might indicate a more important liquid phase in targets with Co NWs compared to other materials.

Pits: Several targets show circular "pits", a few μm wide, pock marking the alumina surface around the crater (see fig 4.6). Most of them are too small to reliably measure their depth with the optical microscope due to diffraction, but the widest ones seem to be as deep as the alumina layer. SEM analysis shows the bottom of the pits is conductive, therefore it seems these pits reach the aluminum under the oxide.

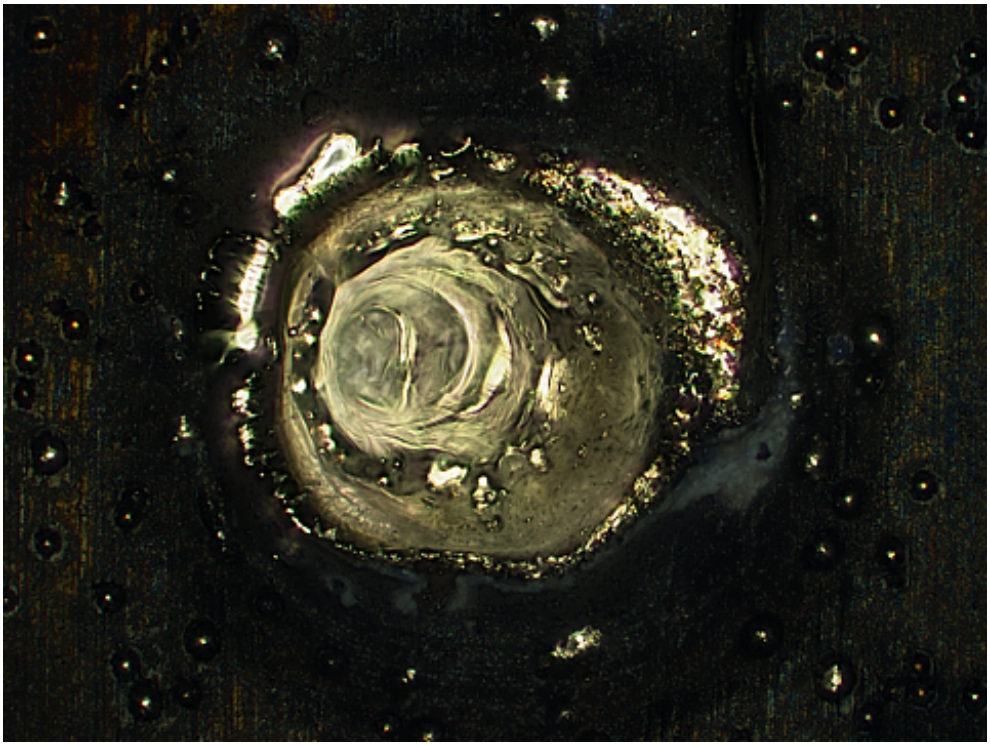

Figure 4.6: Pits in target with cobalt NWs - the small circular marks which surround the craters. The high reflectivity at the centre of pits is likely from aluminum substrate, meaning the whole alumina layer has been removed. Pits are likely due to laser light reflected by the plasma.

At least some pits can be found in all targets except the bulk-aluminum one. They have a peculiar spatial distribution: they are absent near craters, become more frequent near a specific radius, and then become less frequent again. This peculiarity led to think they are due to reflected laser light, possibly scattered by the expanding plasma plume. While they have not been analysed in detail yet, should the plasma scatter hypothesis be confirmed pits density could provide useful data on plasma evolution

4.2.2 Morphological measurements

In this subsection, morphological data systematically collected on the craters will be presented, explaining the criteria used to choose which crater were included in the analysis, and how measurements have been performed.

Measurement process: the optical microscope used for this work allows several kind of measurements on the 3D models it creates, including linear, superficial and volumetric quantities. It is not trivial to decide which geometrical parameters are indicative of more energy absorption. Also, due to the structure of craters, some measurements could be

reliably performed with low uncertainty, while others required arbitrary decisions or led to high uncertainties.

After comparison of several kinds of measurement strategies, only two parameters were included in the final analysis: crater depth and volume. They have been measured in the following way:

- **depth**: first, a line is chosen along which the crater's depth profile will be measured. It was decided to choose a line parallel to the laser beam direction and passing through the point of maximum depth. Since surface outside the crater is quite flat (within two μm) for all considered targets, depth is simply calculated as the height difference between a point well outside the crater - to exclude local swelling and other near-crater features - and the deepest point of the crater.

- **Volume**: to measure volume, it is necessary to define a 2D measurement region, and a reference level. Empty volume will be calculated below the reference level, and only in the selected region.

  Reference level is taken at the surface. At first, the 2D region was defined as a closed geometric line following the rim of the crater, but it was found that simply selecting a circle a few tens of μm wider than the crater gave results within 1% of the point-by-point defined area, so a circle was used for simplicity and to avoid ambiguities in the exact criteria for crater edge definition.

  It was also decided that empty volume due to peeled-off alumina should be included in volume the measurement.

Two more parameters were initially considered viable for analysis: crater diameter and crater curvature radius. Crater diameter was excluded due to ambiguities: features present in some targets (raised crater rim, peeled off alumina) made difficult to choose criteria for measurements, incurring the risk of misleading systematic differences between targets. Curvature radius was found to have large uncertainty and was difficult to measure in targets exhibiting channel structure.

Craters choice: despite appropriate tuning of the experimental setup, it was soon evident that not all craters could be part of the analysis. For example, the laser was subject to occasional glitches, focusing problems occurred during the data taking phase, and some craters were clearly different from the others.

So, a policy had to be set for the choice of which craters should be included in the analysis, in order to avoid including data contaminated by setup problems.

So, the criteria for craters selection were:

4.2.3 Uncertainties and statistics

Measurement of craters' depth and volume found significantly different values within each target. To account for this differences and provide accurate mean and uncertainty values, two sources of fluctuations must be taken into account: actual differences in craters within a target, and uncertainties on depth or volume measurement.

In addition to this statistical fluctuations, possible systematic errors will be discussed, and the steps taken to minimize them described.

Setup uncertainties

During the data taking, not all experimental variables could be perfectly controlled. While a huge number of experimental parameters could influence the resulting crater for each shot, the most important sources of uncertainty are thought to be the following:

- **Laser energy:** in the current setup, there is no shot-by-shot control of laser intensity. Since energy calibration is performed measuring the total energy delivered by a high number of shots, the variance of energy between shots is currently unknown, and could be an important contribution to morphological fluctuations between different events.

- **Target regularity:** even if the laser always delivered energy with exactly the same spatial and temporal distribution, the target surface could have local inhomogeneities. Pores length should be very regular and NWs length have a narrow distribution, with local difference between single NWs but not between different regions of the target, but some local fluctuations exist. Since a high number of NWs is included in the laser spot (order of 10^6), fluctuations in the number and shape of NWs should be small. Still, together with other target irregularities (metal grain, impurities, scratches and other minor damages, surface modifications due to previous shots) they probably contribute to craters' random fluctuations.

- **Intrinsic variability of the process:** even with optimal control over laser and target conditions, perfectly identical craters would not be expected. Plasma evolution involves many chaotic processes, and very small setup differences (or even intrinsic stochasticity of laser-matter interactions) could easily be amplified to different results.

Systematic measurement errors:

Uncertainty on depth and volume measurement for each craters comes from different sources, some of which are quite difficult to estimate. Those considered most important

are:

- **Resolution:** 3D models were built by software stitching of images captured at 1 μm step, so 1 μm is the effective vertical resolution of these measurement. For depth measurements, this means a $\sqrt{2}$ μm total uncertainty. As craters' depth ranges between 160 and 210 μm for all targets, resolution contribution to depth uncertainty is below one per cent. As for volume, resolution uncertainty has been considered to be vertical resolution times twice the measured region surface as conservative estimate.

- **Surface definition:** Both depth and volume measurements require identification of a surface level outside the crater to be used as reference. While most targets' surfaces were very regular, sometimes swelling near the crater or surface irregularities made the definition of "surface level" outside the crater subject to some arbitrariety, especially for not perfectly planar craters. The extent of this uncertainty was estimated by measuring the difference from the highest and lowest point of the surface outside the crater, and considering that to be twice the standard deviation.

- **Deepest point identification:** The channel structure at the bottom of craters contributes very little to volume, but is important for depth measurement. Differences in illumination and geometrical orientation of the target lead to slightly different depth estimation by the 3D-building algorithm, due to the difficulty of focusing the channel structure. By repeatedly scanning the same crater with different illumination and positioning, random fluctuations due to this effect have been estimated to be $\approx 2\mu$m.

- **3D model building software**: Observation of surface scratches led to discover that the microscope's modelling algorithm does not work very well on thin grooves, and underestimates their depth. Since no other instrument was available to independently measure channel depth. This contributes a currently unknown systematic error to depth. To reduce it, target magnification and illumination have been chosen in such a way to produce as clear images as possible of the channel structure. In future, comparison with independent measurements could allow to evaluate this error.

Uncertainty calculation from standard deviation of mean Estimated systematic measurement uncertainties for typical craters are reported in table 4.1. As can be seen, the quadratic sum of systematic uncertainties is considerably smaller than the observed

variance. This likely means actual crater-by-crater fluctuation of craters' parameters is the main contribution to variance.

While systematic errors on measurements might be present, as long as they affect every target in the same way, they are of little interest for this study, which is comparative in nature.

radius calculation Direct measurement of craters' radius proved very challenging, due to the lack of a well-defined rim, and irregular geometrical features of some crater. Finally, a simple approximation was used, based on the observation of the craters' profiles: craters were assumed to be shaped like a cylinder plus a half-sphere of equal radius. In this hypothesis, radius can be calculated from depth and volume. The results were found to be reasonable consistent with observations, and thus are included in the data, even if it should be noted that they add no degree of freedom to volume and depth.

Sources of systematic uncertainties on depth and volume		
Source	σ depth (μm)	σ volume $(\mu m)^3 \cdot 10^5$
Vertical resolution	$\leq \sqrt{2}$	≤ 0.2
Surface identification	≤ 2	≤ 0.1
Deepest point identification	≤ 2	-
Total	3.2	0.22

Table 4.1: List of sources of systematic uncertainty on morphological data. The listed values are to be considered maximum values, valid for all targets.

4.2.4 Morphological data

In the following table, depth and volume data from all the targets included in the morphological analysis are listed. As previously explained, uncertainty is calculated as the standard deviation of the mean, while the systematic error is assumed to be the same for all targets and reported in table 4.2

Morphological data for each target				
Target	Number of craters	Depth (μm)	Volume ($\mu m^3/10^6$)	Calc. Radius (μm)
Al-Bulk	23	139 ± 3	3.67 ± 0.13	106
Ni-Thin	19	160 ± 3	3.99 ± 0.08	100
Co-Thin	29	184 ± 3	4.52 ± 0.05	97
Fe-Thin	31	171 ± 4	3.39 ± 0.09	87
Ni-Long	7	203 ± 10	5.32 ± 0.24	100
Ni-Short	23	180 ± 4	4.67 ± 0.05	101
Ni-DC	23	189 ± 4	4.20 ± 0.07	92
Ni-Free	8	172 ± 10	3.69 ± 0.24	91

Table 4.2: Average depth and volume of craters for each target, with calculated radius.

As can be noted, difference between targets in terms of morphological data is usually several times larger than uncertainty. This means that, while there is some overlap between depth and volume of craters in different targets, their mean values are significantly different.

It's interesting to notice that despite the low melting point of bulk aluminum (660 °C, compared to 2072 °C for alumina and >1400 °C for the metals involved), craters in aluminum are shallower and smaller in volume compared to those from nanostructured targets, with slightly larger radius.

This is probaly due to different propagation of heat and shockwaves in metal vs alumina. As evidenced by the previous figures, aluminum melts in smooth craters, while alumina plits and tears, causing more total volume to be removed with the same pulse energy. Nanowires free from alumina show an ablation volume closer to that of aluminum, but with substantially greater depth - this could be due to their directionality, which helps convey heat and shock along their axis compared to the lateral direction.

Overall, craters have similar radii, consistent with the calculated spot radius of 97 μm.

4.3 Visible spectrum analysis

Optical imaging is extremely useful since the ICCD camera described in section 3.2.4, with a minimum gating time of 2 ns, is fast enough to take snapshots of the expanding plasma. Since the plasma emits visible light, this allows to obtain information about the spatial evolution of the plasma plume over time, possibly highlighting differences between bulk and nanostructured targets.

While image gating is very fast, readout is not as fast, though, requiring almost a millisecond even at the fastest speed. Since plasma emission remains detectable for 200 ns at most, with most of the emission intensity in the first 50 ns, it wasn't possible to take repeated snapshots of the same event.

Therefore, to study plasma evolution, a series of laser pulses were taken on several events at different positions on the target, with the same beam conditions, but plasma images were recorded at different delays from the time of interaction. Assuming that most events, having the same initial conditions, led to similar plasma dynamics, this allowed to follow the evolution of the plasma plume from the moment of the laser shot to the last detectable signal.

Since plasma emission decreased with time, gradually longer exposure (5 and finally 10 ns) was used for shots with higher delay. In this way, more signal was collected, at the expense of less temporal (and spatial, as a consequence) resolution.

Since the detectors available to the group didn't allow a spectrographic analysis in the visible range, no information could be extracted about the spectral distribution - and thus the production process - of the collected signal. Literature leads to expect a visible emission dominated by recombination, but for this analysis, visible emission is used as a tool to study the geometrical evolution of the plasma plume over time, so the emission mechanism is of secondary interest.

4.3.1 Analysis software

Raw data collected through the ANDOR (the manufacturer of the ICCD) software consisted in a matrix of digital values, representing the counts for every pixel in the CCD sensor during exposure. While the software included some visualization and analysis tools, they weren't well suited to our specific task, so new software was developed to analyse the data and display them in a more intuitive manner.

While visual comparison of the time series from different events is instructive, approach was needed that allowed quantitative comparison of the plasma plume's geometry. In the end, it was decided to divide the image into geometrical sections, integrate the signal over each section, and use the resulting values as the starting point for our analysis.

After several attempt, it was decided to define regions relative to the interaction point. Since the plasma plume is roughly conical, the analysis regions (see figure 4.7) are shaped as circular sectors, with nine regions of different angles (0-30°,30-60° and 60-90° relative to target's normal) and different distances from the target's surface.

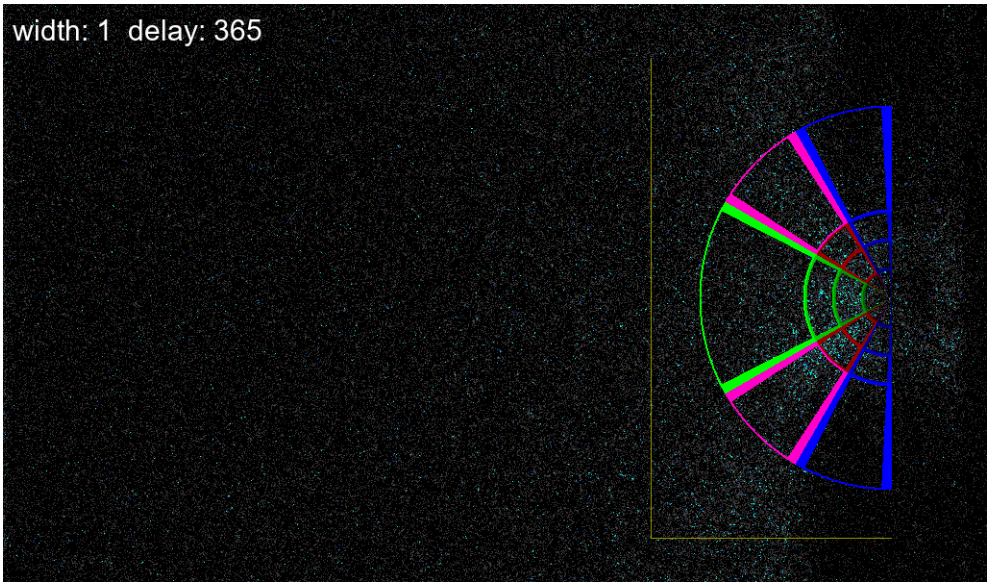

Figure 4.7: The grid used to compare geometrical evolution of events. Four radial regions and three angular regions (distinguished by color) have been considered

Locating the interaction point for every image turned out to be a problem, too. In the first nanoseconds after shooting, it's easy to find the interaction point since the emissive region is small and approximately circular. As the plasma evolves, though, it becomes less easy to identify.

At first, it was assumed that the coordinates determined at low delays could be valid for the whole sequence of events, too, but comparing several low-delay events for the same target soon made clear that the interaction point can move between events.

This was likely because, while the camera doesn't move, the target holder moves to present fresh parts of the target to be shot. In principle, this shouldn't change the interaction point's position, but it was later verified with the distance meter that its distance from the lens actually varies within a range of about 200 μm. When the majority of the time evolution measurements were made, in 2017, an older sample holder was used, which introduced an offset on the lens-target distance, and the laser distance meter wasn't yet available, so this offset must be corrected with information from the images themselves.

For the y coordinate of the interaction point, the y of the brightest point for each image was chosen, since the plume seems symmetrical relative to the laser's plane. The x

coordinate couldn't be determined this way, because as the plasma expanded, its brightest part shifted away from the target's surface, and thus didn't work as a fixed reference.

Finally, to measure the shift caused by the sample holder's movement, an unintended feature of the images was exploited - the plume's reflection on target's edge, as can be seen in figure 4.8. Since the target's edge obviously moves with the target itself, it was used to calculate the offset for the center's x coordinates.

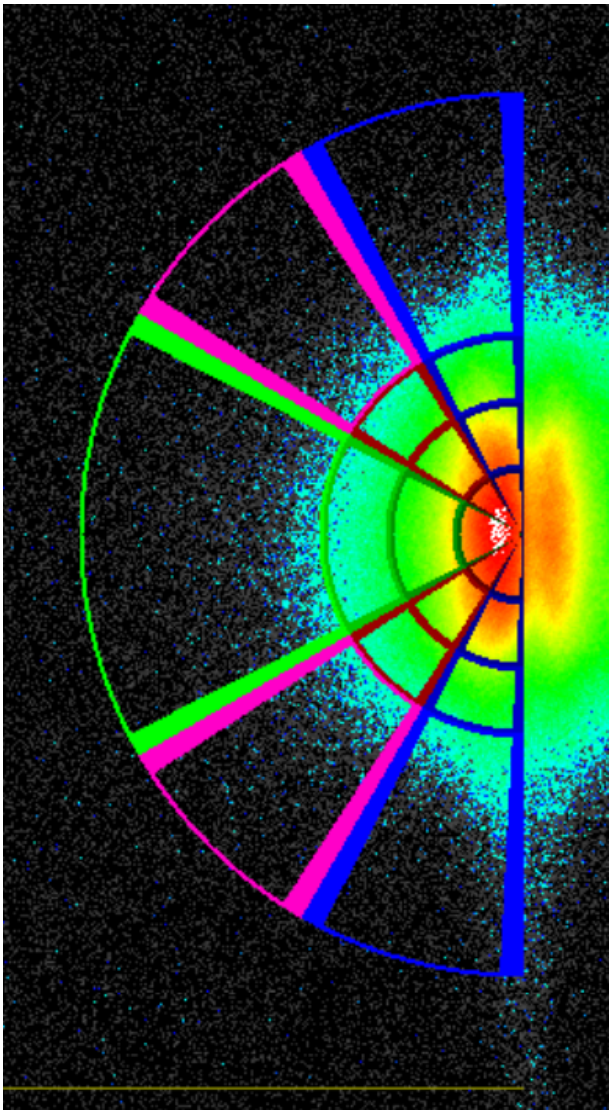

Figure 4.8: The target's edge, a useful reference to correct for small displacement of the target between shots, can be seen as a vertical line.

It was also noticed that the trigger used to set the ICCD delay and the laser's own trigger were not perfectly synchronized. This led to some uncertainty about the time measurement. By comparing images taken at low delay, though, it was found that the first signal can be seen at t= (16 $\pm$ 1) ns from the trigger. The 1 ns fluctuation could be due to the camera's internal clock or to the laser's trigger system. For clarity, times

shown in images and tables are corrected for this, with t=0 at 16 ns from the nominal trigger time.

Uncertainties There are several sources of uncertainty affecting this measurement.

The statistical uncertainty due to background is very low. Background level and uncertainty were assessed event by event, checking the signal in a region of the sensor above the target, where it was expected to find no signal (except for very high delay events). While the background is substantial, it has a very low standard deviation (2.6 counts per pixel, with typical signals >1000 counts per pixels). Therefore, it was simply removed pixel-by-pixel, and its fluctuation, averaged of a ROI, is $< 1\%$ of signal for typical events, so it has been deemed irrelevant.

A more troubling source of instrumental error is the overflow artifact (blooming) which can easily be seen in many images (see image 4.9).

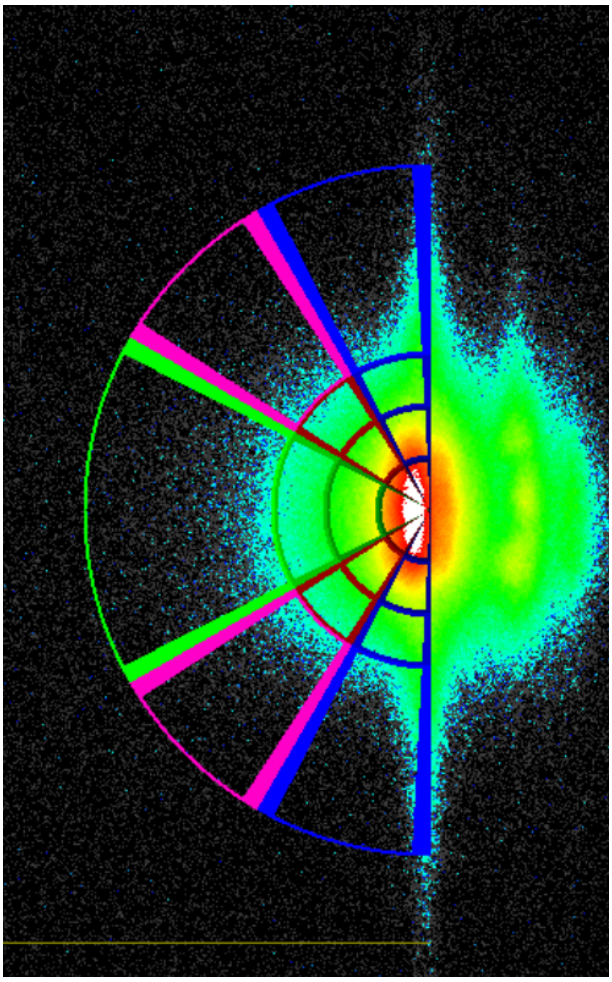

Figure 4.9: ICCD image with obvious overflow artifact along the vertical axis, known as blooming. Note the green color, indicating a low signal compared to the orange and red regions.

This is a systematic error due to the readout process of the CCD sensor, and can't

be easily removed, since the artifact can't be clearly separated from the signal.

However, pixels affected by the artifact, but outside the signal region, read less than 3% of the average value of signal in the same ROIs, since the artifact is present only when pixels are subject to high flux. Therefore, a conservative estimate could be made of their impact by adding a 3% uncertainty to the affected ROIs.

The largest source of uncertainty is the event-by-event fluctuation, due to stochastic processes in the plasma plume, fluctuation in the pulse intensity and small differences in beam focus. Ideally, this uncertainty would have been estimated by repeating the time evolution measurement a sufficient number of time. Given the practical constraints, though, only two couples of repeated measurements were available. Since the interest is mostly in the signal distribution, the percentage of signal in each ROI at matching delays for different series was considered, averaged, and taken as an estimate of event-by-event fluctuation.

4.3.2 Plasma evolution

A typical plasma evolution sequence can be seen in pictures 4.10. This image is taken from a sample with Ni NWs, but a roughly similar pattern is valid for all targets. Differences will be discussed later in this section.

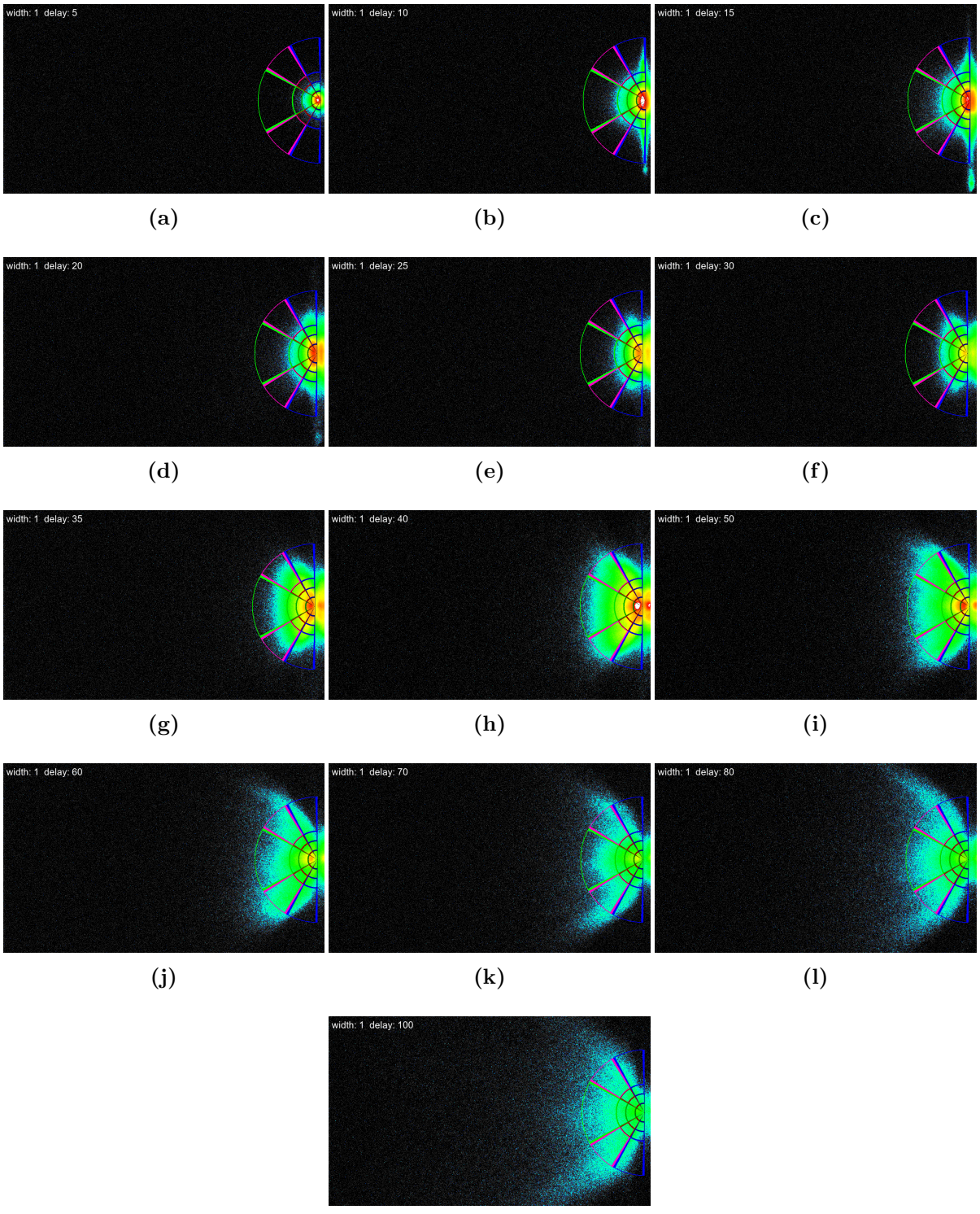

Figure 4.10: Time evolution series for bulk Al, with increasing delays up to 100 ns.

Note that while the image appears symmetric, the actual plume is on the left, while the signal on the right is its reflection on the sample's metal edge.

As can be seen, in the first nanoseconds after the shot, the plasma becomes brighter and expands outward. Peak emission intensity is reached after about 10 ns, which is consistent with the pulse duration of 6 ns. Surprisingly, the most intense region of emission doesn't expand equally in all directions, but spreads laterally (along the target's surface) before spreading outward. This might be due to laser interaction with the plasma, exerting a compressive force on the early plasma, or due to the fact that heat is spreading on the target's surface and generating new plasma.

Soon, the expansion becomes roughly conical, with an intensely emitting core and a less emissive halo.

From about t=30 ns, a further structure can be noticed: jets of hotter plasma at 0° and about 70° from the target's normal.

While the 0° jets are unsurprising - there's ample expectation from literature for an emission peak at 0°, the 20° ones are more surprising. This happens to some degree to both nanostructured and bulk targets. As the plasma evolves further, those angular emissions seem to "bend" forward, probably due to collisions with backscattered plasma.

It should be noted that it might not be due to real geometrical distribution of the plasma, but to greater recombination at the edges of the plasma cone.

Either way, they are a feature of the plasma plume which can be compared between different kinds of targets, and thus useful to investigate differences between nanostructured and bulk targets.

In the later phase of the evolution, the plasma thins and spreads, blurring the initial structures and fading beyond detectable levels after about 200 ns. Overall, the total signal (total counts in all the considered regions, normalized by exposure time) has a similar time dependence for all samples: a fast climb within the first 10 ns, then a slower exponential decay, as can be seen in figure 4.11, with substantial fluctuation probably due to event-by-event variation.

Name	Label	type	metal	NWs ø (nm)	NWs length (µm)
Al bulk	Al01	bulk	Al	\	\
Ni NWs	Ad7Ni	NWs	Ni	20	10
Co NWs	Ad9Co	NWs	Co	20	10
Fe NWs	Ad10Fe	NWs	Fe	20	10
Ni long NWs	Ad20Ni	NWs	Ni	20	20

Figure 4.11: Time-evolution of the visible emission intensity, normalized to the peak, for different samples

While the overall evolution is similar, as we'll see in the next section the geometrical structure of the plasma has some variations between samples.

4.3.3 Visible emission comparison

Time-evolution measurement required a set of measures under very similar conditions, and the ICCD camera wasn't always available to us, so the plasma time-evolution could be compared only for a subset of the samples at our disposal. In table 4.12 the most important samples used for this comparison are listed.

Name	Label	type	metal	NWs ø (nm)	NWs length (µm)
Al bulk	Al01	bulk	Al	\	\
Ni NWs	Ad3Ni	NWs	Ni	20	10
Co NWs	Ad7Co	NWs	Co	20	10
Fe NWs	Ad10Fe	NWs	Fe	20	10
Ni-long	Ad20Ni	NWs	Ni	20	20
Ni-short	Ad20Ni	NWs	Ni	20	10

Figure 4.12: Samples considered for the time evolution series. Several other samples were used, but data were deemed less reliable due to setup problem or limited statistics.

There are three similar nanostructured samples, with short, thin nanowires of different metals (Co, Fe and Ni). In addition, there are two nanostructured samples with very similar parameters except for the length of nanowires. Those samples are meant to be compared to each other, to assess the impact of NWs length on plasma evolution. As a control sample, a bulk aluminum target was chosen. Aluminum was selected, and not the metals constituting the nanowires, because the plasma is, by volume and by mass, mostly aluminum. For some samples (Fe and Co NWs) two time-evolution series were collected, while for the others (Ni NWs and bulk Al) too few shots were available, and only one time-evolution series was collected.

Plasma time-evolution comparison

Let's now consider the difference between distribution of signal for nanowires target compared to the bulk Al. In figure 4.13 and 4.14, time-evolution series can be seen for samples Co-NWs and Al-bulk respectively. Co-NWs is fairly representative of the three thin NWs samples, which time-evolutions are quite similar to each other.

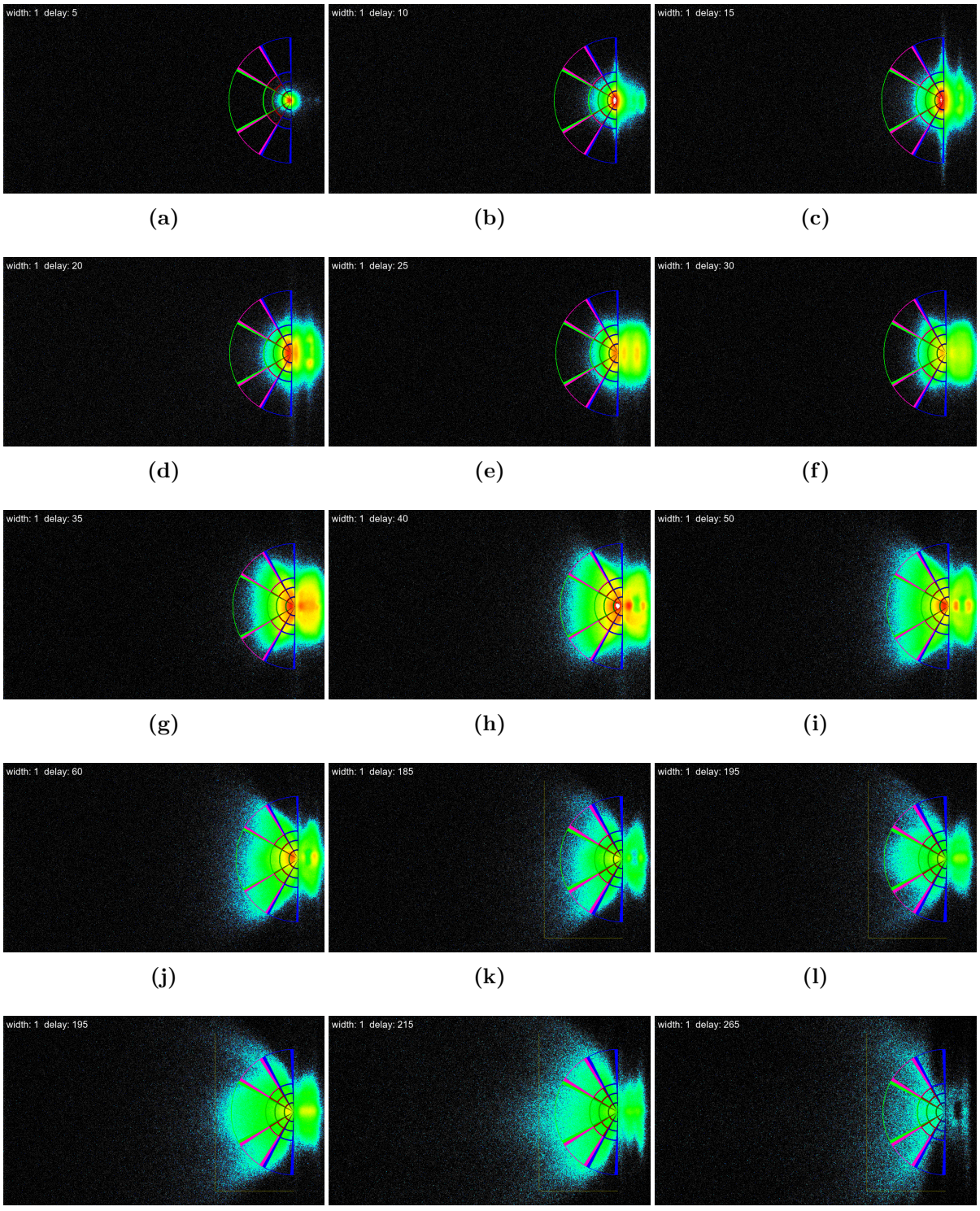

Figure 4.13: Time evolution series for target with Co NWs, with increasing delay up to 265 ns.

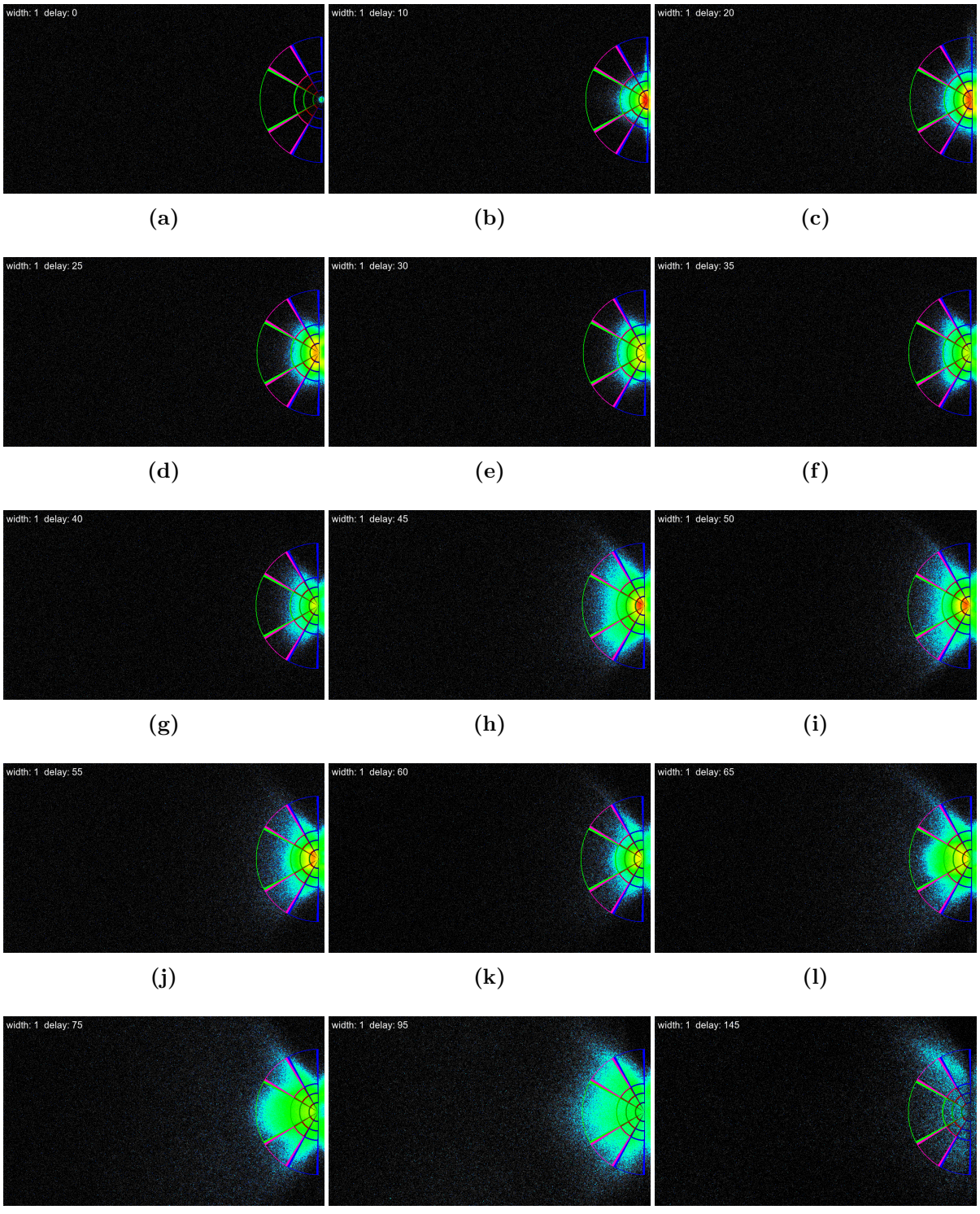

Figure 4.14: Time evolution series for bulk Al, with increasing delay up to 145 ns.

It can be easily noticed how the Al plasma has a stronger central emission, with weaker lateral jets. The opposite is true for plasma from NWs, which have strong lateral

jets.

Quantitatively, this can be supported by the previously discussed analysis of angular regions. In particular, the density of signal (counts per pixel) in the outer regions (60°-90° from the normal) can be compared to the middle and central ones. These results can be seen in figure 4.15.

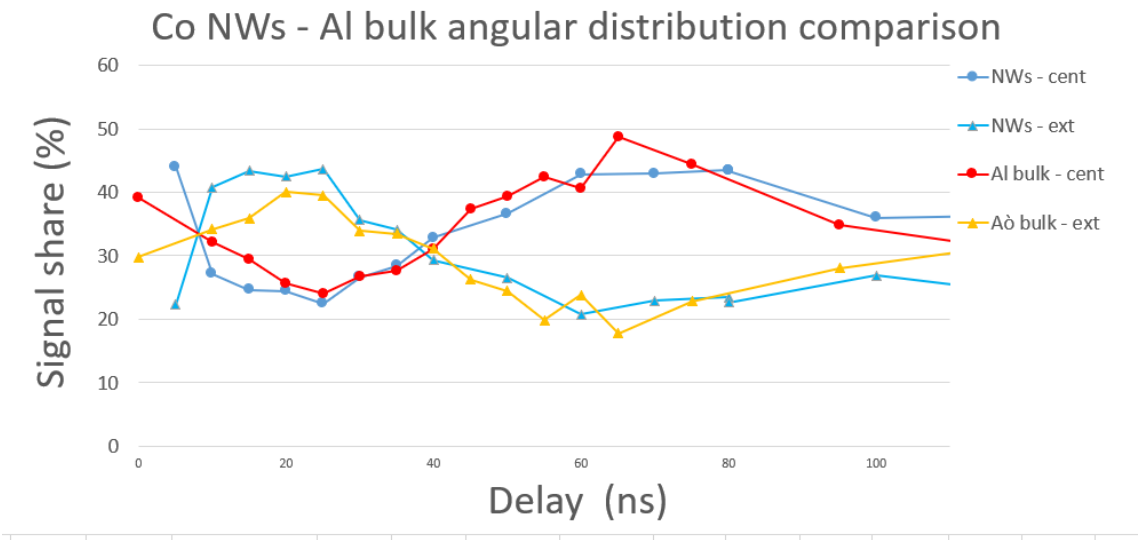

Figure 4.15: Distribution of signal between central, intermediate and lateral angular ROIs. Results are similar for the three nanostructured samples, so only Co-NWs is shown for clarity. While the very first points are unreliable due to strong fluctuations, from 10 ns (immediately after the laser pulse ends) to about 30 ns there is a substantial difference between the samples, with a strong central percentage of the signal for bulk Al compared to the nanostructured one.

As it can be seen in images 4.13 and 4.14, for both series the signal starts stronger in the external regions, mostly due to the initial lateral spread of the plasma, then it becomes stronger in the center as the plasma expands. However, the signal is relatively stronger in the center for the bulk target. This is probably due to the much weaker angular jets.

This difference is interesting, and suggestive of different dynamics in the first nanoseconds of plasma production.

The different radial evolution of the plasma plume was also analysed, comparing the signal per pixel at different distance irrespective of the angle. As can be seen in figure 4.16, however, no significant difference was found between the expansion of plasma from nanostructured targets and from bulk Al.

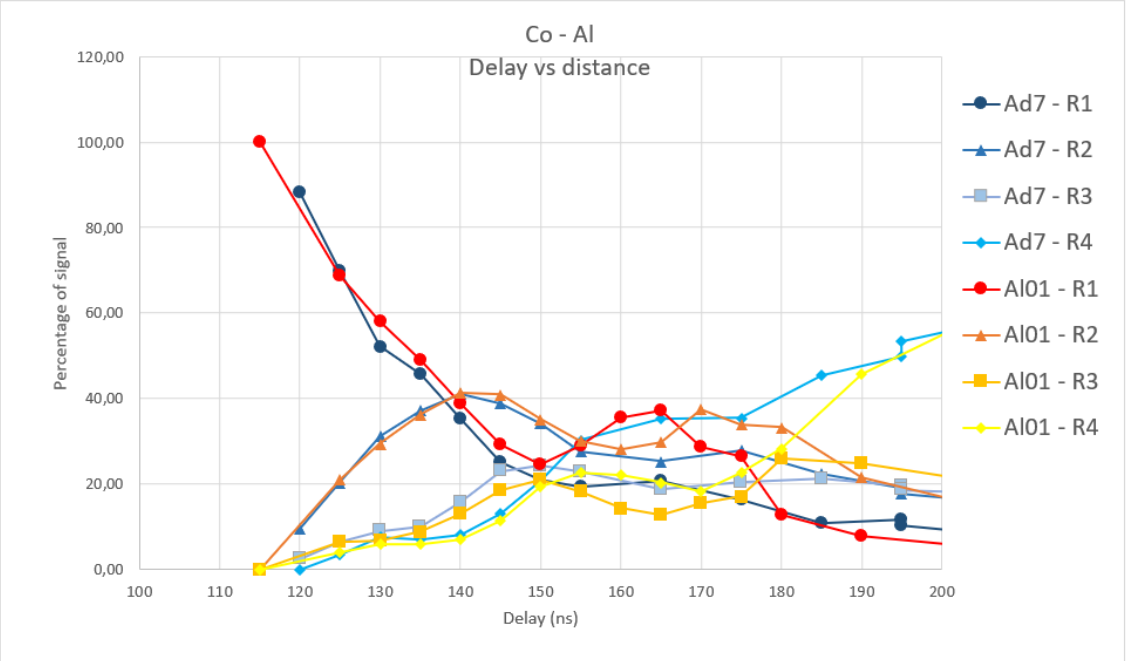

Figure 4.16: Time evolution of the visible emission intensity, normalized to peak, for the different samples

Another comparison is that between short and long nanowires, grown on different samples with different electrodeposition time. This comparison allows to understand the role nanowires play in shaping the plasma plume. As it can be seen in figure 4.17, in the tens of nanoseconds after shooting, plasma formed from the sample with shorter NWs has markedly stronger emission at high angles compared to samples with long nanowires.

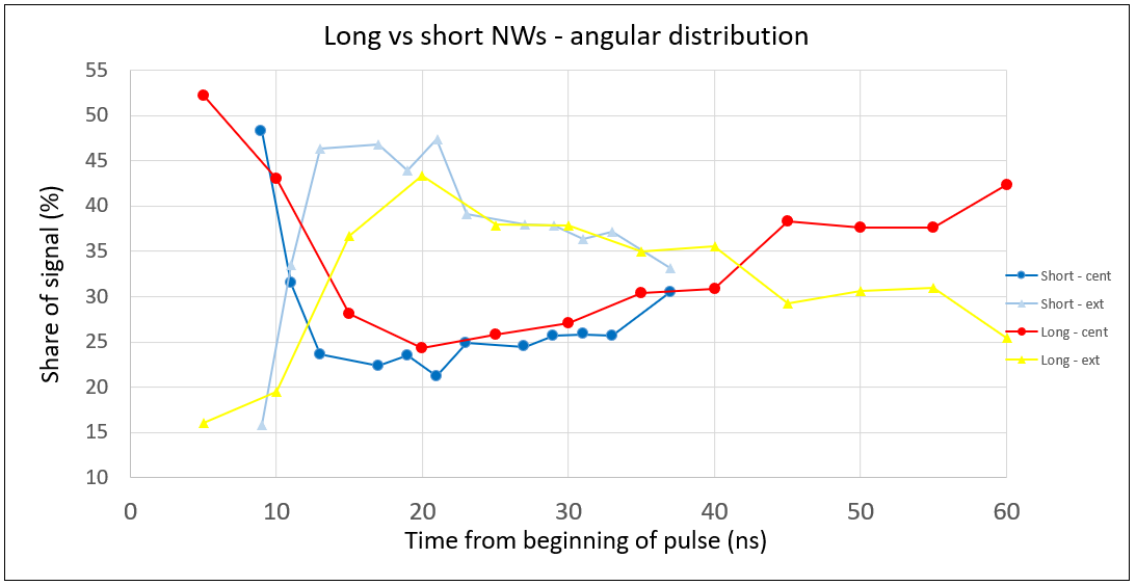

Figure 4.17: Share of signal in the angular region within 30° to the target normal ("cent") compared to the region more than 60° from the normal, for nanowires of different length. The signal in the intermediate region is not shown, since it is similar for all samples and over time.

While this might be indicative of a role played by nanostructure length in plasma formation, caution is required, because as will be seen in the next section, at least for X emission, only the outermost layer of the target played a role. If this is true for visible emission too, the shorter nanowires might have been too deep inside the channels to be part of the plasma, and thus the two plasmas in the series would differ in elemental composition, possibly explaining the difference.

Total intensity

As can be seen in figure 4.18, time evolution of the signal was similar for all the considered samples.

However, as it can be seen in image peak absolute intensity was substantially larger for nanostructured samples. This, however, is probably due to greater recombination emission by the heavy elements in the plasma. This is supported by the fact that the temperature, inferred by the X emission, turned out to be similar for nanostructured and bulk target.

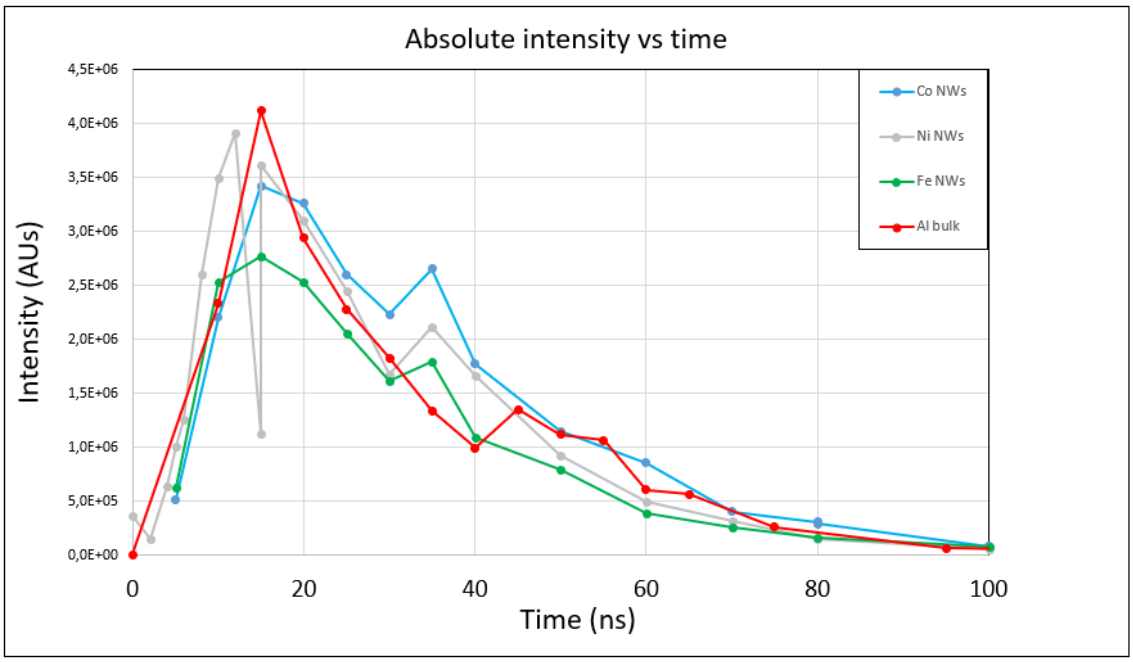

Figure 4.18: non-normalized total intensity of different targets vs time.

For a small number of events, peak emission was extremely high (more than five times the average), to the point of substantially skewing the data. This happened when the camera received direct light from the crater's inside, which was optically bright due to thermal emission. While the camera's angle was chosen in such a way to avoid imaging it, small differences in the target holder's position and inclination could move it into the field of view.

4.4 X-ray analysis in single photon mode

As previously detailed, the CCD camera sensitive to soft X-rays was used in two different modes: single photon and flux-integrating. In flux-integrating mode, a high flux of X-rays was allowed to reach the camera, losing information about spectral shape but allowing a measurement of plasma emission intensity over a wide range of values, since thicker filters can avoid saturation for strong signals and thinner ones allow sensitivity to weaker signal.

In Single Photon mode, a comparatively thick Ti (10 um) or Al (60 um) filter is put in front of the detector, so that only a minority of the camera's pixels are reached by the plasma emission.

While since 2018 the two modes were combined with a special absorber mask, they required different analysis and thus have been described in two different sections. A later section will describe the flux-integrating operating mode.

At first, an aluminum filter was used for the SP mode. However, preliminary data showed that the cutoff in transmission due to the Al absorption edge at 1.5 keV severely limited our ability to gather data except at lower energies. Due to this, a titanium filter was used in subsequent data takings.

4.4.1 Calibration

To calibrate the energy response of the CCD sensor for the Single Photon mode, a ^{55}Fe source was used, which has an emission line at 5.8 keV (actually two very close lines) and one at 6.49 keV. The source was put directly in front of the CCD, with only a thin aluminum absorber in front of it to screen Auger electrons. To collect enough events, but remain in SP mode, hundreds of images were collected with one-second exposure time.

Beside allowing to calculate the pixel counts/deposited energy ratio, this analysis allowed to observe how a several-keV signal spread through multiple pixels. In fact, figure **??** left shows the distribution of pixels counts under the 55Fe source: there are two peaks between 600-800 counts, but a long tail is visible at lower counts. The tail is due to the charge spread on neighboring pixels that happens when the diameter of the electron-hole cloud created in the semiconductor substrate (which is proportional to the X-ray energy) is larger than one pixel.

This probably happens because the cloud of electrons/holes in the semiconductor substrate created by the X-ray absorption had sufficient radius to involve more than one pixel.

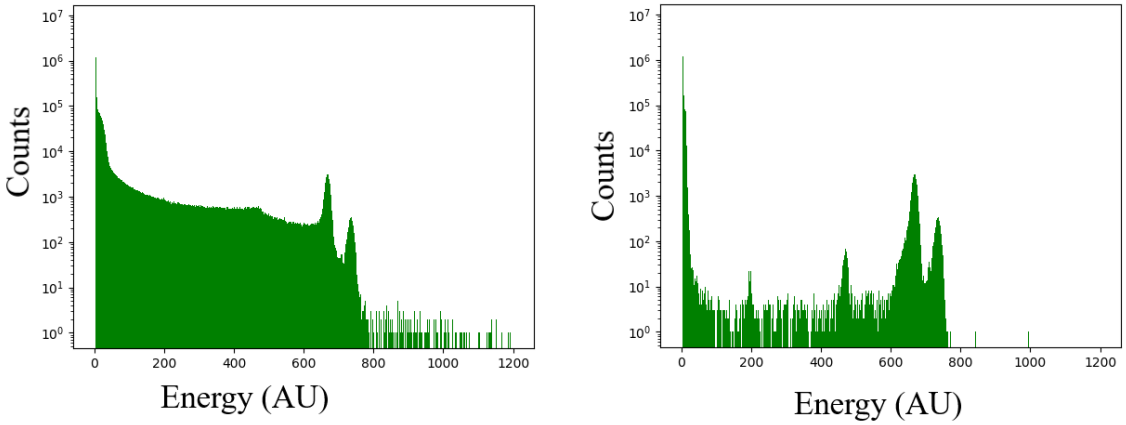

Figure 4.19: Histogram of signal collected in Single Photon mode, before (left) and after (right) applying a clustering algorythm. The large amount of signal before the peaks is actually the result of energy from a single event being split between two or more pixels

An analysis software was developed to scan the sensor data, select the hitted pixels (with counts more than four sigma above the background), identify clusters of pixels that

are consistent with a single photon, according to the rules (shapes) shown in figure 4.20. Clusters of any other shape are usually the result of two partially overlapping photons, and are discarded.

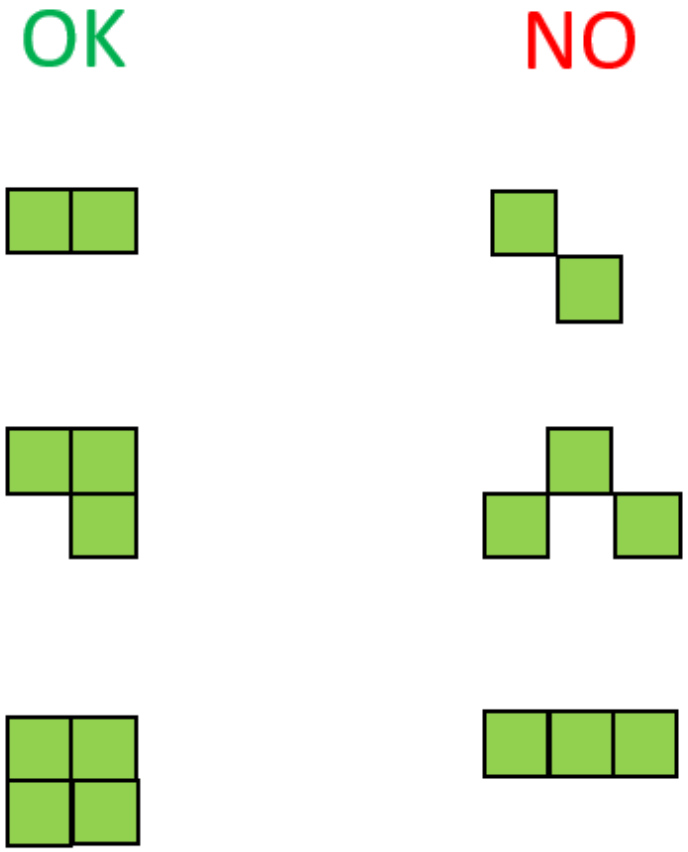

Figure 4.20: Shapes which were considered as legitimate consequence of a single high-energy photon

The resulting events are then used to calculate the calibration constant and the resolution. Calibration was repeated for different settings of gain, acquisition time and readout noise. The peaks in count distribution were fitted with a double Gaussian model, which made no assumption about the position and width of the peaks. For validation, the ratio between the two lines expressed in counts was checked against the known energy ratio of the spectral lines.

The fitted data can be seen in image 4.19-right. Table 4.22 shows the parameters derived from it. Results were validated by checking the ration between the 5.8 and 6.49 keV lines.

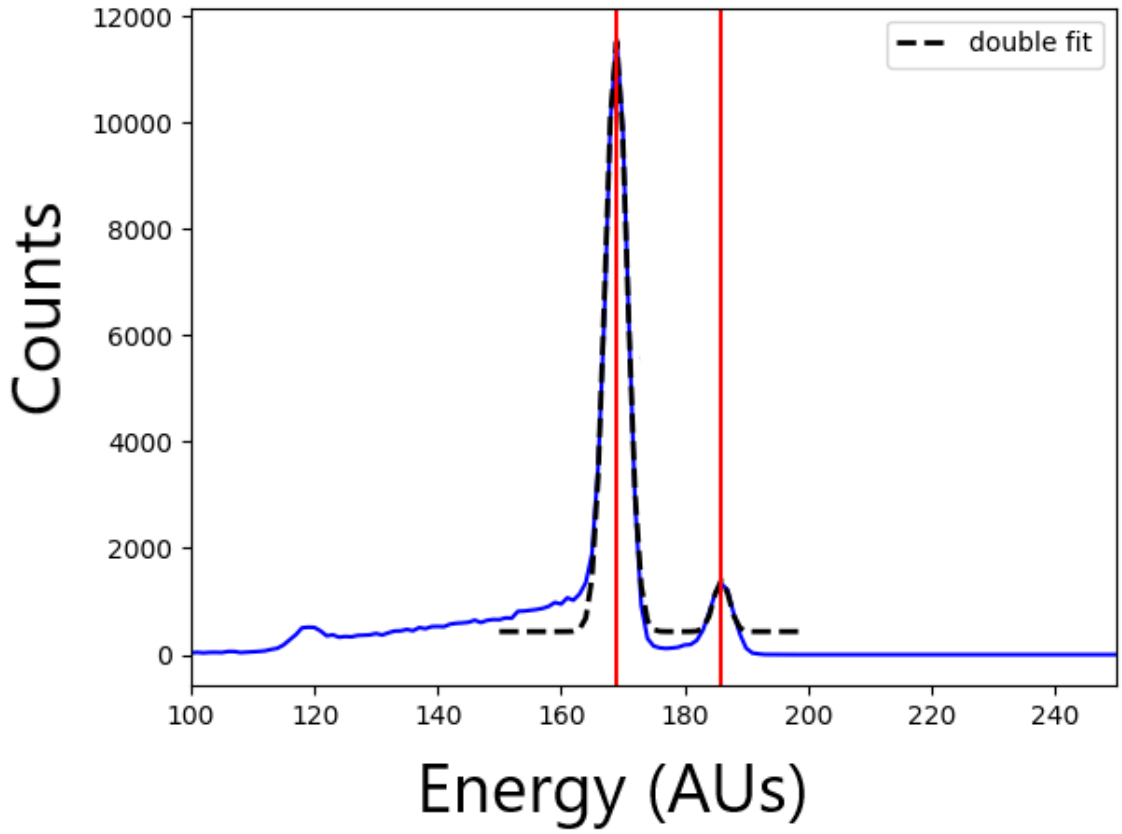

Figure 4.21: CCD counts vs energy after clustering of pixels

Rate (kHz)	Gain	Acq time (s)	E2/E1 ratio Observed	E2/E1 ratio Expected	Sigma (eV)	Cal const (eV/count)	Uncertainty (eV/count)
50	1	1	1,101	1,102	62	34,87	0,97
50	4	1	1,101	1,102	58	8,82	0,05
1000	4	0.01	1,100	1,102	106	9,44	0,16
3000	1	0.01	1,028	1,102	224	37,95	0,30
3000	2	0.01	1,101	1,102	115	19,89	1,01

Figure 4.22: non-normalized total intensity of different targets

The calibration constant (i.e. the conversion factor from counts to energy expressed in eV) seems to change slightly for different operating modes (readout and gain) of the CCD. Lower readout speed turns out to have a much better resolution, so it was used for this experiment, since there was no need to acquire images at a high rate. However, it was decided to use the lower gain setting, to avoid saturation in the brightest parts of the plasma.

The ratio between the 2 observed lines (E2/E1) is within uncertainty from the expected value, thus validating the calibration method.

Unfortunately, no lower energy source was available to check linearity at lower energies, but given the nature of the CCD sensor it seems a reasonable assumption.

4.4.2 Filter choice

The mask described in section 3.2.4 allowed to dedicate part of the sensor to operate in SP mode. To reach the required conditions of <1 photon per pixel, however, an appropriate filter was required.

At first, an aluminum filter was used. While at appropriate thickness (about 60 μm for maximum laser energy) the Al filter allowed to operate in SP mode, after analyzing preliminary data, it was apparent that the aluminum filter introduced a distortion due to the absorption edge at 1.58 keV.

After considering different alternatives, a titanium filter was chosen as the best replacement. As can be seen in figure 4.23 Ti spectrum is smooth in the 1-5 keV range, which is the region of interest. Ti spectrum's edge at low energy is not a problem since low energy photons are almost entirely suppressed anyway, while the 5 keV edge is higher than the vast majority of observed photons.

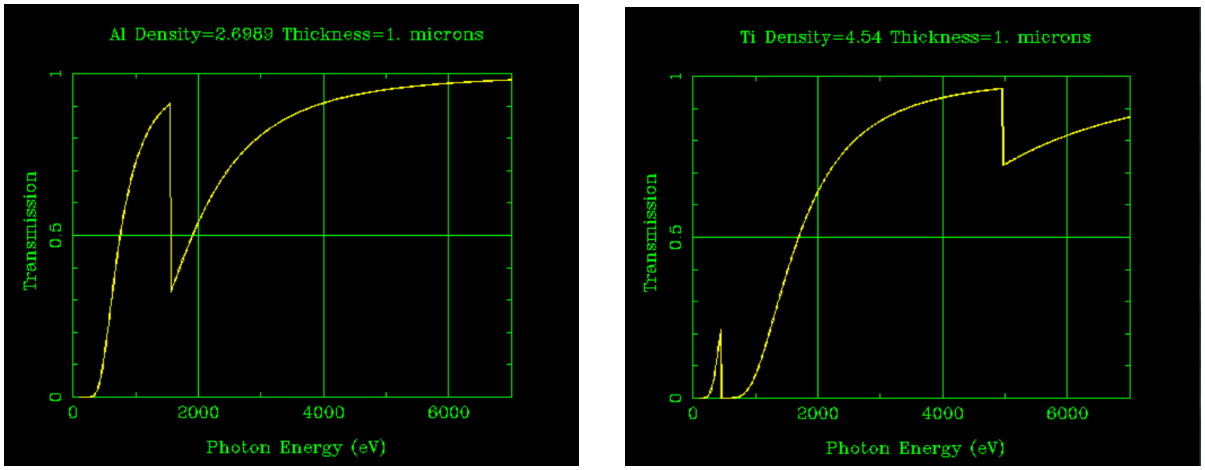

(a) **(b)**

Figure 4.23: Comparison between X-ray absorption in the keV range for 1 μm of Ti and Al. Aluminum's absorption edges cause significant spectral distortion, while Ti edge at 5 keV is at a very high energy compared to typical signals.

4.4.3 Observed spectra and temperature estimation

Since SP mode sharply limited the amount of data that could be taken for a single event, several shots were required to get usable statistics on a target. On the other hand, the interest was in seeing how the emission spectrum changes with variables such as beam

energy and polarization, so the events of a whole shooting session couldn't simply be combined as it had done for time evolution analysis. As a compromise, after focalization was found, ten laser pulses were fired for each set of parameters before moving to different beam conditions.

Spectra from a selection of the targets (Co NWs, Co bulk, and the multilayer sample with a thin Co coating) can be seen in figure 4.24. it was soon clear that single emission lines, or edges from recombination emission, couldn't be resolved. The signal excess (compared to an exponential decay) in the 1-1.5 keV range is probably due to line emission, but without more detailed information specific lines can't be resolved.

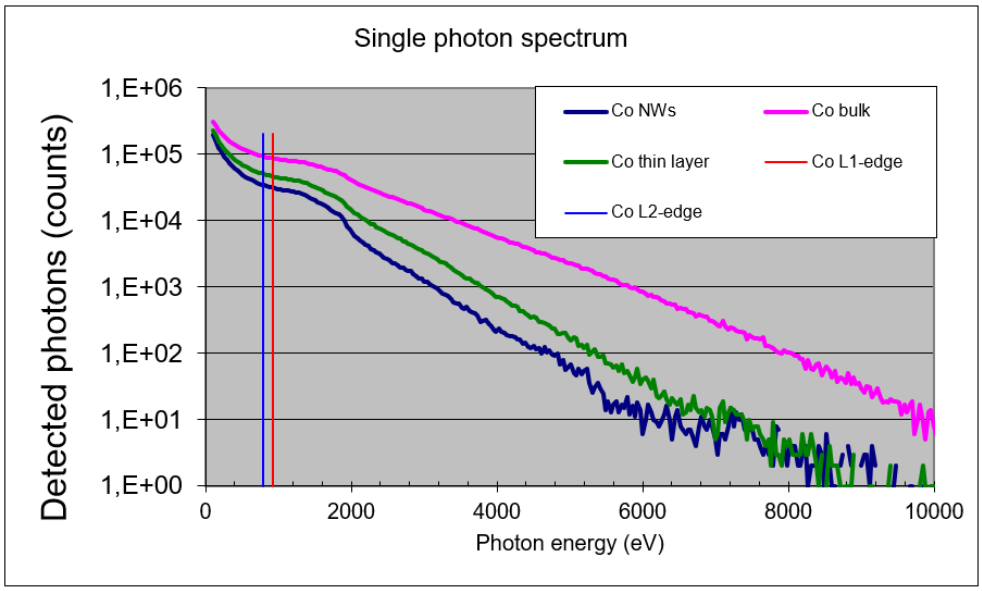

Figure 4.24: Single Photon spectra for Co NWs, Co bulk, and a multilayer sample with 1.2 μm thick Co layer. Potential emission lines for Co are shown. While there is a deviation from the exponential in the line region, no specific emission line can be singled out, and the spectrum is largely dominated by exponential decay.

This is probably due to several causes:

- Low energy resolution of the CCD detector
- Complex emission spectrum due to the different elements in the nanostructures (even if lines couldn't be resolved for the bulk control sample, either)
- Emission lines at low energy, possibly dominating, strongly suppressed by the titanium filter

The observed spectrum (which is modified by both the filter and the detector's quantum efficiency) is dominated by continuous emission. Whether by recombination or by bremsstrahlung, the spectral shape after the region of line emission is the same, with

emission falling exponentially with temperature. Therefore, the temperature could be calculated from the observed slope. However, the spectral distortion must be taken into account for such a calculation. Detector and filter efficiency could be in principle deconvolved, calculating the original source's spectrum, but the electronic noise from the CCD sensor would compromise the result.

Therefore, it was decided to take a different approach and estimate temperature by fitting the data with a simple software model.

For this purpose, only emission above 1.5 keV was considered, to avoid entirely the region with emission edges and lines, since that can't be easily modelled. At higher temperatures, it was assumed an emission falling exponentially with temperature (which is true for continuous emission of plasma, see section 1.1.3). So, a software was made which generated photons distributed this way, and simulated their probability of being absorbed in the filter and detected in the CCD pixels, adding shot noise and background noise. This was repeated iteratively for every plasma temperature (within a reasonable 100 - 300 eV range), and the resulting predicted spectra were compared with the observed ones via chi-square minimization.

Note that this model includes several assumption and simplifications. Beside assuming continuous-only emissions, it ignores the effects of integration over time, assuming the spectrum is dominated by the emission when the plasma is hottest, just after the shot is over.

4.4.4 Temperature comparisons

After several preliminary sessions to improve both the detection system and the analysis software, a set of bulk metal and nanowire samples were chosen for temperature measurements.

Absorber thickness couldn't be changed during an experimental session, since it's a lengthy process which requires partially disassembling the detector. Unfortunately, though, no single absorbed thickness allowed to stay in SP mode over the whole energy range. Either events at low energies were lacking, or there were too many events at high energies, making clustering impossible. Finally, a filter thickness was chosen that performed well in the intermediate region of available laser energies, to have data about the dependence of plasma temperature on beam energy. So, while the laser could shoot up to 1700 mJ per pulse, for most samples data above 1300 mJ were affected by saturation, and thus unusable for temperature measurement.

In table 4.25 samples used for temperature measurement are listed. Nanostructured samples with Ni and Co nanowires were used, since those elements led to the highest X-ray yield. Two nanostructured samples were treated with acid in order to partly dissolve

the alumina matrix, to obtain "freestanding" nanowires. One multilayer sample was also studied: 3 μm of Co deposited over an Al bulk sample. This sample was part of a set realized to study the depth of plasma formation, but it was also used as a control since it would produce mixed Al/Co plasma, elementally similar to the nanostructured samples.

Name	Label	Type	Metal	NWs ø (nm)	NWs length (µm)	notes
Co bulk	Co05	bulk	Co	\	\	\
Al bulk	Al05	bulk	Al	\	\	\
Ni bulk	Ni02	bulk	Ni	\	\	\
Co layer	Ad73	composite	Co	\	\	3 um Co over Al2O3
Ni NWs	Ad92	NWs	Ni	50	10	\
Co NWs	Ad98	NWs	Co	50	10	\

Figure 4.25: samples considered for temperature analysis from Single Photon

For every sample, measurements were taken at two different polarization angles were taken: at zero degrees polarization, electric field oscillation is always tangent to the target's surface, while at ninety degrees there is a component normal to the surface. A marked difference in response of polarization might suggest the nanostructures in the targets are reacting to light polarization, as expected by plasmonic interaction with light.

In table 4.26, temperature estimations for various samples are shown, with data for both polarizations.

sample	E (mJ)	T 0° (eV)	unc (eV)	Chi^2	N°photons
Co bulk	586	111	7	0,7	315
	714	117	3	0,4	863
	1070	162	3	0,9	3004
Al bulk	1060	129	5	1,1	3808
	1305	141	7	1,7	1021
	1770	204	11	1,6	470
Ni bulk	725	111	3	0,6	575
	1082	155	3	1,6	5681
Co layer	755	129	4	0,9	1200
	1064	146	3	2,1	5442
	1301	167	4	0,5	1992
Co free NWs	708	110	7	0,4	121
	713	107	4	1,0	470
	1066	140	3	2,1	4291
	1766	215	9	0,4	579
Ni free NWs	809	132	3	0,2	2272
	1066	149	3	2,0	3730
	1305	175	7	1,3	1274

Figure 4.26: Temperature estimation for the considered samples. Temperature is given for zero degree polarization, since there was no significant different with the 90 degrees results.

Co and Ni bulk targets turned out to have substantially higher plasma temperature than Al. For practicality, uncertainty and square chi is presented for the zero-polarization data only, but both were very similar for the ninety-polarization data.

Plasma from nanostructured targets turned out to comparable in temperature to bulk sample, with little difference between the nanostructured samples. This is consistent with plasma from nanostructures behaving mostly like a mixture of its constituent elements, and contribution fro heavy elements dominating emission.

Plasma from the multilayer sample behaved in a similar way to the bulk Co sample, which supports the hypothesis that only the first micrometers of every target's surface become part of the plasma. More data supporting this will be presented in the next subsection.

4.5 X-ray analysis in flux-integrated mode

As explained in the previous sections, the CCD camera could be used with a thin filter (3-30 μm of aluminum) as an integrating detector. While this operating mode yields no spectral information, it allows an easy comparison of spectral intensity for different samples and/or different conditions, and doesn't require a large number of shots to expand statistics.

Also, since it's simpler in hardware and software requirements, it could be used earlier and thus gather more data in this mode. Since the aluminum filters, necessary to avoid over exposition, and the quantum efficiency of the CCD camera reduce the X-ray flux of energies <0.8 keV, and low energies dominate the spectrum, this data couldn't be used to reconstruct how much energy, in absolute terms, was radiated as X-rays. However, since little difference in spectral shape could be found between the samples, relative intensity can be taken as an indicator of better X-ray conversion efficiency.

However, it should be noted that if a targets emits more X-rays than another, it could be due to either hotter plasma or longer lived emission. Information from other detectors must be taken into account to interpret the data.

4.5.1 Analysis software

While simpler than SP analysis, flux-integrated analysis still required some image analysis. A typical raw image (from a ten hole mask, with aluminum absorbers of different thickness in front of each hole, used in the first experimental sessions) can be seen in figure 4.27.

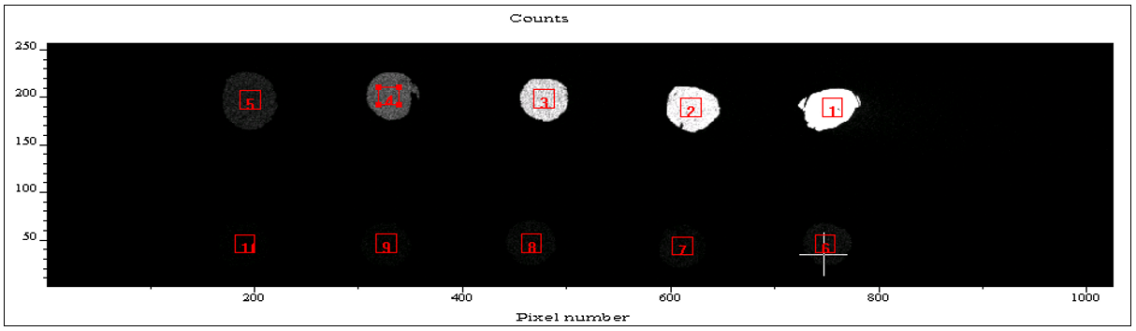

Figure 4.27: raw images from the CCD camera, rendered through the ANDOR software. Brighter pixels correspond to higher counts. The irregular shapes and great intensity variation between spots makes analysis more complex.

The high intensity spots correspond to the holes. Analysis evidenced the existence of small penumbra zones around the bright region, and dark spots within them. The darker

spots are probably due to defects of the CCD sensor, since they are consistent across all events.

To take this into account, at the beginning of each experimental sessions, some shots are fired on bulk targets to observe the resulting hole pattern. A software was developed to automatically identify the bright regions, excluding penumbra zones and dark spots. This is achieved by excluding the pixels which deviate more than four standard deviations from the median value for a given spot.

The remaining pixels are considered valid, and each spot's pixels are averaged to get a data point, along with its standard deviation - which is usually very low, since experimental error turned out to be dominated by variation between events. In the first data takings, this was very especially important since the hole mask had several fabrication issues. Feedback from this kind of analysis helped create a better and more regular mask for later data takings. The result can be seen in figure 4.28, with much more regular exposition for the newer masks.

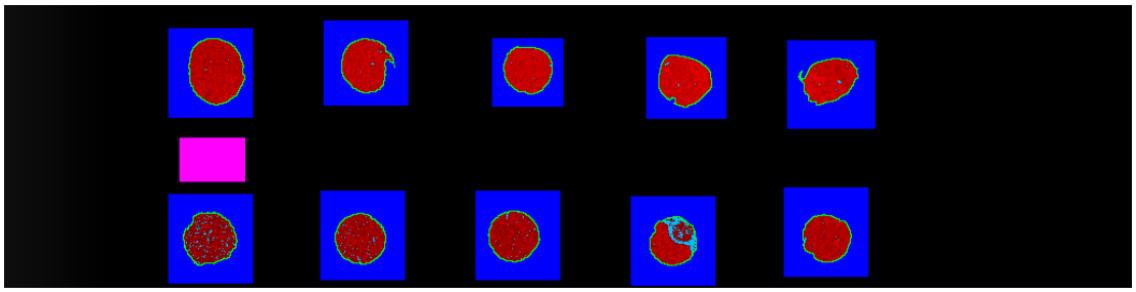

Figure 4.28: Feedback from the analysis software allowed to fabricate better masks, and to verify that filters led to even illumination. Blue regions of interes were designated around each hole, and the software detected the holes profile from those. The violet region has been used for background calculation.

4.5.2 Nanowires of different metals

Targets with nanowires of different metals were tested to determine which one lead to higher X-ray emission, since that could mean better laser light absorption or longer plasma confinement time. In table 4.29 the samples considered for this analysis are listed. Since preliminary tests had shown emission was dominated by the heavy element of the NWs, bulk targets of the same metal as the NWs were used as control.

The data presented are those at "zero" polarization, meaning the beam's polarization is such that the electric field oscillations have a component normal to the target's surface. Polarization contribution will be discussed in more detail later.

Name	Label	Type	Metal	NWs ø (nm)	NWs length (µm)	notes
Al bulk	Al02	bulk	Al02	\	\	
Ni-thin	Ad3Ni	NWs	Ni	20	8	
Co-thin	Ad7Co	NWs	Co	20	8	
Fe-thin	Ad10Fe	NWs	Fe	20	8	
Ni-long	Ad20Ni	NWs	Ni	50	20	
Ni-short	Ad20Ni	NWs	Ni	50	10	
Ni-DC	Ad22Ni	NWs	Ni	20	10	contacted on substrate
Ni-free	Ad22Ni	NWs	Ni	20	10	Alumina removed, contacted

Figure 4.29: integrated X-ray flux comparison between different samples. Flux values are expressed as CCD count per pixel.

Results can be seen in figure 4.30, with measured X-ray flux at different laser energies for each considered sample. Data are taken from a single width of absorber, since fluxes from the different absorber were strongly correlated.

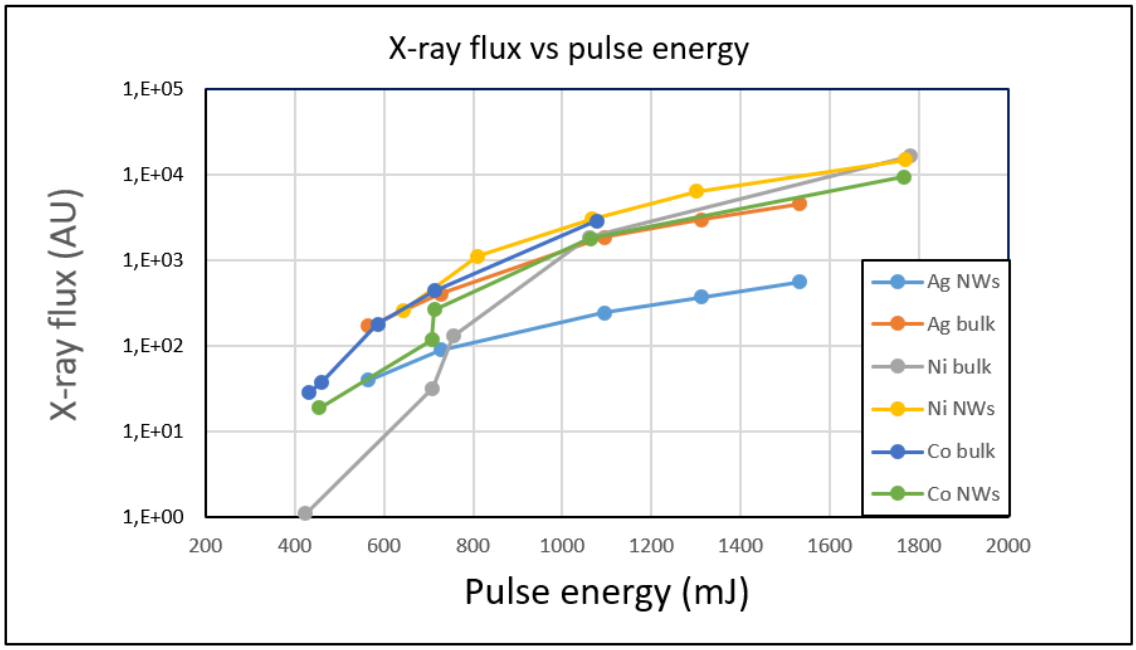

Figure 4.30: integrated X-ray flux comparison between different samples. Flux values are expressed as CCD counts per pixel. Error bars are within the points.

As can be seen, Ni and Co NWs yield higher fluxes than Ag NWs. Bulk Co yields a similar flux to Co NWs, while Ni NWs yield a similar flux to the control bulk at high energy, but a higher flux at low energy (the very lowest energies, however, were affected by strong fluctuations). Ag nanowires, on the other hand, yielded a flux lower than the bulk counterpart by a factor of two or more at all energies.

Flux from bulk Al isn't shown as it is lower by an order of magnitude compared to the other targets'. This might seem surprising since, for nanostructured targets, the ablated material is mostly Al2O3 by mass. However, as previously noted heavier elements have a

much stronger continuous X-ray emission, so the metals in the NWs dominate the X-ray emission.

It's noteworthy that at lower laser energies, emission from nanostructured targets is closer to that of bulk targets. As will be discussed in more detail later, a possible interpretation is that nanostructures improve laser absorption by the sample, as described in section 1.2, but at some point during irradiation they are destroyed, and the target behaves like a simple composite material. At lower energies, nanostructures might provide a more substantial contribution before being destroyed.

4.5.3 Nanowires with different geometry

Since it is possible to control several geometrical parameters of the nanowires, some targets were specifically created to test the impact of NWs geometry on plasma production. In particular, the interest was in assessing the impact of diameter and length of nanowires.

Name	Label	Type	Metal	NWs Ø	NWs length	Notes
Al bulk	Al02	Bulk	Al02	-	-	
Ni-Thin	Ad3	NWs	<10	20	8	
Co-Thin	Ad7	NWs	<10	20	8	
Fe-Thin	Ad10	NWs	<10	20	8	
Ni-Long	Ad20	NWs	5	50	10	
Ni-Short	Ad20	NWs	10	50	5	
Ni-DC	Ad22	NWs	10	20	10	Freestanding NWs
Ni-Free	Ad22	NWs	10	20	10	Freestanding NWs, contacted

Figure 4.31: Gradient of samples with nanowires of different length. Longer NWs lead to greater light absorption, and thus a darker color.

In table 4.31 the parameters of the tested samples are shown. Note that the targets with different NWs length are the same physical sample: half of it was taken out of the solution midway through deposition, resulting in two regions with different length of nanowires, but identical in every other aspect. Note that nanowires height is a key parameter in the sample's coupling with light: longer nanowires absorb more light, reaching the darkest color (>90% absorbance for visible light) at about 15 μm. See figure 1.4 for a striking example of how NWs length affect color.

Nanowires diameter doesn't have obvious effects on light absorbance, but since it's closely associated with distance between nanowires, it might affect resonance between light and nanowires. Finally, due to the complexities of plasma evolution it wasn't sure whether the removal of the alumina layer would improve or hinder plasma formation.

This was one of the first analyses, so it was necessary to rely on integrated X-ray data because other data taking modes weren't fully operational yet. However, this was sufficient to draw several interesting conclusions.

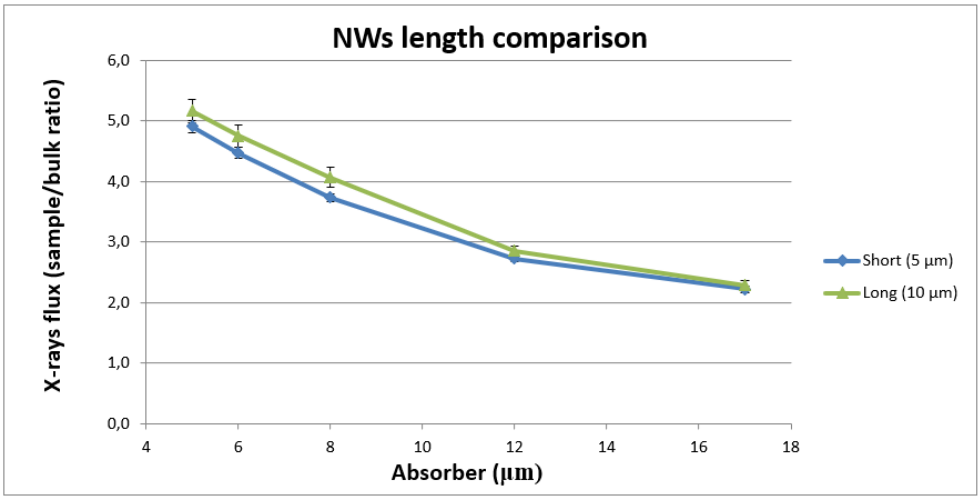

Figure 4.32: X-ray flux after Al absorbers of different thickness for targets of different nanowires length (10 μm and 20 μm). The difference is comparable to standard deviation for all data points. The flux is normalized to that of bulk Al samples for the same absorber.

Length comparison results are shown in figure 4.5.3. As can be seen, there is little difference between emission from longer and shorter nanowires. This lead to question how deep the plasma formation enters the target. As it will be shown later, it turned out to be only a few micrometers deep, based on the results: the nanowires were already long enough to reach high absorbance, and plasma production is too superficial to make the difference in length matter.

Diameter comparison (figure 4.5.3) leads to similar results: NWs of the same element and length lead to similar X-ray fluxes despite the difference in diameter. This wasn't surprising, since distance between nanowires is small (<100 nm for both kinds) compared to the 1052 nm wavelength of the incoming laser, so it was unlikely that resonance played an important part.

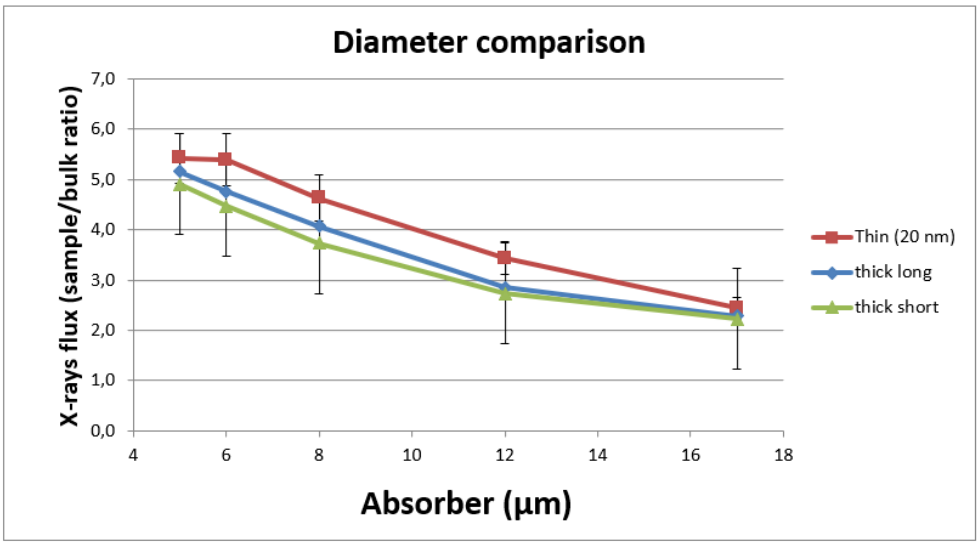

Figure 4.33: X-ray flux after Al absorbers of different thickness, for targets of different nanowires diameter. The difference is comparable to standard deviation for all data points.

More interesting results came from the comparison between nanowires still immersed within the alumina layer and those freed by chemical etching (see figure 4.5.3. Flux was much more intense for freestanding nanowires, comparable to that of bulk metal. This seemed to indicate the light elements Al and O in the barrier layer, despite alumina being transparent, limit the interaction between nanowires and laser light.

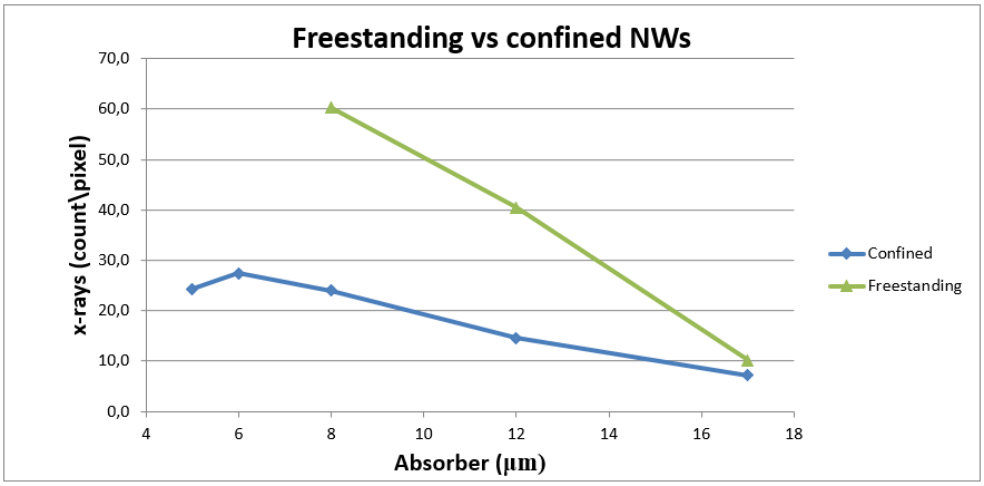

Figure 4.34: X-ray flux after a 10 μm Al absorber for targets of freestanding and confined nanowires. Flux is much higher for freestanding nanowires.

4.5.4 Polarization analysis

Since it was interesting to assess the impact of nanostructures in plasma evolution, a key parameter to study is response to polarization. As discussed in section 1.2, nanowires

are sensitive to light polarization due to their directional nature. Since our targets were held at thirty degrees relative to the beam direction, and the beam is linearly polarized, beam polarization has a component either tangent or normal to the target's surface. The component normal to the surface is aligned with the nanowires, which could lead to stronger absorption, as can be seen in the spectral analysis in figure 4.5.4.

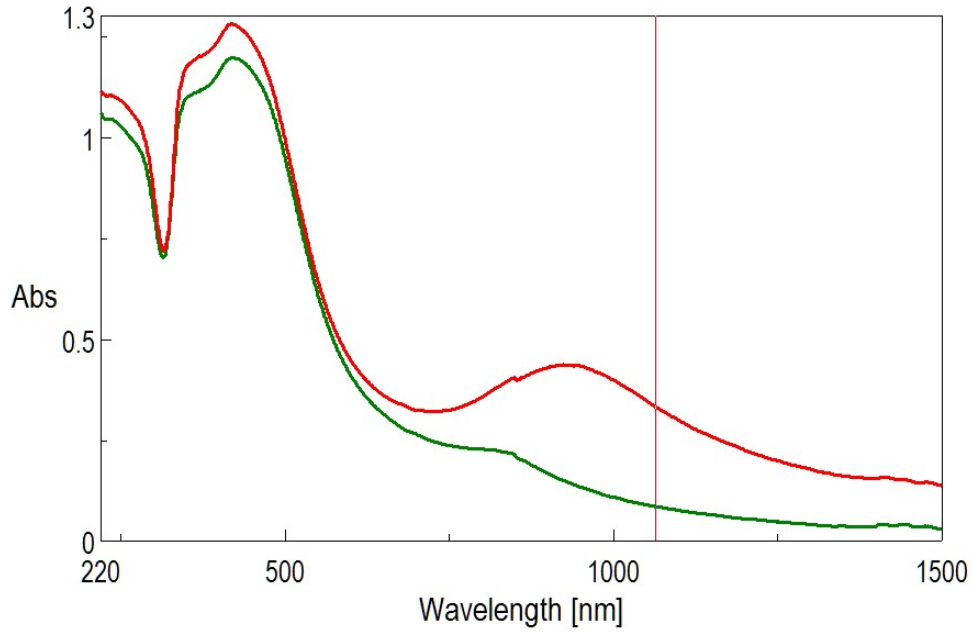

Figure 4.35: Absorbance vs incident wavelength for Ag NWs. The two lines differ in polarization: the red line has a component normal ("p" wave) to the surface, the green line has the polarization axis tangent to the target surface ("s" wave).

So, a half-wave plate was used to rotate the plane of polarization, so a series of shots could be taken with polarization entirely tangent to the surface and a series with a component normal to the surface. Since this could easily be changed, a selection of targets were tested at several different energies. Shots at different polarization were done on the same targets, so all other conditions can be assumed to be equal.

The most relevant results are those from comparing Ni and Co NWs - the most emissive kind - with bulk metal.

Two set of measurements were performed: first the polarization angle was changed at constant energy, then energy was gradually changed, but only using 0° and 90° polarization angles, which should lead to the maximum difference.

For the polarization angle scan, all taken at about 1500 mJ, results can be seen in figure

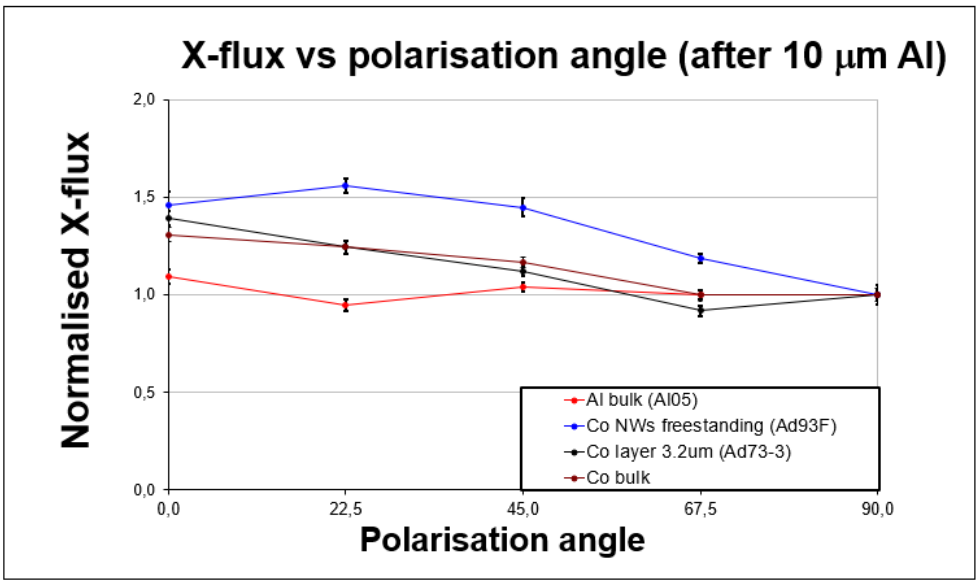

Figure 4.36: Flux ratio, normalized to the 90° value, for different samples and different polarization angles, at the same nominal energy of 1500 mJ.

As it can be seen, the Co NWs samples has substantially higher emission at 0° and low angles, and lower emission nearer to 90°. This applies to a lesser extent to the multilayer samples, especially the one with a thinner layer. The difference is smaller for Co bulk, and Al bulk has no polarization difference within uncertainty.

It is unclear why multilayer targets reacted to polarization more strongly than either of the metals composing them. It should be considered, however, that alumina with empty nano-channels lies between the thin metal layer. Even without nanowires, the channels in the allumina could react to polarization along their axis.

More interesting results come from the study of the polarization ratio (flux 0°/flux 90°) at different energies. Considered targets can be seen in table 4.37, and results can be seen in figure

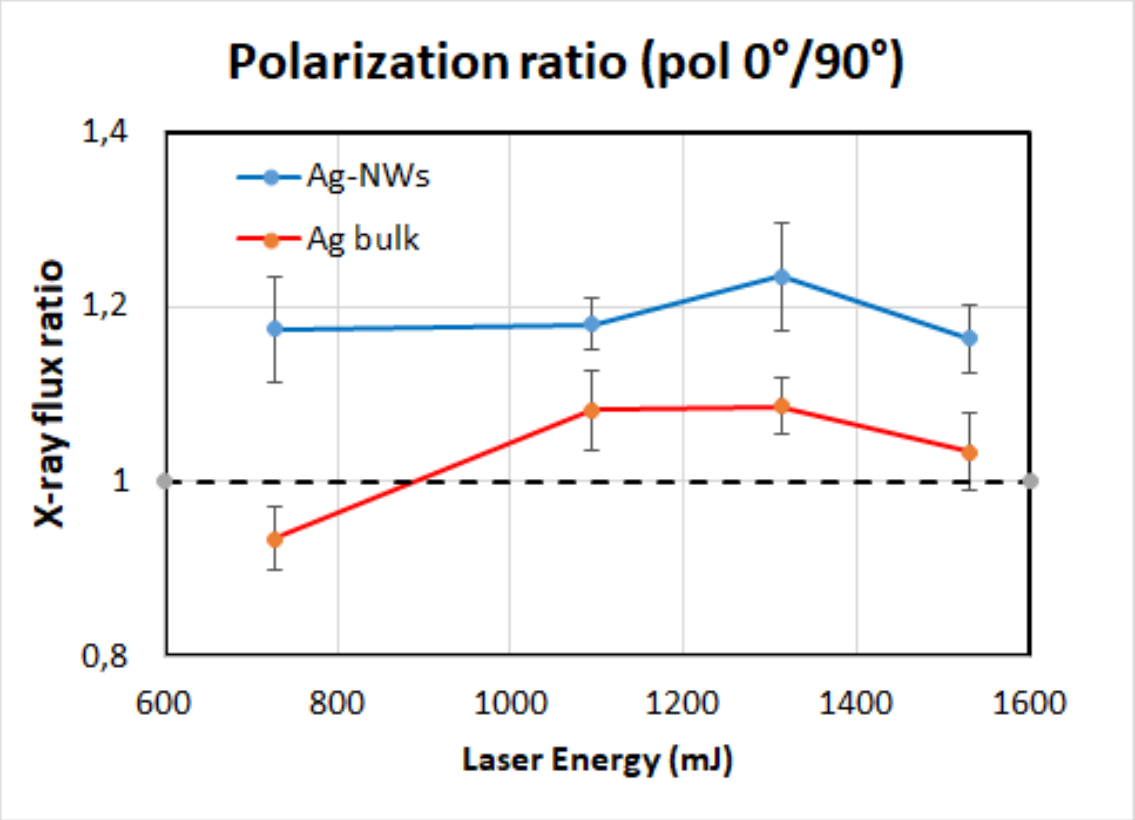

Figure 4.37: Polarization ratio for Ag NWs and Ag bulk at different energies.

As can be seen the X-flux ratio for the nanostructured target increases by about 20% with respect to the unity, at all energies. This means that when the polarization axis of the incoming radiation has a component perpendicular to the target surface, the coupling with the nanowires increases. On the other hand, the X-flux ratio for the bulk target is consistent, within errors, with the unity at all beam energies, as expected. This confirms that the plasmonic coupling can give a contribution in the radiation absorbtion, even if the duration of the laser pulse is much longer than the plasma formation times.

4.5.5 Plasma penetration study

An important question to interpret our data properly was how deep into the target was material ionized. As previously shown, craters were almost 100 μm deep, but ablation can occur due to melting and vaporization, without necessarily reaching ionization.

To ascertain this, the different X-ray conversion efficiency of Co and Al was exploited. Co plasma is much more emissive than Al, as had already been ascertained, so a special target was realized with a layer of Co deposited over an empty alumina matrix (10 um thick) on the aluminum subtsrate.The Co deposition was obtained by electron-gun evaporation, with two layers of different thickness. Together with two control samples

(one of Co and one of Al), this allowed to investigate if a comparatively thin (1.2 and 3.2 μm) layer of Co would be sufficient to obtain a plasma behavior similar to bulk Co. So, the samples considered for this analysis are listed in table 4.5.5.

Plasma penetration study - samples			
Name	**Label**	**type**	**layer height (µm)**
Bulk Co	Co01	bulk	\
Bulk Al	Al05	bulk	\
Thin Co layer	Ad73-A	Multilayer	1,2
Thick Co layer	Ad73-B	Multilayer	3,0

Figure 4.38: Samples considered for the plasma penetration analysis. Beside the Al and Co bulk control, two region of the same physical Al support were deposited with Co layers of different thickness.

The results of this analysis can be seen in figure 4.39. X-ray fluxes for different energies are shown for each target. As was already known, bulk Co has a much stronger emission than bulk Al. The sample with the thin layer has an intermediate level of emission between Al and Co, while the one with the thick layer has a slightly superior yield compared to bulk Co. This might be due to small systematic differences (like focalization) or be the result of a role played by the alumina channels in coupling with laser light.

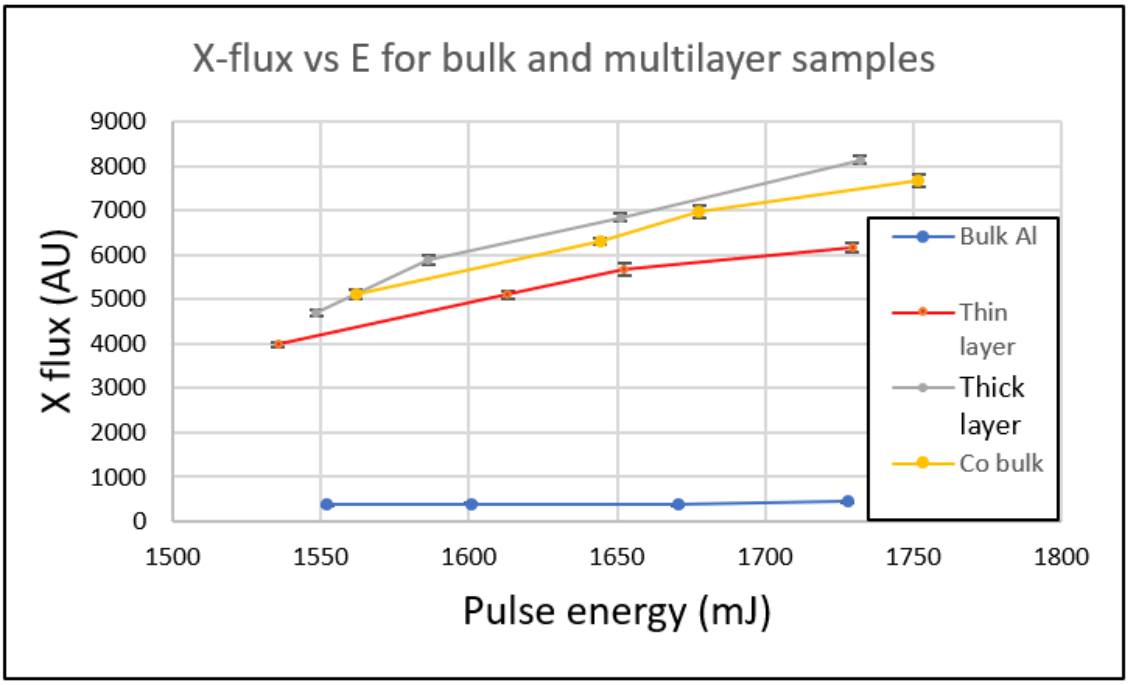

Figure 4.39: Samples considered for the plasma penetration analysis. Beside the Al and Co bulk control, two region of the same physical Al support were deposited with Co layers of different thickness.

This led to the conclusion that plasma formation only involves the top ≈ 2 μm of the target, while ablation goes much deeper (>100 μm). The underlying material is melt or vaporized, but not ionized. This confirmed the choice of freeing nanowires from the alumina layer as reasonable, otherwise the resulting plasma is mostly alumina, and can't be compared with bulk metal.

4.6 Preliminary results from green laser

The PLANETA experiment had a second laser facility available at L'Aquila, where a frequency-doubling system allowed to fire 532 nm laser pulses, by exploiting the second harmonic of a 1064 nm wavelength.

The comparison was extremely interesting not only to provide confirmation of the results in Catania with a different setup, but also to detect possible resonance effect between the laser's wavelength and either the length or grid spacing of the nanowires.

At the time of this writing, only preliminary data have been collected and analysed from L'Aquila, with a limited number of samples tested compared to Catania and only integrated X-ray flux available. However, this already allows some considerations on the bulk samples vs NWs ones.

4.6.1 Available samples

At the time of this writing, only one nanostructured target has been irradiated at L'Aquila, together with two bulk control samples. Their parameters are listed in table 4.40

Sample	Type	NWs ø	Heigth
Ag NWs	Nanowires in alumina	50 nm	10 µm
Ag bulk	Bulk	\	\
Al bulk	Bulk	\	\

Figure 4.40: Targets chosen for irradiation at L'Aquila

Silver and Aluminum bulk targets allowed to compare the mixed plasma from composite nanostructures (Ag nanowires in alumina) to their components.

4.6.2 Focalization and energy stability

The beam was focuses by mazimizing X-ray output, and spot diameter was determined by post-irradiation sample analysis to be about 200 μm spot, similar to the 1064 nm setup in Catania. The laser could shoot at two energies: high energy (about 1400 mJ) or low energy (about 490 mJ), yielding a similar range of available power density to the infrared laser in Catania. However, the efficiency of the KDP crystal used for frequency doubling was highly sensitive to temperature change caused by the beam passage. Therefore, it had to be re-aligned every 10-20 shots, and energy could drop as much as 5% before re-alignment. This fluctuation can't be avoided with current setup, and adds a fluctuation to the energy of different events, which would ideally be constant.

4.6.3 Metal Filters

As described in the previous section, the only detectors available so far at L'Aquila were pin diodes sensitive to X-Rays, but working only in flux-integrated mode. In front of each diode a metal sheet was put as a filter, to reduce X-ray flux and keep out visible light. The data used for analysis comes from the diode directly facing the target, which was filtered with different materials at different times.

The filters used were 2 μm of titanium, 1 μm of nickel, 3 μm of aluminum. Filters of different metals allowed some spectral sensitivity, since they have different spectral response, especially in the 0.1 - 2 keV range which was expected for the laser-produced plasma.

To understand the choice of filter materials, it must be considered that (as expected from literature and observed for infrared laser), most plasma emission is expected to be from bremsstrahlung and recombination. These emission processes have the same functional dependence: $I \propto \exp \frac{-E}{kT}$, with E being photon energy and T being plasma temperature, which was expected to be in the hundreds of eV range. Given this, and knowing the detector's quantum efficiency, the filters were chosen to highlight different regions of the resulting spectrum. The relevant spectra are shown in figure 4.41

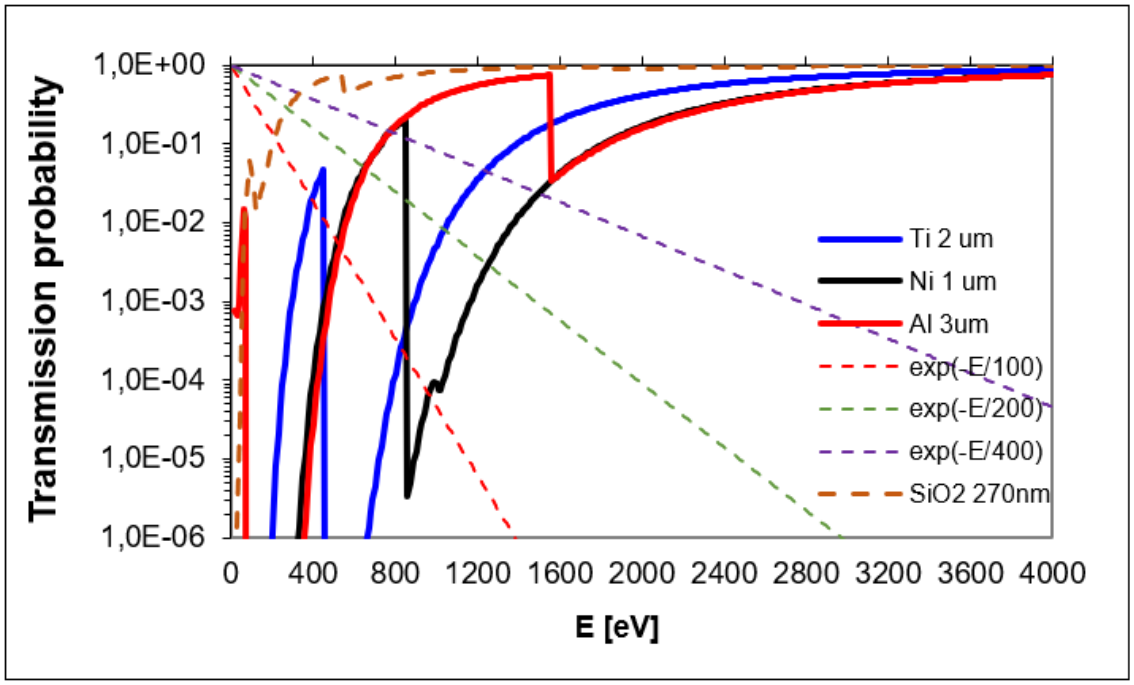

Figure 4.41: Trasmission spectrum for the filters (2 mm Ti, 1 mm Ni, 3 mm, Al) and for 270 nm SiO2 , representing the dead layer (i.e. the quantum efficiency) of the PIN photodiode. Three Bremmstrahlung curves (dashed lines) for T=100, 200 and 400 eV are also shown, as an indication of a plasma emission spectra at a given temperature.

As can be seen, Titanium has the highest transmission for low energies, Nickel for intermediate energies, and Aluminum for relatively high energies.

A photon generated by the plasma must pass through the filters and be detected by the diode to contribute to the signal. Therefore, filter transmission must be multiplied by quantum efficiency to understand the effect it has on the incident spectrum. Multiplying the expected signal by the resulting effective quantum efficiency, the expected effect of the different filters can be predicted. In figure 4.42, an example of the expected result for 200 eV plasma can be seen.

Since the three filters affect the incident spectrum in different ways, it's possible in principle to predict the ratio of signal past each filters at different temperature (figure 4.42).

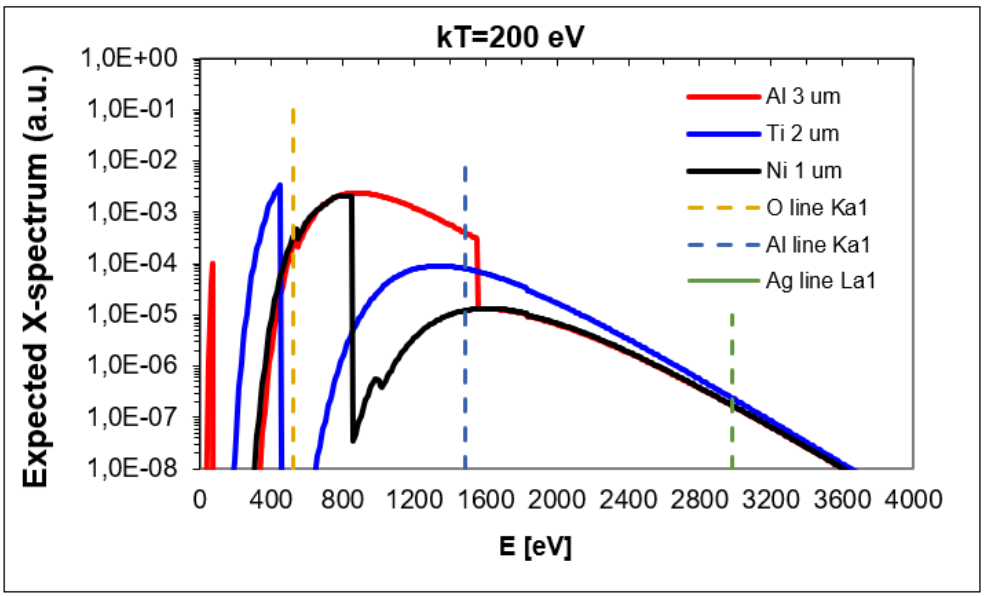

Figure 4.42: Convolution of the trasmission spectrum of each filter with the detection efficiency and the emission spectrum of a generic plasma described by a Bremmstrahlung with a given temperature, 200 eV in this case. Vertical dashed lines indicate positions of the principal emission lines for 8O, 13Al and 47Ag.

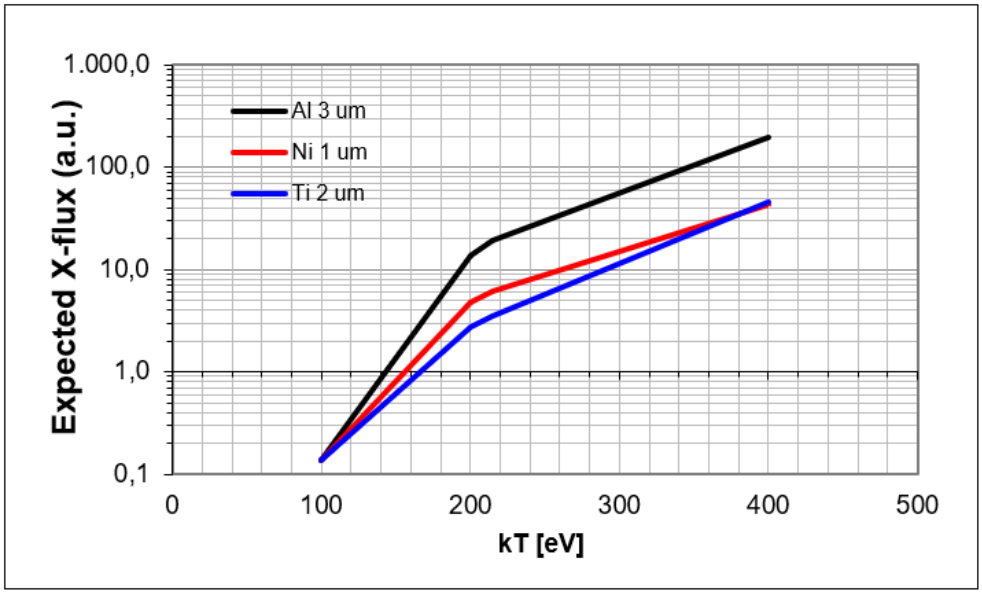

Figure 4.43: Expected flux (arbitrary units) as a function of the plasma temperature, for the 3 filters.

While realistically phenomena like line emission, uncertainties of emission spectrum and limited available data don't allow to calculate temperature with this system, this simple model is a useful reference to compare the actual data.

Pin diodes singnals were sampled with a LeCroy oscilloscope at 5 GHz. The oscilloscope trigger was synchronized with the laser pulse. Typical signals are shown in picture

4.44.

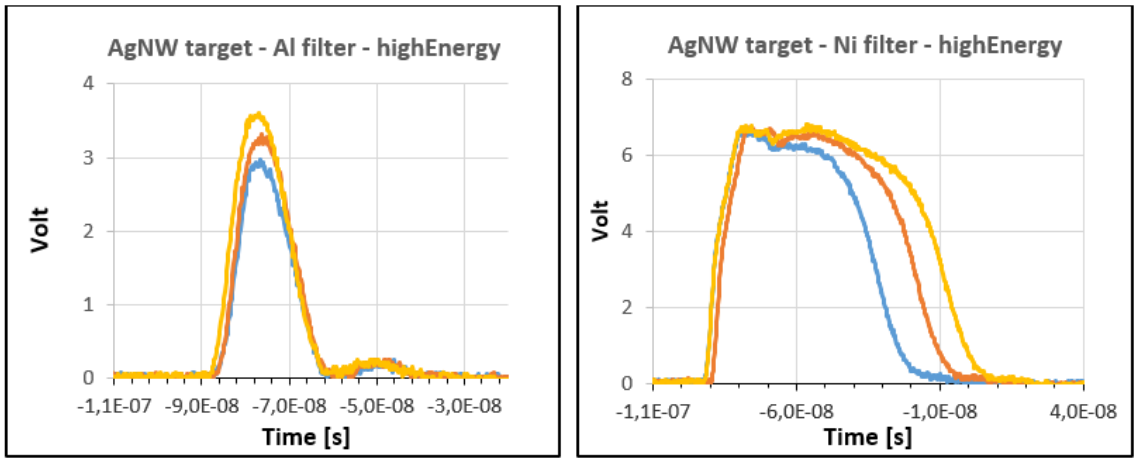

Figure 4.44: Sample events recorded by pin diodes at L'Aquila. On the left, three events from laser shooting at low energy. On the right, three events at high pulse enrergy. Diode saturation can be noticed on the latter.

Typical signals were 10 to 100 ns long, with a roughly gaussian outline. For the events with highest flux, saturation occurred, as can be seen on the right in picture 4.44. In this case, signal intensity is not directly proportional to the incoming energy, and charge collection time is considerably extended. A thicker filter would prevent saturation, but could make lower energy signals too weak too detect.

To analyse the data, it was necessary to account for the background signal. Background is thought to come primarily from two sources: electronic white noise and direct light from the pulse reaching the sensor after being reflected inside the interaction chamber. Visible light should be prevented from reaching the pin diode by the metal filter, but thin metal foil can have microscopic holes, which allow some light to reach the detector. While the electronic noise can be subtracted event-by-event by measuring the baseline signal before the trigger, the same can't be done for visible light reflection. To measure the contribution from visible light, some shots were fired with air instead of vacuum inside the interaction chamber. Thirty cm of air have little impact on 532 nm light, but completely absorb X-rays in the <2 keV range, so the signal with air in the chamber must be due to visible light. It was found that no visible light background can be detected for low energy pulses, while some signal can be seen for high energy pulses, especially for bulk Al. This is probably because bulk Al targets are more reflective than nanostructured targets. Even for the worst case, however - event from shots on Al targets with Ti filter (which absorbed the most signal), signal was more than fifty times larger than noise.

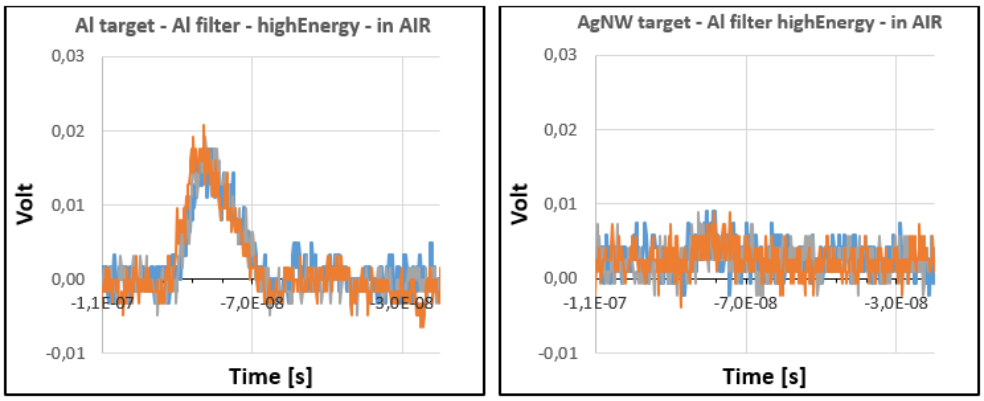

Figure 4.45: Observed signal from the pin diodes, with air-filled interaction chamber, for high energy (left) and low energy (right) events.

4.6.4 Data Analysis

As explained in section 3.3, three pin diodes were used as X-ray integrating detectors. While they have no intrinsic wavelength discrimination, using different filters it's possible to obtain some basic spectral information and to compare the integrated value between different samples. Preliminary analysis was conducted by irradiating three different targets (see previous section) at two different energies (high and low), and measuring the X-ray flux after three different filters. Therefore, the result is a matrix of eighteen different results. Each result is the average of 3-5 different shots, and the standard deviation of those is taken as uncertainty. All the results, with their uncertainties, are listed in table 4.46.

Data		Low Energy			High Energy		
	Filter	Al-bulk	Ag NWs	Ag-bulk	Al-bulk	Ag NWs	Ag-bulk
Flux	Ti 2 um	15,40	10,50	16,96	76,13	60,91	152,31
Flux_error	Ti 2 um	1,67	1,02	3,59	3,53	4,96	13,57
Flux	Ni 1 um	2,18	35,49	122,40	38,17	412,61	824,55
Flux_error	Ni 1 um	0,39	5,82	16,87	6,32	74,39	76,83
Flux	Al 3 um	13,15	1,36	160,67	45,84	45,41	845,53
Flux_error	Al 3 um	1,46	0,22	26,45	2,75	5,65	83,55

Figure 4.46: Results from green laser analysis. Entries marked in red were found to be affected by saturation. Uncertainty is listed below each value.

By observing the signal shapes, some events were found to be affected by saturation. Those values are marked in red on the table, and might underestimate the actual value. It is immediately clear (see the data in histogram form, 4.47) that the Ag-bulk target yielded the highest X-ray flux for both energies and all filters. Al-bulk and Ag-NWs yielded lower fluxes, but with interesting differences depending on filter and energy. Flux

from the nanostructured target is comparable to the bulk aluminum one for Ti and Al filters, but substantially higher for the nickel filter, at both energies.

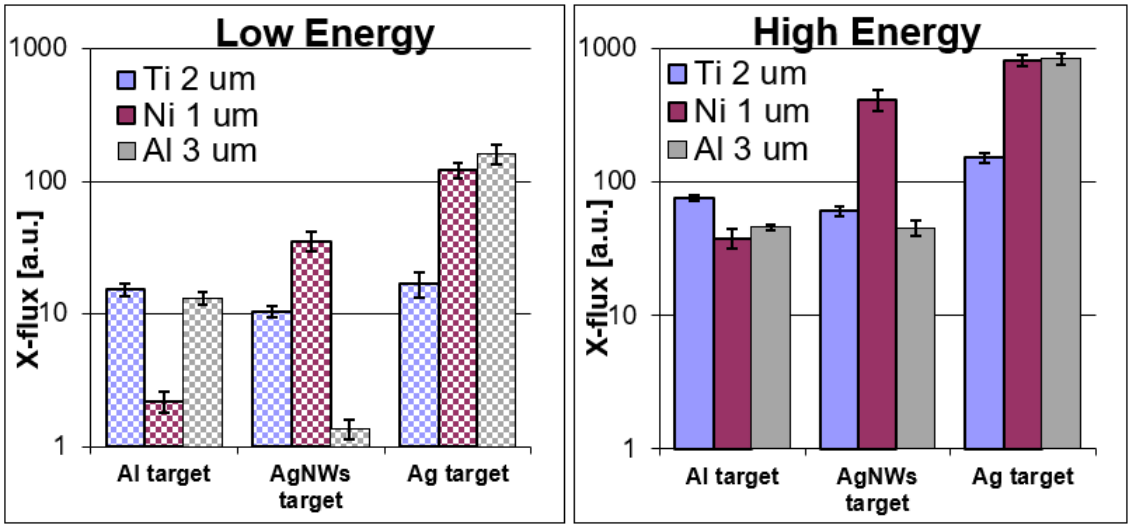

Figure 4.47: X-ray fluxes from green laser irradiation at L'Aquila, in histogram form.

This behaviour could have different explanation. First of all, it must be remembered that the nanostructures in the Ag-NWs target were still encased in the alumina matrix, due to technical limitations of the production of silver nanowires. Therefore, the plasma from the nanostructured target was a mix of Ag, Al, and O plasma. The strongest emission line for Oxygen, for example, would be heavily soppressed by Ti and Al filters, but less so from the Ni filter. Line emission from Oxygen, therefore, could help explai the difference between the results from different filters. On the other hand, Al line emission is strongly absorbed by Al, so the very low result for flux from Al with Al filter could be partly due to a substantial component of line emission being masked. To better understand the comparison between bulk and nanostructured targets, it's useful to see the flux ratio between nanostructured and bulk targets (fig 4.48).

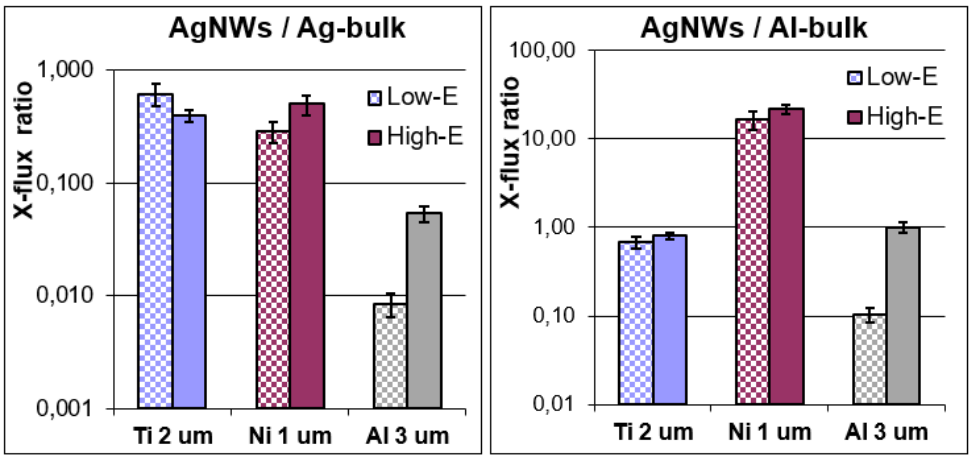

Figure 4.48: Ratio between measured flux for nanostructured target versus the bulk samples - Ag on the left, Al on the right. Note the log scale.

Comparing Ag-NWs with Ag-bulk, it's interesting to notice that while the bulk target always radiates more X-rays, the flux is most similar for Ti filter, most sensitive to low energy photons, and least similar for Al filter, sensitive to relatively high energy photons. Assuming line emission doesn't skew the comparison, this is suggestive of plasma in bulk Al being hotter.

4.6.5 Discussion

While 532 nm data are preliminary, they give valuable indications about the nanostructures' contribution to laser pulse absorption. Specifically, X-ray flux yield reached up over 50% (up to 62%) of that from bulk Ag. Given that bulk Ag emits a much higher X-rays flux compared to bulk Al, and the plasma Ag nanowires in allumina contains only 20% of Ag atoms (by stoichiometric ratio), a target made of free nanowires, without the alumina matrix (which produced the best result at 1064 nm) could be expected to perform better.

The nanostructured target does not simply behave as an Al/Ag mix, even if part of the results could be explained as being due to the alumina matrix and the resulting line emission. This could be a sign of plasmonic effect playing a role in laser-matter interaction.

In the future, the 532 nm laser setup at L'Aquila could be substantially upgraded, for example by improving energy stability, eliminating saturation, and adding planned detectors which would allow to collect spectral information. Detailed information from 532 nm pulses would allow a reliable comparison with the 1064 nm study. Response to polarization, a signature of plasmonic aspect should be tested with different angles and materials to quantify its impact.

Conclusions

The PLANETA experiment worked on a minimally investigated phenomenon, plasmonic absorption in laser-plasma production. There is little theoretical or experimental work pertaining the matter yet, so data interpretation was complex and a lot of energy was devoted to produce and improve the hardware and software required to collect and analyse data. To get a comprehensive picture of the behaviour of laser-produced plasma on nanostructures, much more data would be required. A few conclusions, however, can be drawn from the available evidence:

- Plasma produced by nanostructured targets behaves in many aspects (temperature, X-ray flux) like a mixture of the constituent elements, especially at high pulse energy. This is because at some point of the incoming pulse nanostructures are destroyed by irradiation, so they can no longer play a role in laser-matter coupling.

- At lower pulse energy, when a greater fraction of the laser pulse can be absorbed before the material's structure is destroyed, nanostructured targets reach comparable X-ray emission and temperature to targets made of the nanowires metal, possibly indicating that absorption in the nanowires offsets the presence of the lighter elements.

- Plasma emission from nanostructured targets is sensitive to the plane of polarization of the laser pulse. Polarization-dependant light absorption is typical of plasmonic light coupling, and is one more sign of nanostructures playing a role in the early stages of plasma evolution.

- The nanostructured targets which obtain the higher X-ray flux are those of Nickel or Cobalt, freestanding. Nanowires' diameter and length showed a weak dependence on plasma emission, but might play an important role in the formation of resonance conditions with a given wavelength.

- Spatio-temporal evolution of the plasma plume for nanostructured targets shows a distinctive pattern of angular ion emission, compared to bulk targets, which emits closer to the target normal. The reason is unclear, but it's further evidence of nanostructures influencing plasma formation.

- The geometry of craters formed as a result of the laser-matter interaction seems to relate only weakly to plasma parameters. This is probably because the most important processes for crater formation are melting and vaporization, with just a small fraction of the ablated matter becoming ionized. However, nanowires freed

from the alumina matrix are deeper than craters in bulk Al despite having similar volume, possibly a result of energy transport along the nanowire's axis.

The knowledge acquired with the nanosecond pulses used in this experiment could be used to produce targets to irradiated at femtosecond pulse laser facilities. These pulses would be fast enough to deliver energy before nanostructures are destroyed, thus allowing to exploit their full potential.

Bibliography

[1] Tajima, Toshiki and Malka, Victor. (2020). "Laser plasma accelerators. Plasma Physics and Controlled Fusion." 62.

[2] Szweda, Roy., "Handbook of microlitography, micromachining and microfabrication, vol. 1: Microlitography." - *Università degli studi di Bologna, 2004*

[3] Luca U. Labate PhD dissertation, "Progress in laser-plasma X-ray sources: time-resolved spectroscopic studies and applications to µ-imaging" - *Università degli studi di Bologna, 2004*

[4] Michael Antony Purvis PhD Dissertation, "relativistic plasma nano-photonics for ultra-high ehergy density physics" - *Colorado State University): 2014*

[5] Brown, Matthew S., and Craig B. Arnold. "Fundamentals of laser-material interaction and application to multiscale surface modification." chapter 4. Springer Berlin Heidelberg, 2010: 91-120.

[6] Purvis, Michael A., et al. "Relativistic plasma nanophotonics for ultrahigh energy density physics." - *Nature Photonics 7.10 (2013): 796-800.*

[7] Lanzalone, G., et al. "Effect of advanced nanowire-based targets in nanosecond laser-matter interaction." - *Review of Scientific Instruments 87.2 (2016): 02B324.*

[8] S. Lal, S. Link, and N. J. Halas, "Nano-optics from sensing to waveguiding" - *Nature photonics 1, (2007): 641*

[9] A. W. Sanders, D. A. Routenberg, B. J. Wiley *et al*, "Observation of Plasmon Propagation, Redirection, and Fan-Out in Silver Nanowires" - *Nano Letters vol.6, n.8 (2006)*

[10] Logeeswaran VJ, J. Oh, A. P. Nayak, *et al*, "A Perspective on Nanowire Photodetectors: Current Status, Future Challenges, and Opportunities" - *IEEE Journal of selected topics in quantum electronics 17.4 (2011)*

[11] Atwater, Harry A., and Albert Polman. "Plasmonics for improved photovoltaic devices." - *Nature materials 9.3 (2010): 205-213.*

[12] Wang, Wenhui, et al. "Light propagation in curved silver nanowire plasmonic waveguides." - *Nano letters 11.4 (2011): 1603-1608.*

[13] L.Malferrari, A. Jagminien, G. P. Veronese, F. Odorici, M. Cuffiani, and A. Jagminas: "Alumina Template-Dependant Growth of Cobalt Nanowire Arrays" - *Journal of Nanotechnology (2009): 149691*

[14] Lima, Joaquim, et al. "Optical properties of nanowire metamaterials with gain." - *Optics Communications 379 (2016): 25-31.*

[15] Yan, Ruoxue, et al. "Direct photonic–plasmonic coupling and routing in single nanowires." - *Proceedings of the National Academy of Sciences 106.50 (2009): 21045-21050.*

[16] C. T. Sousa, D. C. Leitao et al.: "Nanoporous alumina as templates for multifunctional applications" - *Applied Physics Review 1 (2014): 031102*

[17] Mariana P. Proencaa, Célia T. Sousa, João Venturaa, Manuel Vazquez, João P. Araujoa: "Ni growth inside ordered arrays of alumina nanopores: Enhancing the deposition rate" - *Electrochimica Acta 72 (2012): 215*

[18] Feiyue Li, Lan Zhang, and Robert M. Metzger: "On the Growth of Highly Ordered Pores in Anodized Aluminum Oxide" - *Chem. Mater. 10 (1998): 2470*

[19] "Anodic oxidation of Aluminum and its alloys" In Information Bulletin, vol. 14. London: The Aluminum development association, 1948.

[20] J. Choi, "Functional nanostructures by ordered porous templates" Ph.D. thesis, Martin-Luther University, 2004.

[21] Masuda H, Fukuda K, "Ordered metal nanohole arrays made by a two-step replication of honeycomb structures of anodic alumina." - *Science 268, (1995)*

[22] K. Nielsch, J. Choi, K. Schwirn, R. B. Wehrspohn, and U. Gosele, "Self-ordering Regimes of Porous Alumina: The 10% Porosity Rule" - *Nano Lett. 2, 677 (2002)*

[23] G. D. Sulka and K. G. Parkola, "Structural features of self-organized nanopore arrays formed by anodization of Aluminum in oxalic acid at relatively high temperatures"- *Electrochimica Acta 52, 1880 (2007)*

[24] Z. X. Su, G. Hahner, and W. Z. Zhou, "Electrochemical Anodizing, Structural and Mechanical Characterization of Nanoporous Alumina Templates"- *J. Mater. Chem. 18, 5787 (2008).*

[25] Tajima, "Luminescence, breakdown and colouring of anodic oxide films on Aluminum" - *Electrochim. Acta 22, 995 (1977).*

[26] Malferrari, L., et al. "Alumina Template-Dependant Growth of Cobalt Nanowire Arrays." - *Journal of Nanotechnology 2009 (2009)*

[27] Ditlbacher, Harald, et al. "Silver nanowires as surface plasmon resonators." - *Physical review letters 95.25 (2005): 257403.*

[28] Jafarabadi, Marzieh Akbari, and Mohammad Hossein Mahdieh. "Investigation of phase explosion in Aluminum induced by nanosecond double pulse technique." - *Applied Surface Science 346 (2015): 263-269.*

[29] Torrisi, L., A. Borrielli, and D. Margarone. "Study on the ablation threshold induced by pulsed lasers at different wavelengths." - *Nuclear Instruments and Methods in Physics Research Section B: Beam Interactions with Materials and Atoms 255.2 (2007): 373-379.*

[30] Margarone, D., et al. "Studies of craters' dimension for long-pulse laser ablation of metal targets at various experimental conditions." - *Applied Surface Science 254.9 (2008): 2797-2803.*

[31] Salle, B., et al. "Laser ablation efficiency of metal samples with UV laser nanosecond pulses." - *Applied surface science 138 (1999): 302-305.*

[32] Semerok, Alexandre F., et al. "Microablation of pure metals: laser plasma and crater investigations." Nonresonant Laser-Matter Interaction (NLMI-10). - *International Society for Optics and Photonics, 2001.*

[33] Price, D. F., et al. "Absorption of ultrashort laser pulses by solid targets heated rapidly to temperatures 1–1000 eV." - *Physical review letters 75.2 (1995): 252.*

[34] Mahdieh, M. H., et al. "Crater geometry characterization of Al targets irradiated by single pulse and pulse trains of Nd: YAG laser in ambient air and water." - *Applied Surface Science 256.6 (2010): 1778-1783.*

[35] Ruoxue Yan, Peter Pausauskie, Jiaxing Huang, and Peidong Yang: "Direct photonic–plasmonic coupling and routing in single nanowires" - *PNAS vol. 106 no. 50 (2009): 21045*

[36] Michael A. Purvis, Vyacheslav N. Shlyaptsev *et al*: "Relativistic plasma nanophotonics for ultrahigh energy density physics" - *Nature - photonics, vol 7 (2013): 796*

[37] G. Lanzalone, C. Altana *et al*: "Effect of advanced nanowire-based targets in nanosecond laser—Matter interaction" - *Review of Scientific Instruments 87 (2016)*

[38] H.J. Assenbaum and K. Langanke: "Effects of Electron Screening on Low-Energy Fusion Cross Sections " - *Z. Phys. A 327 (1987): 461*

[39] Glibert, K. M., *et al.* "X-ray yields of plasmas heated by 8-nsec neodymium laser pulses." - *Journal of Applied Physics 51.3 (1980): 1449.*

Abstract in italiano:

Questa tesi presenta I risultati di uno studio, parte dell'esperimento PLANETA (un programma di ricerca dell'INFN), sull'impato delle nanostrutture sull'interazione laser-materia. Specificamente, sul plasma creato su bersagli contenenti nanofili metallici irradiati con impulsi laser della durata di 6 ns, a 1064 e 532 nm di lunghezza d'onda, con densità di potenza nell'ordine di 10^12 W/cm^2.

I plasmi da laser sono di interesse per una vasta gamma di applicazioni scientifiche e tecnologiche, dall'utilizzo come sorgente di raggi X alla possibilità di fusione nucleare, grazie alle alte temperature e densità che si possono raggiungere all'interno del plasma.

Tuttavia, la maggioranza delle applicazioni sono limitate dalla scarsa penetrazione dell'energia del laser nella materia, a causa della rapida formazione di una superficie di densità critica riflettente all'interno del plasma.

L'esperimento PLANETA era mirato a investigare se bersagli con nanofili mettalici (cilindri sottili con diametro al di sotto dei 100 nm, inferiori alla lunghezza d'onda incidente, e alcuni micron di lunghezza) potessero portare alla produzione di un plasma più caldo e\o di durata superiore rispetto al metallo bulk. Il meccanismo proposto sarebbe la penetrazione più in profondità della luce laser nei bersagli, in quanto i nanofili sono altamente assorbenti nel range della luce visibile. Questo potrebbe portare a un riscaldamento volumetrico anziché superficiale, e quindi alla produzione di un plasma più caldo e denso rispetto a un bersaglio bulk.

I bersagli sono stati prodotti al laboratorio di microscopia elettronica dell'INFN di Bologna, con nanofili dai diversi parametri geometrici e composti di metalli diversi (Ni, Fe, Co e Ag). Sono stati irradiati con un laser Nd-Yag alla struttura INFN dei Laboratori Nazionali del Sud a Catania, e i plasmi così prodotti sono stati osservati con diversi tipi di detector per confrontarli con i plasmi da materiali bulk. L'esperimento PLANETA disponeva anche di un laser a 532 nm, presso una diversa struttura INFN, il Dipartimento di Fisica dell'Università Dell'Aquila. Sebbene al momento della scrittura di questa tesi i dati dall'irraggiamento con il laser verde siano limitati, forniscono un paragone utile e la loro analisi è stata inclusa.

Per studiare l'impatto delle nanostrutture sull'evoluzione del plasma, le proprietà dei plasmi prodotti sono state testate su bersagli di tipo diverso e con diverse condizioni del fascio (polarizzazione, energia).

Attività di Dottorato – Marco Frassetto:

Principali attività svolte durante il Dottorato:

- Partecipazione alle prese dati dell'esperimento PLANETA presso i Laboratori Nazionali del Sud (LNS) a Catania
- Progettazione e successivi upgrade del setup dell'esperimento PLANETA
- Calibrazione dei detector presso i LNS
- Realizzazione del software di analisi dati per diverse necessità dell'esperimento, in particolare:
    - Lettura e analisi del segnale della telecamera CCD sensibile ai raggi X, in modalità di integrazione del flusso, inclusa l'individuazione automatica delle regioni esposte al flusso X.
    - Lettura e analisi del segnale della telecamera CCD in modalità Single Photon, con analisi e accorpamento dei cluster, per ricostruire lo spettro.
    - Lettura e analisi dei collettori di ioni per la misura del Time of Flight, che ha poi portato a evidenziarne le criticità e a escluderli dai risultati.
    - Lettura e analisi dei dati provenienti dalla telecamera ICCD sensibile alla luce visibile
    - Produzione di semplici simulazioni per valutare l'impatto dei filtri sullo spettro X, e poi per ricostruire lo spettro a partire dal segnale osservato.
- Analisi dati per diverse parti dell'esperimento (dati visibile, raggi X, TOF)
- Presentazione dei risultati al congresso SIF 2018

Pubblicazioni:

- A. Muoio, C. Altana *et al*: "Nanostructured targets irradiation by ns-laser for nuclear astrophysics applications: first results" – *European Physical Journal Conferences, 165, 01002 (2017)*
- A. Muoio C. Altana *et al:* "Nanostructured targets irradiation by ns-laser for nuclear astrophysics applications: first results" – *Journal of Instrumentation, Volume 12 (2017)*
- G. Lanzalone, A. Muoio *et al:* "Nuclear Reactions Studies in Laser-Plasmas at the forthcoming ELI-NP facilities" – *Journal of Physics, conference series 1014:012006 (2018)*
- G.Pirruccio, D. Rocco *et al:* "Numerical simulations on laser absorption enhancement in hybrid metallo-dielectric nanostructured targets for future nuclear astrophysics experiments", *AIP Advances 10, 045020 (2020);*